The Reconstruction of Mass Profiles from Simulated Stacked Weak Gravitational Lensing

Christopher Davis

April 16, 2012

Contents

Chapter 1

Introduction

1.1 History of Gravitational Lensing

Ironically, the naive assumption of particles of light leads closely to the actual deflection caused by the bending of spacetime. The Newtonian conception of gravity predicts that light would be deflected by an angle $\alpha = 2GM/(c^2\xi)$, where G is the gravitational constant, c is the speed of light, and ξ is the impact parameter of the incoming particle of light. In reality, general relativity predicts that light will bend *twice* as much:[1]

$$\alpha = \frac{4GM}{c^2\xi} = 1''.75 \left(\frac{M}{M_\odot}\right)\left(\frac{\xi}{R_\odot}\right)^{-1}, \tag{1.1}$$

where the second equivalence gives the deflection in terms of common astronomical parameters (Schneider 2006a). A deflection of 1.7 arcseconds can be measured during the Solar Eclipse, and measurements of the deflection during the Solar Eclipse in 1919 were sufficiently convincing to grant Einstein's theory a tremendous boost in legitimacy. Lodge (1919) soon thereafter coined the term "lens" when considering gravitational light deflection, even though a gravitational lens has no focal length.

Einstein himself was dismissive of any further applications of the deflections: in a 1936 paper, he considered the lensing effects between two stars and concluded that the angular separation (owing to the relatively large impact parameter) would be too small (on the order of milliarcseconds) to resolve and hence unlikely to be observed (Einstein 1936). Einstein might be forgiven for his lack of imagination, for the Shapley-Curtis Debate had only settled the issue of external galaxies sixteen years prior (Curtis 1921; Shapley 1921). Fritz Zwicky examined the potential lensing properties of other galaxies (calling them "extragalactic nebulae") and, from considering estimates of the mass of the galaxies as well as their typical image separation, concluded that these lensing effects could not only test General Relativity, but also enable the observation of yet further galaxies (albeit distorted and magnified) and the determination of the mass of the lenses themselves (Zwicky

[1] Einstein (1920) refers to the coincidence, stating that "half of this deflection is produced by the Newtonian field of attraction to the sun, and the other half by the geometrical modification ("curvature") of space caused by the sun." In a sense, the particle theory of light is half-right.

1937a). Further, he concluded that galaxies acting as gravitational lenses would almost certainly be observed (Zwicky 1937b). Unfortunately for Zwicky, he was unable to observe any lens systems during his life.

For lack of evidence, the subject of gravitational lenses came to a halt. Almost thirty years later, however, with the publication of a smattering of papers pertaining to gravitational lensing (Klimov 1964; Liebes 1964; Refsdal 1964b,a) and the discovery of extremely luminous and distant "quasi-stellar" sources, the field of gravitational lensing once again became active. It would be over a decade before lens systems were observed and identified. These papers would greatly influence the very conception and application of gravitational lensing. Klimov (1964) considered galaxy-galaxy lensing and uses its results to estimate the number of "occulted galaxies" in a pencil beam of a given distance. Liebes (1964) considered the observation of "time symmetric pulses of light intensity" from transitory alignments, founding the field of microlensing. Refsdal (1964b) considered the gravitational lensing of point lens stars to obtain their mass, while Refsdal (1964a) used gravitational lenses in conjunction with supernovae to determine Hubble's constant, $H(z)$.

At this point, gravitational lensing was still a novel theory. It was not until 1979 that multiple images from a gravitational lens system were confirmed in QSO 0957+561. Seeking to identify radio sources in the optical band, Walsh et al. (1979) discovered a pair of quasars with a magnitude of 17, a $5\farcs7$ separation at $z = 1.405$, and nearly identical colors and spectra. They interpreted these two images as resulting from gravitational lenses. Using Charge Coupling Devices, Young et al. (1980) observed the lens responsible for the radio sources and concluded that the images arise from a galaxy-cluster combination at $z = 0.39$, while Stockton (1980) further constrained the lens galaxy. In another case, Lynds and Petrosian (1986) and Soucail et al. (1987) observed giant luminous arcs at Abell cluster A 370 which were later confirmed as gravitational lensing events (see Paczynski 1987; Soucail et al. 1988).

1.2 Weak Gravitational Lensing

Concurrent with the discovery of strongly-lensed images was the development of the theory of *weakly*-lensed images, where, unlike arcs and arclets, the distortion of a galaxy cannot be easily distinguished from its intrinsic shape. Tyson et al. (1984) presented "a fundamentally new technique for measuring galaxy mass" through statistical measurements of faint galaxy images. Systematic stretch distortions could be attributed to the mass distribution in foreground galaxies through gravitational lensing. Unfortunately for them, their observations could not confirm their technique. Webster (1985) furthered the technique and postulated that, instead of looking for galaxy-galaxy lensing in order to measure galaxy mass, one should look for cluster-galaxy lensing to instead constrain cosmological parameters. Miralda-Escude (1991) proposed a means by which the correlation of ellipticities produced by gravitational lensing may be distinguished from innate elliptical correlations, emphasizing its application in determining large scale structure. Kaiser

(1992) analyzed the two-point statistics of deformations caused by gravitational lensing and posited a means of relating the distortions to the mass fluctuation power spectrum.

After the first giant arcs in clusters were discovered by Lynds and Petrosian (1986) and Soucail et al. (1987), Fort et al. (1988) observed objects in A 370 which, while less obviously stretched than the giant arcs, still showed unnaturally large axis ratios aligned along the tangent vector to the cluster center.[2] These "arclets" were later verified via spectroscopy by Mellier et al. (1991) to have arisen from gravitational lensing. The arclets pointed to a powerful fact: if background galaxies can be deformed so strongly that multiple images arise from gravitational lensing, then there should be many more images where the distortion effect can only be observed statistically.

Tyson et al. (1990) finally confirmed the "systematic alignment" of faint background galaxy images centered on foreground galaxy clusters with high velocity dispersions in order to constrain dark matter distributions. Much discussion grew from this discovery. Blandford et al. (1991) considered the possibility that coherent shear distortions may arise from large-scale structure caused by inhomogeneities in the universe. They posited that inhomogeneities – especially anisotropies on the cosmic microwave background – could be tested on scales of ~ 100 Mpc and be used to distinguish different cosmologies. Motivated by Tyson et al. (1990), Kaiser and Squires (1993) rigorously established the theoretical basis for weak-lensing and showed how the measurement of galaxy ellipticities can yield a surface density measurement for a cluster. The formalisms contained therein are the basis for much of weak-lensing theory. Bartelmann (1995) delimited the accuracy of cluster mass reconstruction from "ideal" weak lensing data, concluding that "the cluster reconstruction techniques based on the weak lens effect can achieve an accuracy of the reconstructed mass on the order of 10%–20%, if they are applied to fields with side lengths of 10′ or larger."

Initially, weak gravitational lensing faced several technical problems. Because weak lensing relies on the measurement of shapes of source objects, poor seeing conditions could entirely compromise measurements of the weak lensing effect. The measurements also need high resolution imagery, and when weak lensing first took off, photographic plates were still heavily used. Photographic plates are not linear detectors, so correcting for the point spread function was difficult and unreliable. Even with the advent of CCD cameras, the pixel size was too large (of order an arcsecond) to detect weak lensing signals. In addition to small enough pixel sizes, the cameras must also view a large area of sky (often more than a square degree), demanding much of the camera and also – perhaps more importantly – of the observational astronomers and the time allocation committees (see Wambsganss 1998). Perhaps in retrospect it is easy to see why it could be difficult to convince the astronomy community of the validity, and indeed necessity, of prioritizing weak lensing observations: unlike giant arcs, weak lensing cannot be "seen," nor is it easy to graphically display.[3] Even modeling the shape is fraught with difficulty: there is no guarantee that a galaxy will appear ellipsoidal, and several different definitions for object

[2] See Section 2.1.

[3] "At least one can display a temperature map of the [CMB anisotropies in the] sky" (Schneider 2006b).

ellipticities exist (Schneider 2006b).

A major priority (perhaps unstated) of early weak lensing measurements hence was the establishment of credibility. Brainerd et al. (1996) measured 3202 pairs of source and lens galaxies[4] and found results for mass distributions of the galaxies consistent with other methods of mass determination.[5] Schneider and Rix (1997) followed up this discovery with the development of a maximum-likelihood analysis that can constrain galaxy properties through "galaxy-galaxy" lensing, obtaining reasonably accurate ($<$10%) measurements of sizes and velocity dispersions from a sample of about 5000 galaxies. However, lensing mass measurements often disagreed with X-ray measurements – or other lensing measurements on the same objects by different groups – by a factor of 2 to 3 (see Miralda-Escude and Babul 1995; Pierre et al. 1996; Sahu et al. 1998; Ota et al. 1998; Wu and Fang 1997). Smail et al. (1997) and Allen (1998) performed detailed comparisons between lensing and X-ray masses for a number of lensing clusters and concluded that wrong assumptions on the physical state of gas could contribute significantly to the discrepancy, while Navarro et al. (1997) proposed that the analytical models used for modeling mass distributions on the lensing side might be inappropriate. Mahdavi et al. (2008) followed on these sentiments and looked at finely resolved X-ray clusters, measuring the mass from both X-ray hydrostatics and from weak lensing. With the improvements in technology and methodology over the course of the decade, the discrepancy had greatly decreased to, at worst, a 20% difference. Much work since then has been devoted to resolving the discrepancy, for example from the Local Cluster Substructure Survey (Zhang et al. 2008): Zhang et al. (2010) obtained measurements of cluster masses from *XMM-Newton* and Subaru[6] with the purpose of testing deviation from hydrostatic equilibrium and testing the presence of non-thermal pressure support, finding that the two methods were in agreement to within 10%, with the worst discrepancies arising from disturbed clusters.[7]

The proliferation and increasing acceptance of weak lensing measurements coincided with several major survey projects, most notably the Sloan Digital Sky Survey (SDSS).[8] The SDSS has obtained multi-color images over more than a quarter of the sky, cataloging nearly a million galaxies and over a hundred thousand quasars. The data is released to the public. With such a large amount of data, weak lensing measurements and analysis exploded. Fischer et al. (2000) used early release SDSS data and conducted galaxy-galaxy weak lensing shear observations over a 225 deg^2 and more than forty million pairs of galaxies to obtain galaxy-mass correlation and galaxy-galaxy autocorrelation functions as

[4]Far more than Tyson et al. (1990) had – improvements in technology greatly aided the field. Tyson et al. (1990) found the systematic alignment of only "20-60 faint background galaxy images."

[5]"Zaritsky & White (1994) have analyzed a sample of companion galaxies to isolated local spirals and find [mass distribution results], consistent with our findings. . . . Since the assumptions underlying the two techniques are very different, the close agreement between the two methods is encouraging" (Brainerd et al. 1996).

[6]From X-ray hydrostatics and weak lensing, respectively.

[7]A cluster is classified as "disturbed" based on its X-ray morphology. A disturbed cluster then has more "non-thermal pressure support."

[8]http://www.sdss.org/

well as constrain the value of Ω_M. In the next year, McKay et al. (2001) used the same data to model the surface mass density contrast to a power-law fit and hence obtain mass and luminosity scalings for spiral and elliptical galaxies in a variety of environments. Seljak (2002) constrained galaxy halo profiles by combining SDSS weak lensing measurements with Tully-Fisher and Fundamental Plane relations, concluding that baryonic effects on rotation velocity play a significant role in the latter two relations. Sheldon et al. (2004) related the observed tangential shear from SDSS data to the galaxy-mass cross-correlation function – similar to Fischer et al. (2000), except over a much larger region (nearly 3800 deg^2) and with spectroscopic data for the lens galaxies. At this time, most of the model fits for the galaxy correlation function were simple power law fits; Zehavi et al. (2004) found that there were systematic departures from the best-fit power law at closer ranges inside the halo, concluding that the observed inflection arose from the combination of one- and two-halo correlation functions. Seeking to complement the extensive photometric studies of elliptical galaxies, Mandelbaum et al. (2006) measured the 3D density profile of groups and clusters of luminous red galaxies with galaxy-galaxy weak lensing out to 2 h^{-1} Mpc, finding that the singular isothermal sphere profile is ruled out relative to the Navarro-Frenk-White profile at a 95% level. Johnston et al. (2007b) measured the statistical weak lensing measurements of 130,000 groups and clusters of galaxies in the SDSS (with an eye to future deep, wide-area optical surveys), constraining the halo concentration parameter and the halo bias as a function of cluster mass and finding their results in good agreement with N-body simulations of ΛCDM models.

Numerical models kept pace with the observations. Berlind and Weinberg (2002) examined galaxy bias in the framework of the "halo occupation distribution" for N-body simulations, obtaining a galaxy mass correlation function and relating the results to SDSS redshift surveys, while Guzik and Seljak (2002) presented a theoretical analysis of galaxy-galaxy lensing that tested the results of the SDSS measurements to examine the virial masses of galactic haloes as well as the conversion of baryonic matter into stars. Yoo et al. (2006) developed a method for combining the mean surface density contrast and the galaxy-galaxy correlation function to constrain the matter density parameter Ω_M and the matter fluctuation amplitude σ_8, then "went backwards" to make predictions on how SDSS data may be used to determine Ω_M and σ_8. Johnston et al. (2007a) presented a non-parametric method for determining the mean 3D density and mass profile from weak-lensing measurements around stacked clusters (see also Sheldon et al. 2009), testing the method on N-body simulations and proposing its application in SDSS and other deep wide-area surveys. Baldauf et al. (2010) used SDSS luminous red galaxy data from (Mandelbaum et al. 2006) in conjunction with N-body simulations to develop a method for reconstructing the dark matter correlation function from both galaxy-galaxy lensing and galaxy-clustering measurements.

In addition to measurements and theoretical predictions, systematics in the SDSS were considered. Hirata et al. (2004) investigated shear calibration bias, concluding that shear amplitude in the SDSS sample is calibrated to better than 18 percent even when including noise-induced calibration biases in the ellipticity. Mandelbaum et al. (2008b) developed

statistics to quantify the effect of redshift errors on lensing results, finding calibration biases as high as 20% for "methods in active use," although also arguing that the galaxy-galaxy lensing calibration error can be reduced to as low as 2%. Joachimi et al. (2011) investigated the correlation of intrinsic ellipticities between two galaxies[9] and determined the normalization of the intrinsic alignment power spectrum. Seeing the need for a redshift probability distribution (as many potential source and lens galaxies lack the spectroscopic data needed to determine redshift), Sheldon et al. (2011) developed one for the SDSS DR8 imaging data, encouraging its use for each galaxy (as opposed to an ensemble of galaxies).

I am focusing on the weak lensing results of the SDSS so much because it represents a model for future weak lensing projects. By being publicly available, the SDSS data has opened the way for an extreme variety of different scientific projects, whether they be observational, calibrational, or computational. The concurrent developments in one "subfield" have influenced the others significantly. This thesis examines mock data prepared for groups in the Dark Energy Survey (DES) collaboration.[10] As such it straddles the three distinct groups I have outlined above: in as much as it is an N-body simulation with true shear values, its results are theoretical, but the analysis of the mock data can give valuable insights into possible observational systematics and can even make predictions about what will be observed when the DES goes live. The Dark Energy Camera is expected to come online in the next year and will observe 5000 deg^2 to about the 24th magnitude. Additionally, the Hyper Suprime-Cam is also expected to come online in the next year and will survey a 1500 deg^2 area to about the 25th magnitude. Combined, the two surveys will measure the shapes of nearly 300 million galaxies and provide photometric redshifts out to $z \sim 1.3$ (Weinberg et al. 2012). In the future, much of the work below may readily be adapted to these observational data, providing simultaneously an insight into the nature of our physical universe and a check on the simulated one.

1.3 Other Uses of Gravitational Lensing

This section summarizes some of the ways gravitational lensing is now applied.

Measuring mass and mass distributions. The deflection of light is determined by the spacetime geometry through which light propagates, which in turn is related to

[9] In weak lensing, one must account for two types of intrinsic alignments. In the first, one accounts for correlations between the intrinsic ellipticities of the foreground galaxies and the shear field they produce (or, in other words, how much of the shear observed cannot be attributed to the lens itself). These may arise from, e.g., large-scale structures yet closer in the foreground. In the second type, one accounts for the correlations between shapes of lens and source galaxies (or, in other words, how much of the source shape observed cannot be attributed to the shear field). These may arise from, e.g., similar formation environments. Generally, stacked weak lensing can eliminate the first type of intrinsic ellipticity by sampling over-dense and under-dense regions.

[10] http://www.darkenergysurvey.org/

the gravitational field determined by the mass distribution. The deflection is independent of the *type* of matter; gravitational lensing will be detected if there is a large enough mass present, whether that mass is luminous, dark, hot, cold, mundane, or exotic. Gravitational lensing cannot differentiate between the types of mass, but that also means that it cannot favor one type of mass (say, hot masses) over the other. This makes it an ideal tool for measuring the total mass of an astronomical body, including its dark and luminous contents. With care, precise mass and mass distribution measurements are possible to within a few percent.

Setting the upper limit of the number density of mass concentrations. The probability for a lensing event to occur depends on the number density of the lenses. Then, by investigating the fraction of lensing events in a sample of sources, one can infer the number density in a sample. This method was famously used to constrain the number density of massive compact objects in our galaxy or other objects (either by observation or non-observation), but may also be used to examine the redshift evolution of, e.g., galaxies and clusters that produce strong or weak lensing signals.

Following Liebes (1964), Paczynski (1986) proposed to monitor the Large Magellanic Cloud for variabilities in the brightness of stars. The main application would again be cosmological: one theory for dark matter was that it consisted of massive compact halo objects (MACHOs), such as black holes, brown dwarfs, neutron stars, or unassociated planets. These objects – which would be extremely difficult to detect via their intrinsic luminosity – would pass in front of stars, causing a time-dependent magnification event with a characteristic light curve dependent on the mass of the MACHO. Unfortunately, only one out of ten million stars in the Large Magellanic Cloud were expected to be lensed. Alcock et al. (1993); Aubourg et al. (1993) both took up the task and reported microlensing events. These observations concluded that MACHOs could only explain about 20% of the dark matter in the galaxy (Alcock et al. 2000). More recent measurements by Wyrzykowski et al. (2011) in the OGLE project have concluded that MACHOs in the range of $M = 0.1 - 0.4 M_{\odot}$ are only 6% of the Galactic halo, while MACHOs with mass less than 1 $M_{\odot}$ have an upper fraction limit of 9%.

Magnifying distant objects. Because gravitational lensing magnifies background sources, lens systems can act as natural telescopes, facilitating the observation and sometimes even the actual detection of extremely distant sources (Fan et al. 2003, for example).

Discovering planets. Just as a star passing in front of another star causes a transient magnification event, so too can a planet attached to the transiting star cause a further (if shorter and weaker) transient magnification event. Compared to other methods of discovering planets (radial velocity, direct imaging), this method is conceptually simple, requiring of its telescopes only the ability to detect changes in total flux over time to an appropriate degree of sensitivity. The telescopes need to cover a large

area of the sky, but they do not need to be large. Unfortunately, like all transient events, once the event is over, it cannot be observed again; there is no way to "take a second look" at a micro-lensed planet.

Constraining cosmology. Refsdal (1964a) noted that the Hubble constant can be obtained from the time delay in multiple image systems. The major advantage here is that the estimates bypass the distance ladder used in other measurements of H_0 and can also measure it at much larger distances. Weak lensing of large-scale structure can be used to determine the bias parameter (a probe of the correlation between dark matter and galaxy distributions), the matter density parameter, Ω_M, and other cosmological parameters. In particular, weak lensing studies of the cosmic microwave background provide valuable insight into the equation of state of dark energy.

Following Refsdal (1964a), the light curves of the QSO 0957+561 were measured in the optical and radio bands (Vanderriest et al. 1989; Schild 1990; Lehar et al. 1992). From these results, time delays were obtained, although with significantly different results: the time delays ranged from 410 to 540 days. Kundic et al. (1997) put the measure to rest for QSO 0957+561, measuring a short time delay of 417 days, which Colley et al. (2003) constrained to an impressive precision of 417.09 ± 0.07 days. Fadely et al. (2010) used these measurements and improved methodologies to obtain a Hubble constant of $H_0 = 79.3^{+6.7}_{-8.5}$ km s^{-1} Mpc^{-1}.

1.4 Outline of the Thesis

As the previous sections have noted, gravitational lensing and especially weak gravitational lensing has come to the fore as a means for conducting a variety of observations and experiments. This paper will specifically focus on the application of weak gravitational lensing toward measuring the mass distributions of clusters. It aims to tease out systematics – specifically with regard to ellipticities in the stacked profile – in the selection of clusters of galaxies during large sky surveys like the SDSS and DES by comparing the lensing profiles of selected clusters of galaxies with their matched dark matter halos.

In order to accomplish this task, the general theoretical formalism of gravitational lensing is presented in the next chapter, with some digressions into popular cosmological distance and mass profile models. A new (if only subtly different) model for deprojecting the lensing profile into a three dimensional mass profile is presented, and the formalism for deprojecting elliptical profiles into a spherical mass profile is developed and shown. In the third chapter, the simulation data set is presented, while the methods and systematics for converting halo and cluster lensing profiles into mass profiles is explained. The results of the simulations are presented in the fourth chapter. In the fifth and final chapter, these results and potential further work are discussed, and the major conclusions of this thesis are highlighted.

Chapter 2

Theoretical Preparation

2.1 Gravitational Lensing Basics

Consider the deflection of a light ray with impact parameter ξ to a spherically symmetric mass M. General Relativity predicts that the deflection angle $\hat{\alpha}$ is

$$\hat{\alpha} = \frac{4GM}{c^2\xi}, \tag{2.1}$$

provided that ξ is much larger than the Schwarzschild radius of some mass, $\xi \gg R_S \equiv 2GM/c^2$. But if this is the case, then the deflection angle is small, $\hat{\alpha} \ll 1$, so the Newtonian gravitational field strength is small, $\phi_N/c^2 \ll 1$. In such conditions, the field equations of General Relativity may be linearized, so the deflection angle of a set of mass points is then the sum of the deflections from each individual mass. Further, if the deflection angle is small, the deflected light ray may be approximated as a straight line. Let the location of a mass element $\mathrm{d}m$ be $\boldsymbol{r}' = (\xi_1', \xi_2', r_3')$, where r_3' is the radial distance to the mass element and $\boldsymbol{\xi}'$ is in the two dimensional plane perpendicular to r_3'. A small deflection angle is then equivalent to $|\xi| \ll r_3$. The total deflection angle is then the (vector) sum of the individual deflections:

$$\bar{\boldsymbol{\alpha}}(\boldsymbol{\xi}) = \frac{4G}{c^2} \sum \mathrm{d}m(\xi_1', \xi_2', r_3') \frac{\boldsymbol{\xi} - \boldsymbol{\xi}'}{|\boldsymbol{\xi} - \boldsymbol{\xi}'|^2} \tag{2.2}$$

$$= \frac{4G}{c^2} \int \mathrm{d}^2\boldsymbol{\xi}' \int \mathrm{d}r_3' \rho(\xi_1', \xi_2', r_3') \frac{\boldsymbol{\xi} - \boldsymbol{\xi}'}{|\boldsymbol{\xi} - \boldsymbol{\xi}'|^2}, \tag{2.3}$$

where we have substituted a mass distribution, $\mathrm{d}m = \rho(\boldsymbol{r})\mathrm{d}V$, for some volume $\mathrm{d}V$ and mass density ρ. The last factor in Equation (2.3) is independent of r_3', and so the r_3'-integration of ρ yields the mass density projected onto a plane perpendicular to the light ray, otherwise known as the surface mass density Σ:

$$\Sigma(\boldsymbol{\xi}) \equiv \int \mathrm{d}r_3 \rho(\xi_1, \xi_2, r_3). \tag{2.4}$$

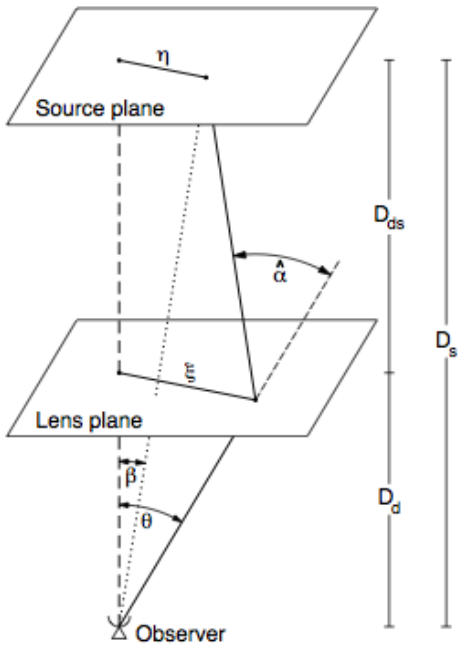

Figure 2.1: A sketch of a typical gravitational lens system (Schneider 2006a).

Thus, the deflection angle produced by some density distribution is

$$\bar{\boldsymbol{\alpha}}(\boldsymbol{\xi}) = \frac{4G}{c^2}\int \mathrm{d}^2\boldsymbol{\xi}'\Sigma(\boldsymbol{\xi}')\frac{\boldsymbol{\xi}-\boldsymbol{\xi}'}{|\boldsymbol{\xi}-\boldsymbol{\xi}'|^2}. \tag{2.5}$$

It is worth reiterating the caveats in Equation (2.5): the impact parameter must be much larger than the Schwarzschild radius, gravity must be weak enough to be linearized, and the deflection angle must be small enough (compared to the scale over which the mass changes) as to be approximately straight around the mass. Lensing by galaxies, clusters of galaxies, and halos satisfy these conditions, but there are instances where this is not the case (see Schneider 2006b).

Now consider a mass concentration at an angular diameter distance[1] D_d away which deflects the light rays from a source at distance D_s, as in Figure 2.1. If the distance along the line-of-sight to the deflector is much greater than the transverse line-of-sight distance of the mass distribution,[2] then the deflections may be described with Equation (2.5). Let $\boldsymbol{\eta}$ be the two-dimensional position of the source in the source plane. Utilizing the small angle approximation in Equation (2.5), Figure 2.1 implies that

$$\boldsymbol{\eta} = \frac{D_\mathrm{s}}{D_\mathrm{d}}\boldsymbol{\xi} - D_\mathrm{ds}\hat{\boldsymbol{\alpha}}(\boldsymbol{\xi}). \tag{2.6}$$

It is more convenient to work in angular coordinates $\boldsymbol{\eta} = D_\mathrm{s}\boldsymbol{\beta}$ and $\boldsymbol{\xi} = D_\mathrm{d}\boldsymbol{\theta}$, as well as

[1] See Section 2.2.

[2] Clusters of galaxies are on the scale of a few Mpc, while the distances are typically a few thousand Mpc.

defining the scaled deflection angle,

$$\boldsymbol{\alpha}(\boldsymbol{\theta}) = \frac{D_{\rm ds}}{D_{\rm s}}\bar{\boldsymbol{\alpha}}(D_{\rm d}\boldsymbol{\theta}). \tag{2.7}$$

From these definitions, we transform Equation (2.6) to

$$\boldsymbol{\beta} = \boldsymbol{\theta} - \boldsymbol{\alpha}(\boldsymbol{\theta}). \tag{2.8}$$

This is the lens equation. A source with true position $\boldsymbol{\beta}$ in the sky will be observed by an observer at an angular position $\boldsymbol{\theta}$ that satisfies Equation (2.8). Therefore, if multiple $\boldsymbol{\theta}$ satisfy Equation (2.8), then images will appear at several positions on the sky, that is, the lens produces multiple images. That is the "strong" lensing case.

It is convenient to transform the surface mass density into a dimensionless angular surface mass density, also known as the convergence:

$$\kappa(\boldsymbol{\theta}) = \frac{\Sigma(D_{\rm d}\boldsymbol{\theta})}{\Sigma_{\rm crit}}, \tag{2.9}$$

where $\Sigma_{\rm crit}$ is the critical surface mass density, which depends on the distances to the source and lens,

$$\Sigma_{\rm crit} = \frac{c^2 D_{\rm s}}{4\pi G D_{\rm d} D_{\rm ds}}. \tag{2.10}$$

Figure 2.2 plots the critical surface mass density as a function of source and lens redshifts under the cosmology of this thesis.[3] The critical density increases as the lens-source distance decreases, and increases as the lens distance increases.

We can now apply a similar transformation procedure from physical to angular distances to Equation (2.5):

$$\boldsymbol{\alpha}(\boldsymbol{\theta}) = \frac{1}{\pi}\int \mathrm{d}^2\theta' \kappa(\boldsymbol{\theta}') \frac{\boldsymbol{\theta} - \boldsymbol{\theta}'}{|\boldsymbol{\theta} - \boldsymbol{\theta}'|^2}. \tag{2.11}$$

It will be useful to think in terms of scalar deflection potentials, such that $\boldsymbol{\alpha} = \nabla\psi$. ψ may be written as

$$\psi(\boldsymbol{\theta}) = \frac{1}{\pi}\int \mathrm{d}^2\theta' \kappa(\boldsymbol{\theta}') \ln|\boldsymbol{\theta} - \boldsymbol{\theta}'|. \tag{2.12}$$

(Recall that $\nabla \ln|\boldsymbol{\theta}| = \boldsymbol{\theta}/|\boldsymbol{\theta}|^2$ for any two-dimensional vector $\boldsymbol{\theta}$.) In further analogy to typical potentials, it is possible to obtain a two-dimensional Poisson equation by using the identity $\nabla^2 \ln|\boldsymbol{\theta}| = 2\pi\delta(\boldsymbol{\theta})$, where δ is the Dirac delta function. Applying the Laplacian to Equation (2.12), one finds that

$$\nabla^2\psi = 2\kappa. \tag{2.13}$$

The two-dimensional Poisson equation provides a useful conceptual framework for thinking about lensing: ψ corresponds to the gravitational potential, κ corresponds to the mass density, and $\boldsymbol{\alpha}$ corresponds to the acceleration vector.

[3] See Section 2.2.

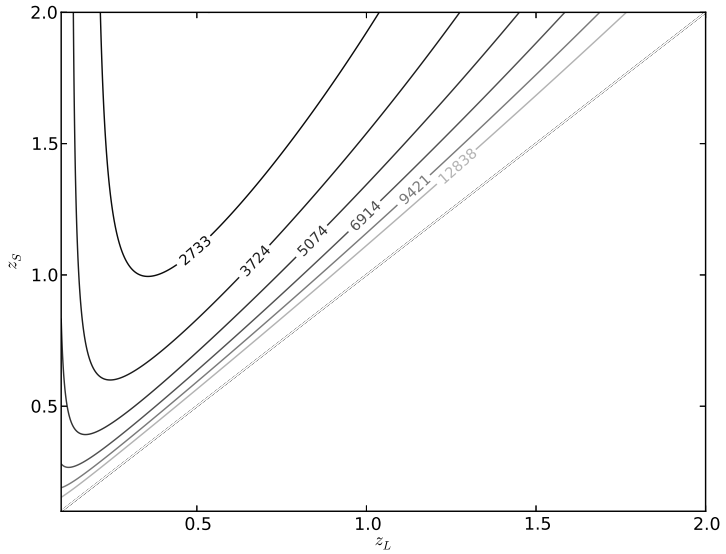

Figure 2.2: Contour plot of the critical density as a function of the source and lens redshifts in $M_\odot/\mathrm{pc}^2$. Recall that a source with $z_\mathrm{s} < z_\mathrm{d}$ has an undefined critical density.

The shapes of images in the lens plane may be determined by solving Equation (2.8) for all points within an extended source. Because no photons are emitted or absorbed in the process of gravitational deflection, the mapping of an image from the source to lens plane conserves surface brightness:

$$I(\boldsymbol{\theta}) = I_\mathrm{s}[\boldsymbol{\beta}(\boldsymbol{\theta})] \tag{2.14}$$

where I_s is the surface brightness in the source plane. Analogous to the derivation of Equation (2.5), if the source is much smaller than the scale on which the lens changes, the mapping of the source to the image can be treated linearly:

$$I(\boldsymbol{\theta}) = I_\mathrm{s}\left[\boldsymbol{\beta_0} + \mathcal{A}(\boldsymbol{\theta}_0)\cdot(\boldsymbol{\theta}-\boldsymbol{\theta}_0)\right], \tag{2.15}$$

where $\boldsymbol{\theta}_0$ is a point on the image with a corresponding point $\boldsymbol{\beta}_0 = \boldsymbol{\beta}(\boldsymbol{\theta}_0)$ and $\mathcal{A} = \frac{\partial\boldsymbol{\beta}}{\partial\boldsymbol{\theta}}$ describes the distortion of the image by the lens. By considering Equation (2.8) and the Poisson equation (2.13), it can be shown that

$$\frac{\partial\boldsymbol{\beta}}{\partial\boldsymbol{\theta}} = \mathcal{A} = \left(\delta_{ij} - \frac{\partial^2\psi(\boldsymbol{\theta})}{\partial\theta_i\partial\theta_j}\right) \tag{2.16}$$

$$= \begin{pmatrix} 1-\kappa-\gamma_1 & -\gamma_2 \\ -\gamma_2 & 1-\kappa+\gamma_1 \end{pmatrix} \tag{2.17}$$

where we have introduced the complex shear γ, which obeys the following relations:

$$\gamma = \gamma_1 + \imath\gamma_2 = |\gamma| e^{2\imath\vartheta}, \tag{2.18}$$

$$\gamma_1 = \frac{1}{2}\left(\frac{\partial^2\psi}{\partial^2\theta_1} - \frac{\partial^2\psi}{\partial^2\theta_2}\right), \tag{2.19}$$

$$\gamma_2 = \frac{\partial^2\psi}{\partial\theta_1\partial\theta_2}. \tag{2.20}$$

By making one final definition, the reduced shear $g \equiv \gamma/(1-\kappa)$, the mechanism of shape distortions is clear:

$$\mathcal{A} = (1-\kappa)\begin{pmatrix} 1-g_1 & -g_2 \\ -g_2 & 1+g_1 \end{pmatrix}. \tag{2.21}$$

The factor $(1-\kappa)$ stretches the entire image, while the reduced shear introduces ellipticities into the shape.

Along with stretches and distortions, the redirection of light from gravitational lensing results in a net magnification $|\mu(\boldsymbol{\theta_0})| = I(\boldsymbol{\theta})/I_s(\boldsymbol{\beta})$, canonically described for a "small" source by

$$\mu = \frac{1}{\det\mathcal{A}} = \frac{1}{(1-\kappa)^2 - |\gamma|^2}. \tag{2.22}$$

Because one typically does not know the intrinsic luminosity of the sources, the magnification is not directly observable, although one *can* measure the relative magnification through the ratio of two images.

Hence, when measuring the shape distribution by calculating the ratios of the axes, one measures the reduced shear. Further, the reduced shear due to lensing,

$$|g| = \frac{|\gamma|}{1-\kappa}, \tag{2.23}$$

is the same under the change of variables

$$(1-\kappa) \to \lambda(1-\kappa), \qquad \gamma \to \lambda\gamma. \tag{2.24}$$

This is the mass sheet degeneracy (see Gorenstein et al. 1988; Schneider and Seitz 1995), and may intuitively be observed by considering Equation (2.21), where $(1-\kappa)$ stretches the image, but does not affect its shape. If only distortion measurements relative to the background average ellipticity are made (i.e. measurements of $|g|$), then then no information on κ is observed. The mass recovered is therefore not unique; for example, one could add a constant mass density sheet to the lens plane and not distort the observed ellipticity.

It is possible to break this degeneracy by taking into account the magnification, which can be seen to change as λ^{-2} by applying the same change of variables into Equation (2.22). However, this method faces several problems. As mentioned earlier, one does not know the intrinsic intensity of the magnification and instead measures the relative magnifications of several images, effectively canceling the degeneracy. Additionally, special care

needs to be taken in deciding what observables are due to "magnification," and what are due to other phenomena, specifically the clustering of several sources close together. Schneider et al. (2000) compared methods of breaking the degeneracy via maximum likelihood measurements of magnification and shear measurements, concluding that while magnification may be a better discriminator of the slope of a cluster profile when enough information about the background galaxies are accurately known, the shear better discriminates the normalization. They also tried combining both pieces of information, finding that in the absence of reliable external calibrations of the mass, magnification contributes little toward breaking the mass degeneracy. Today, wide field surveys view a field much larger than the clusters of galaxies. At the edge of the field, where no cluster signal is present, κ vanishes, breaking the degeneracy.

The Weak Lensing Regime

In the weak lensing regime, $\kappa, \gamma \ll 1$, and so the reduced shear g is approximately equal to the shear γ. Individual distortions in the weak lensing regime are difficult to observe. In this regime, the shear is linear and may be added together. Clusters enter the weak regime approximately 10 kpc out from the core; closer in, the signal is in the strong regime and cannot be linearly stacked.

It is more illustrative to work in terms of tangential and cross components of shear (or reduced shear) relative to some direction ϕ:

$$\gamma_+ = -\Re\left[\gamma e^{-2\imath\varphi}\right] \tag{2.25}$$

$$\gamma_\times = -\Im\left[\gamma e^{-2\imath\varphi}\right]. \tag{2.26}$$

For image distortions due to gravitational lensing by a single lens, the cross shear will equal zero (Kaiser 1995); individual lensing potentials act radially outwards and lack a mechanism for "curling" the light.

For an axisymmetric matter distribution, the tangential shear may conveniently be related to the convergence, providing a relatively easy trace of mass through observable distortions in galaxy morphology:

$$\gamma_+(\theta) = \bar{\kappa}(\theta) - \kappa(\theta), \tag{2.27}$$

where θ is the angular radius in the plane of the lens and $\bar{\kappa}$ is the mean convergence inside of θ. A generalized form of this relation will prove extremely useful in Section 2.4 and beyond.

2.2 A Brief Detour into Cosmic Distances

Our observations of the gravitational lensing effect are in angular measurements of the sky. However, the meaningful determination of mass distributions requires that those

angular measurements be converted to physical distances. The non-Euclidean nature of our universe complicates this conversion. Because we live in an expanding universe, the distances between comoving objects are constantly changing. Additionally, observations look back in time as they look out in distance. Therefore, specifying the distance between two points entails specifying the *type* of distance, as well as the cosmology used. Throughout the rest of this paper a Friedmann-Walker-Robertson (FRW) metric is assumed, with $(\Omega_M, \Omega_\Lambda, \Omega_\kappa) = (0.25, 0.75, 0)$, and $H_0 = 100h$ km s^{-1} Mpc^{-1}, where h is left as a free parameter, typically of value ~ 0.7.

A useful further reference for the following section is Hogg (1999).

Distance is characterized by the redshift, z, which is the shift in an object's emitted light due to the expansion of the universe and appears effectively as a Doppler shift:[4]

$$z \equiv \frac{\nu_e}{\nu_o} - 1 \tag{2.28}$$

where ν_e is the emitted frequency and ν_o is the observed. For small distances, Euclidean geometry is recovered, so $z \approx \frac{v}{c} = \frac{d}{D_H}$, where $D_H \equiv \frac{c}{H_0}$ is the Hubble distance.

However, at larger distances, one must account for the expansion of the universe. For convenience, define the function

$$E(z) \equiv \sqrt{\Omega_M (1+z)^3 + \Omega_\kappa (1+z)^2 + \Omega_\Lambda}. \tag{2.29}$$

With this function, several types of distances may now be defined:

Comoving Distance The comoving distance D_C between two objects is the distance which remains constant with time if the two objects are moving with the expansion of the universe. This is equivalent to calculating the proper distance divided by the scale factor, or

$$D_C = D_H \int_0^z \frac{dz'}{E(z')}. \tag{2.30}$$

Transverse Comoving Distance The (transverse) comoving distance between two events at the same distance but separated by some angle $\delta\theta$ is $D_M \delta\theta$, where D_M in this paper's cosmology ($\Omega_\kappa = 0$) is

$$D_M = D_C. \tag{2.31}$$

Angular Diameter Distance The angular diameter distance is defined as the ratio between an object's physical transverse size to its angular size in radians. Practically,

[4] One might ask how one separates a Doppler shift due to radial motion from the innate expansion of the universe. The answer is that one can't, but at the extreme distances used here, the expansion of the universe almost certainly dominates. Consider an object with $z = 0.1$. Due to the expansion of the universe its radial velocity is measured to be $\sim 3 \times 10^4$ km/s. For comparison, the Milky Way is moving at order 100 km/s relative to the cosmic microwave background radiation.

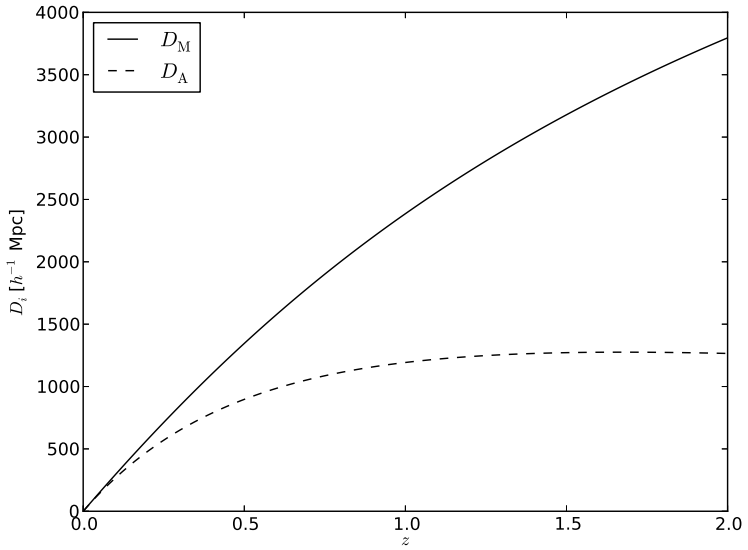

Figure 2.3: A plot of the angular diameter distance and the transverse comoving distance as a function of redshift. In this paper's cosmology, the comoving distance is equivalent to the transverse comoving distance. Notably, the angular diameter distance reaches an inflection point at around $z \sim 1$.

it is used to convert angular separations in telescope images to their proper separations at the source. The angular diameter distance may be written as (Peebles 1993):

$$D_{\rm A} = \frac{D_{\rm M}}{1+z}. \tag{2.32}$$

Note, however, that (unlike the other distances thus far mentioned), the angular diameter distance between two objects at redshifts z_1 and z_2, $D_{\rm A12}$, is *not* the difference between $D_{\rm A1}$ and $D_{\rm A2}$. Instead, for $\Omega_\kappa = 0$, it is (Peebles 1993):

$$D_{\rm A12} = \frac{1}{1+z_2}\left[D_{\rm M2}\sqrt{1+\frac{D_{\rm M1}^2}{D_{\rm H}^2}} - D_{\rm M1}\sqrt{1+\frac{D_{\rm M2}^2}{D_{\rm H}^2}}\right]. \tag{2.33}$$

We will primarily be using the angular diameter distance, which crops up in the critical surface density $\Sigma_{\rm crit}$.

2.3 The Universal Halo Profile

From studying high-resolution N-body simulations, Navarro et al. (1997) discovered an empirical universal density profile for dark matter halos, the Navarro-Frenk-White (NFW) profile, that is dependent only on the parameters c and r_{200}:

$$\rho_{\rm NFW}(r; r_{200}, c) = \frac{\rho_{\rm crit}\delta_{\rm c}}{(r/r_{\rm s})(1+r/r_{\rm s})^2}, \tag{2.34}$$

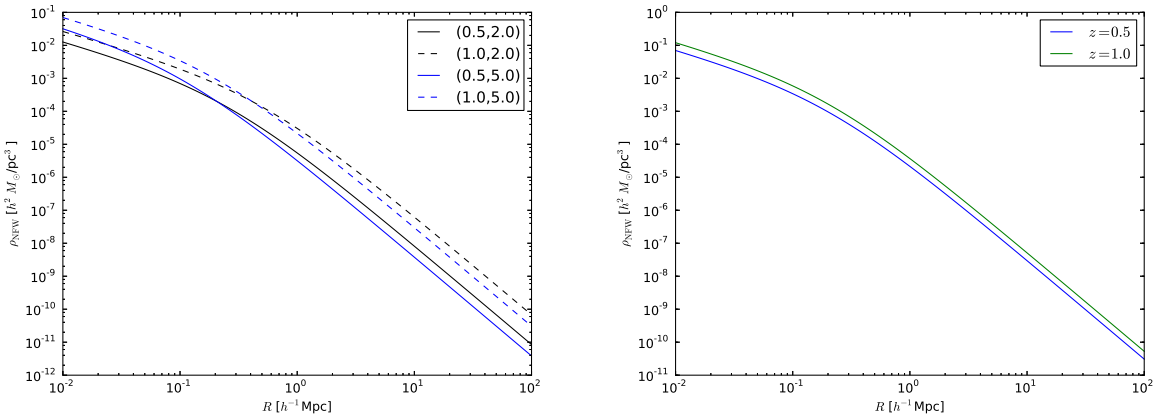

Figure 2.4: The NFW density profile for several combinations of (r_{200}, c). The scale radius, $r_{\rm s} \equiv r_{200}/c$, marks the transition from $\rho \propto r^{-3}$ to $\rho \propto r^{-1}$. Relative to the same r_{200}, an increase in c will decrease the "cuspiness." Additionally, the NFW profile is plotted for different redshifts. An increase in the redshift of the halo increases the critical density, $\rho_{\rm crit}$.

where $\rho_{\rm crit} = 3H(z)^2/8\pi G$ is the critical density for closure at redshift z, $r_{\rm s} = r_{200}/c$ is a scale radius, and $\delta_{\rm c}$ is a characteristic dimensionless density dependent only on c. The radius r_{200} is defined to be the radius within which the average mass density is equal to 200 times the critical mass density, or

$$M_{200} = \frac{4\pi}{3} 200 \rho_{\rm crit} r_{200}^3, \tag{2.35}$$

which then implies

$$\delta_{\rm c} = \frac{200 c^3}{3[\ln(1+c) - c/(1+c)]}. \tag{2.36}$$

For halos of mass $10^{13} - 10^{14} M_\odot$, c is around 5.0 and r_{200} around 1 Mpc. Duffy et al. (2008) used N-body simulations in conjunction with WMAP5 cosmology to constrain $c(M_{200}, z)$. We will be using their results for relaxed halo samples as a function of redshift:

$$c = A(M/M_{\rm pivot})^B (1+z)^C, \tag{2.37}$$

where $(A, B, C, M_{\rm pivot}) = (6.71, -0.091, -0.44, 2 \times 10^{12} h^{-1} {\rm M}_\odot)$.[5]

The profile has become very popular as a "go-to" model for halo mass distributions, although it is not without its detractors (see Merritt et al. 2006; Navarro et al. 2004; Yang et al. 2006; Navarro et al. 2010, for more on that debate). The primary contention is about the "cuspiness" of the central regions of the halo ($r < r_{\rm s}$). Alternative NFW-like profiles

[5] See Figure 2.7. Recall that Equation (2.35) implies that this is equivalent to $c(r_{200}, z)$: $M_{200} = \frac{4\pi}{3} 200 \rho_{\rm crit} r_{200}^3$.

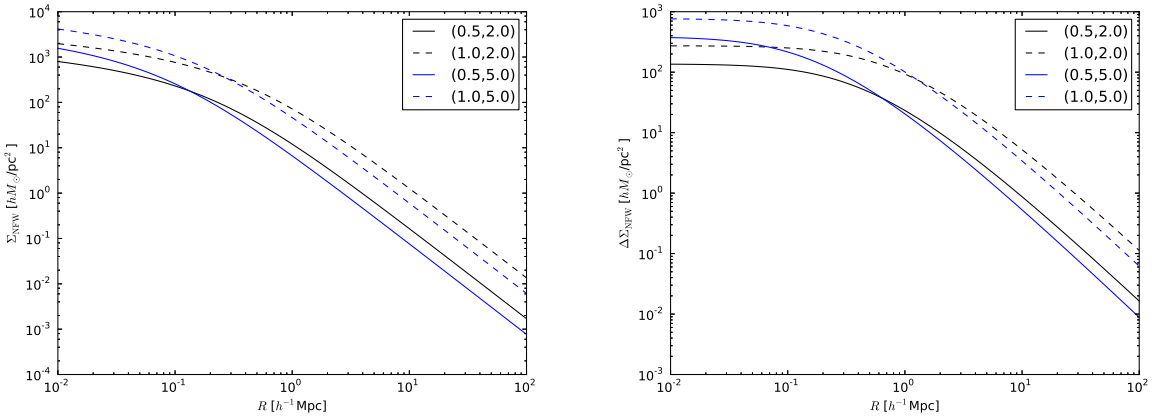

Figure 2.5: The NFW surface density and surface density contrast profiles for several combinations of (r_{200}, c). Of importance is the leveling off of the profile within one scale radius. The profile levels slower with higher concentration.

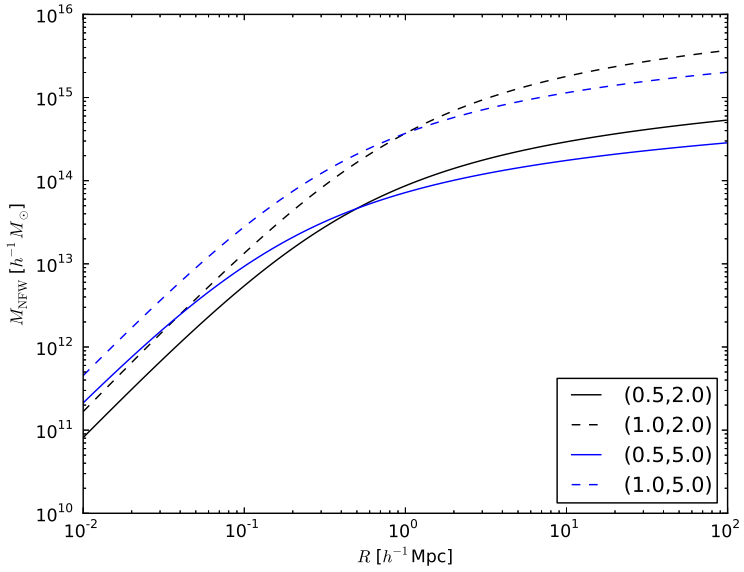

Figure 2.6: The NFW mass profile for several combinations of (r_{200}, c).

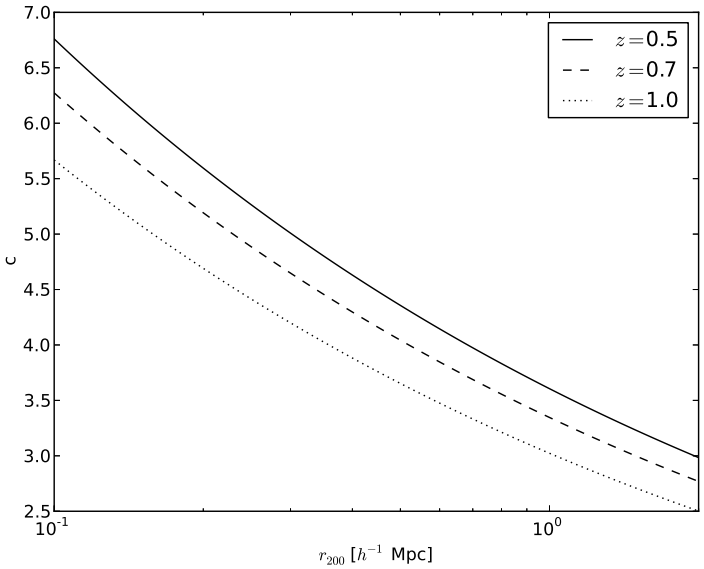

Figure 2.7: Concentration as a function of r_{200} and z (Duffy et al. 2008).

have been proposed that vary the powers in the denominator:

$$\rho_{\mathrm{NFW-Like}}(r; r_{200}, c) = \frac{\rho_{\mathrm{crit}}\delta_{\mathrm{c}}}{(r/r_{\mathrm{s}})^{\alpha}(1 + r/r_{\mathrm{s}})^{\beta}} \tag{2.38}$$

where, for an NFW profile, $(\alpha, \beta) = (1, 2)$ (see Yang et al. 2006). Weak-lensing observations are as yet unable to distinguish between an NFW profile or other alternative NFW-like profiles, although the Singular Isothermal Sphere (SIS) (equivalent to $(\alpha, \beta) = (2, 0)$) may now be ruled out for dark matter haloes (see Wright and Brainerd 2000; Bartelmann et al. 2001; Mandelbaum et al. 2006). Simulations have concluded, however, that systematic deviations from the NFW profile are to be expected and are better approximated by the Einasto formula (Gao et al. 2008).

Of interest to this paper is the projected surface mass density, Σ, as well as the surface mass density contrast, $\Delta\Sigma$. The projected surface mass density is obtained by integrating the three dimensional density profile along the line of sight,

$$\Sigma(y) = 2\int_0^{\infty} \rho\left(\sqrt{x^2 + y^2}; r_{200}, c\right) \mathrm{d}x, \tag{2.39}$$

so

$$\Sigma_{\mathrm{NFW}}(\xi) = 2r_{\mathrm{s}}\delta_{\mathrm{c}}\rho_{\mathrm{crit}}\left[\frac{1}{\xi^2 - 1}\left(1 - \frac{\mathrm{arcsec}(\xi)}{\sqrt{\xi^2 - 1}}\right)\right], \tag{2.40}$$

where $\xi = y/r_{\mathrm{s}}$. The radial dependence of the convergence due to an NFW lens is then $\kappa_{\mathrm{NFW}}(\xi) = \Sigma_{\mathrm{NFW}}(\xi)/\Sigma_{\mathrm{crit}}$.

Because the NFW profile is spherically symmetric,[6] the radial dependence of the shear may be written as

$$\gamma_{\mathrm{NFW},+}(\xi) = \bar{\kappa}_{\mathrm{NFW}}(\xi) - \kappa_{\mathrm{NFW}}(\xi), \tag{2.41}$$

where $\bar{\kappa}_{\mathrm{NFW}}(\xi)$ is the mean convergence inside the the radius ξ,

$$\bar{\kappa}_{\mathrm{NFW}}(\xi) = \frac{2}{\xi^2}\int_0^{\xi} \xi' \kappa_{\mathrm{NFW}}(\xi')\mathrm{d}\xi'. \tag{2.42}$$

In terms of ξ, the surface mass density contrast, $\Delta\Sigma_{\mathrm{NFW}} = \gamma_{\mathrm{NFW},+}\Sigma_{\mathrm{crit}}$, is

$$\Delta\Sigma_{\mathrm{NFW}}(\xi) = 2r_{\mathrm{s}}\delta_{\mathrm{c}}\rho_{\mathrm{crit}}\left[\frac{2}{\xi^2}\left(\frac{\mathrm{arcsec}(\xi)}{\sqrt{\xi^2-1}} + \ln(\xi/2)\right) - \frac{1}{\xi^2-1}\left(1 - \frac{\mathrm{arcsec}(\xi)}{\sqrt{\xi^2-1}}\right)\right] \tag{2.43}$$

This model differs from other conventional presentations of the NFW surface density profile (e.g., Wright and Brainerd 2000) in that the arcsecant function is used instead of the arctangent or hyperbolic arctangent functions, depending on the value of ξ. In the other formalism, three different cases must be presented, for ξ greater than, equal to, and less than one. The formalism used here is better equipped for numerical artifacts and "dips" that may arise near $\xi = 1$. As ξ traverses the apparent discontinuity at $\xi = 1$, $\lim_{x\to 1} \mathrm{arcsec}(\xi)/\sqrt{\xi^2-1} = 1$, and so the discontinuity is avoided. Σ and $\Delta\Sigma$ are always real; any imaginary terms will arise solely from numerical defects.

2.4 From Shear to Mass

Derivation of Mass Profile from Tangential Shear

Remarkably, Equation (2.27) also holds for general matter distributions, albeit slightly modified.[7] Recalling Equation (2.13) from Section 2.1, that the convergence κ is related to the deflection potential ψ by $\nabla^2\psi = 2\kappa$, we can use Gauss's Law to relate the integral of the convergence around a circle of radius θ to the gradient of the deflection potential:

$$\int_0^{\theta} \mathrm{d}^2\boldsymbol{\vartheta}\, \nabla^2\psi = \int_0^{\theta} \mathrm{d}^2\boldsymbol{\vartheta}\, 2\kappa = \theta \oint \mathrm{d}\varphi\, \nabla\psi \cdot \boldsymbol{n}, \tag{2.44}$$

where $\boldsymbol{n}$ is the outward normal on the circle. Noting that $\nabla\psi \cdot \boldsymbol{n} = \frac{\partial\psi}{\partial\theta}$ we can define a function $m(\theta)$:

$$m(\theta) \equiv \frac{1}{\pi}\int_0^{\theta} \mathrm{d}^2\boldsymbol{\vartheta}\, \kappa = \frac{\theta}{2\pi}\oint \mathrm{d}\varphi\, \frac{\partial\psi}{\partial\theta'}, \tag{2.45}$$

where m is only a function of θ. Differentiating this equation with respect to θ gives

$$\frac{\mathrm{d}m}{\mathrm{d}\theta} = \frac{m}{\theta} + \frac{\theta}{2\pi}\oint \mathrm{d}\varphi\, \frac{\partial^2\psi}{\partial\theta'^2}. \tag{2.46}$$

[6] See Section 2.5 below, when the elliptical NFW profile is considered. The formalisms here still hold because the ellipticity is parameterized to be aligned with the lens plane on average.

[7] The following derivation is also outlined in Schneider (2006b).

This is the crucial step: if we consider a point on the θ_1-axis, then

$$\frac{\partial^2\psi}{\partial\theta^2} = \frac{\partial^2\psi}{\partial\theta_1^2} = \kappa + \gamma_1 = \kappa - \gamma_+, \tag{2.47}$$

where γ_+ is the tangential shear. But the convergence and the tangential shear are independent of the choice of coordinate system because they are axisymmetric and must therefore hold for all θ. If this is the case, then the convergence and tangential shear at any vector $\boldsymbol{\theta}$ is equal to the average on the circle radius θ :

$$\kappa(\theta) - \gamma_+(\theta) = \langle\kappa(\theta)\rangle - \langle\gamma_+(\theta)\rangle \tag{2.48}$$

and therefore

$$\frac{1}{2\pi}\frac{\partial^2\psi}{\partial\theta^2} = \langle\kappa(\theta)\rangle - \langle\gamma_+(\theta)\rangle. \tag{2.49}$$

We may then rewrite Equation (2.46):

$$\frac{\mathrm{d}m}{\mathrm{d}\theta} = \frac{m}{\theta} + \theta\left[\langle\kappa(\theta)\rangle - \langle\gamma_+(\theta)\rangle\right]. \tag{2.50}$$

Inside a circle radius θ, $m(\theta)$ and $\frac{\mathrm{d}m}{\mathrm{d}\theta}$ may be written as

$$m(\theta) = 2\int_0^\theta \mathrm{d}\theta\ \theta\langle\kappa(\theta)\rangle \tag{2.51}$$

$$= \theta^2\langle\kappa(\leq\theta)\rangle \tag{2.52}$$

$$\frac{\mathrm{d}m}{\mathrm{d}\theta} = 2\theta\langle\kappa(\theta)\rangle. \tag{2.53}$$

After dividing Equation (2.46) through θ, we obtain the desired relation,

$$\langle\gamma_+(\theta)\rangle = \langle\kappa(\leq\theta)\rangle - \langle\kappa(\theta)\rangle. \tag{2.54}$$

which is very similar to Equation (2.27) for axisymmetric mass distributions. An important implication then is that even if the density is not axisymmetric, the azimuthally-averaged mass profile may still be measured from the average tangential shear.

The Galaxy Mass Correlation Function

The Galaxy Mass Correlation Function (GMCF) relates the shear distortion of galaxies behind a lens to the mass distribution of the lens. Whereas Equation (2.27) relates the dimensionless quantities γ_+ and κ over angular distances, the GMCF relates shape distortions to the mass distribution over physical distances. Start from Equation (2.27) and multiply by the critical density

$$\Sigma_{\mathrm{crit}} = \frac{c^2 D_{\mathrm{s}}}{4\pi G D_{\mathrm{d}} D_{\mathrm{ds}}}, \tag{2.55}$$

where D_s, D_d, and D_{ds} are the angular diameter distances to the source, lens, and between the lens and source.[8] By substituting $\theta = D_d R$, where R is the physical distance from the lens in the plane of the lens, one obtains the GMCF $\Delta\Sigma(R)$:

$$\Delta\Sigma(R) = \langle\Sigma(\leq R)\rangle - \langle\Sigma(R)\rangle. \tag{2.56}$$

The Mass Profile

In this section we relate the GMCF to the surface mass density and, through an inverse Abel inversion, derive a relation between the GMCF and the mass profile.

Start from Equation (2.27) and take derivatives with respect to y:[9]

$$\gamma'_+ = \bar{\kappa}' - \kappa'. \tag{2.57}$$

But $\bar{\kappa}$ is the average mass density out to some radius y:

$$\bar{\kappa}(y) = \frac{\int_0^y \kappa(r) 2\pi r \mathrm{d}r}{\pi y^2}, \tag{2.58}$$

so by the Leibniz integral rule,

$$\bar{\kappa}'(y) = -\frac{2\int_0^y \kappa(r) 2\pi r \mathrm{d}r}{\pi y^3} + \frac{\kappa(y) 2\pi y}{\pi y^2} = -\frac{2\bar{\kappa}(y)}{y} + \frac{2\kappa(y)}{y}. \tag{2.59}$$

Therefore, Equation (2.57) may be rewritten

$$\gamma'_+ = -\kappa' + -\frac{2}{y}(\bar{\kappa} - \kappa) \tag{2.60}$$

which may be combined with Equation (2.27) and multiplied by the critical density (Equation (2.55)) to obtain a relation between the surface mass density Σ and the GMCF $\Delta\Sigma$:

$$-\Sigma' = \frac{2}{y}\Delta\Sigma + \Delta\Sigma'. \tag{2.61}$$

The inverse Abel transform recovers the cylindrical projection $\Sigma(y)$ of a spherically-symmetric function $\rho(r)$:

$$\rho(r) = \frac{1}{\pi}\int_r^\infty \frac{-\Sigma' \mathrm{d}y}{\sqrt{y^2 - r^2}}. \tag{2.62}$$

In this situation, assuming spherical symmetry, the inverse Abel transform of the GMCF finds the three dimensional mass density contrast, $\Delta\rho = \rho - \bar{\rho}$, where $\bar{\rho}$ is the background

[8] See Section 2.1.

[9] Let primes denote the derivative with respect to y, that is, $\gamma'_+ \equiv \frac{\mathrm{d}\gamma_+}{\mathrm{d}y}$.

density not due to the halo and is negligibly small around the halo. Using Equation (2.61), Equation (2.62) may be written as

$$\Delta\rho(r) = \frac{1}{\pi}\int_r^\infty \frac{2\Delta\Sigma(y)}{y\sqrt{y^2-r^2}} + \frac{\Delta\Sigma'(y)}{\sqrt{y^2-r^2}}\mathrm{d}y \tag{2.63}$$

(Deutsch and Beniaminy 1982). The second part of Equation (2.63) may be integrated by parts to give an expression in terms of $\Delta\Sigma$:

$$\int_r^\infty \frac{\Delta\Sigma'(y)\mathrm{d}y}{\sqrt{y^2-r^2}} = \lim_{\alpha\to\infty} \frac{\Delta\Sigma(y)}{\sqrt{y^2-r^2}}|_r^\alpha + \int_r^\alpha \frac{\Delta\Sigma(y)y\mathrm{d}y}{(y^2-r^2)^{3/2}}. \tag{2.64}$$

Keeping careful track of indices, we note

$$\frac{\Delta\Sigma(y)}{\sqrt{y^2-r^2}}|_r^\alpha = \frac{\Delta\Sigma(\alpha)-\Delta\Sigma(r)}{\sqrt{\alpha^2-r^2}} + \frac{\Delta\Sigma(r)}{\sqrt{y^2-r^2}}|_r^\alpha. \tag{2.65}$$

But we note that, as α approaches infinity, the first term is just zero and may be neglected. We are left with

$$\int_r^\infty \frac{\Delta\Sigma'(y)\mathrm{d}y}{\sqrt{y^2-r^2}} = \int_r^\infty \frac{(\Delta\Sigma(y)-\Delta\Sigma(r))y\mathrm{d}y}{(y^2-r^2)^{3/2}}. \tag{2.66}$$

The three dimensional mass density contrast is now entirely in terms of the GMCF:

$$\Delta\rho(r) = \frac{1}{\pi}\int_r^\infty \frac{2\Delta\Sigma(y)\mathrm{d}y}{y\sqrt{y^2-r^2}} + \frac{1}{\pi}\int_r^\infty \frac{(\Delta\Sigma(y)-\Delta\Sigma(r))y\mathrm{d}y}{(y^2-r^2)^{3/2}}. \tag{2.67}$$

Neglecting the background mass density, the total mass contained within a radius y is simply given in terms of $\Delta\rho$ as

$$M(y) = \int_0^y 4\pi r^2\Delta\rho\mathrm{d}r, \tag{2.68}$$

which may be calculated as a set of discrete sums out to a finite distance where the GMCF is approximately zero.

In practice, we do not have information out to $r=\infty$. Instead, we must cut off our radius at $y_{\max}$ and so we cannot assume that $(\Delta\Sigma(\alpha)-\Delta\Sigma(r))/\sqrt{\alpha^2-r^2}$ goes to zero. The GMCF is then given by

$$\begin{aligned}\Delta\rho(r) =& \frac{1}{\pi}\frac{\Delta\Sigma(y_{\max})-\Delta\Sigma(r)}{\sqrt{y_{\max}^2-r^2}} + \frac{1}{\pi}\int_r^{y_{\max}} \frac{2\Delta\Sigma(y)\mathrm{d}y}{y\sqrt{y^2-r^2}} + \\ & \frac{1}{\pi}\int_r^{y_{\max}} \frac{(\Delta\Sigma(y)-\Delta\Sigma(r))y\mathrm{d}y}{(y^2-r^2)^{3/2}} + \frac{1}{\pi}E(r,y_{\max}),\end{aligned} \tag{2.69}$$

where $E(y_{\max})$ is the error arising from cutting the signal off at some maximum radius and which may be calculated by taking the difference between true and measured $\Delta\rho(r)$, leading to

$$E(r,y_{\max}) = \int_{y_{\max}}^\infty \frac{2(2y^2-r^2)}{y(y^2-r^2)^{3/2}}\Delta\Sigma(y)\mathrm{d}y. \tag{2.70}$$

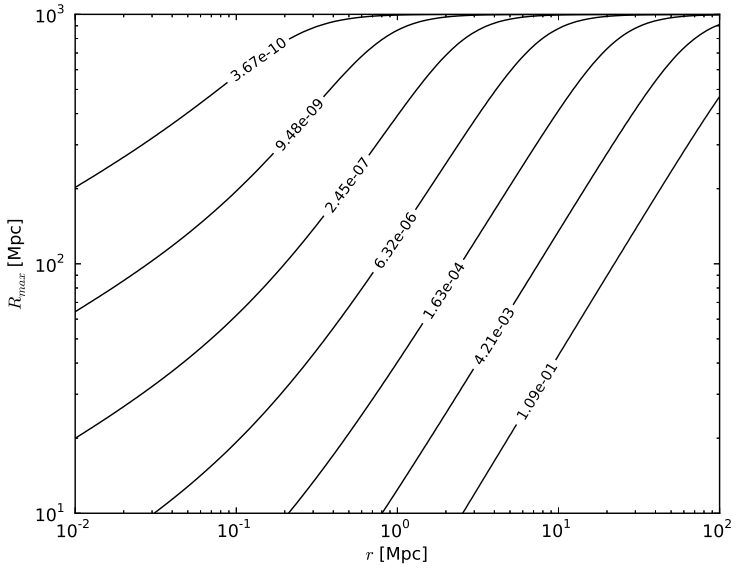

Figure 2.8: Contour plot of the fractional error $\frac{E}{\Delta\rho}(r, R_{\max})$ as a function of radius examined and maximum radius out to which the signal is observed for an NFW halo with $M_{200} = 10^{14} M_\odot$ and $z = 0.5$. As the maximum radius increases, the errors decrease. As the radius examined approaches that maximum radius, the errors will increase because the error function E now covers a much larger proportion of the signal.

Additionally, when calculating the mass, the density distribution is known only to some minimum radius $y_{\min}$. Therefore the mass profile is

$$M(y) = M(y_{\min}) + \int_{y_{\min}}^{y} 4\pi r^2 \Delta\rho \mathrm{d}r, \tag{2.71}$$

where $M(y_{\min})$ is the mass contained within the minimum radius $y_{\min}$.

In order to obtain this inner mass, we recall that the average surface mass density inside some radius y is equivalent to the mass of some cylinder m_{cyl} at radius y divided by the area πy^2. Therefore, we may rewrite Equation (2.56):

$$\Delta\Sigma(y) = \langle \Sigma(\leq y) \rangle - \langle \Sigma(y) \rangle \tag{2.72}$$

$$= \frac{m_{\mathrm{cyl}}(y)}{\pi y^2} - \langle \Sigma(y) \rangle. \tag{2.73}$$

Next we recall that the inverse form of the Abel inversion formula Equation (2.62) is

$$\Sigma(y) = 2 \int_y^\infty r \frac{\Delta\rho(r)}{\sqrt{r^2 - y^2}} \mathrm{d}r. \tag{2.74}$$

Substituting (2.74) and manipulating (2.73) leads to a relation between $\Delta\Sigma, \Delta\rho$ and $m_{\rm cyl}$:

$$m_{\rm cyl}(y) = \pi y^2 \left[\Delta\Sigma(y) + 2\int_y^\infty {\rm d}r\, r \frac{\Delta\rho(r)}{\sqrt{r^2 - y^2}} \right]. \tag{2.75}$$

This is convenient because $m_{\rm cyl}$ may be used to give the mass contained inside radius $y_{\rm min}$ which otherwise cannot be obtained by naively integrating $\Delta\rho$. We may now relate the cylindrical mass $m_{\rm cyl}(y)$ to the (assumed spherical) three dimensional mass $M(r = y)$ (henceforth written as $M(y)$), which is just the mass contained in $m_{\rm cyl}$ minus the mass inside the cylinder but outside the sphere:

$$M(y) = m_{\rm cyl}(y) - 4\pi \int_0^y x{\rm d}x \int_{\sqrt{y^2 - x^2}}^\infty {\rm d}y\, \Delta\rho(r) \tag{2.76}$$

$$= m_{\rm cyl}(y) - 4\pi \int_y^\infty {\rm d}r\, r\Delta\rho(r) \left[r - \sqrt{r^2 - y^2} \right], \tag{2.77}$$

where the y-axis is the axis of projection. Using Equation (2.77) in Equation (2.71) gives

$$M(y) = F(y_{\rm min}, y_{\rm max}) + G(y_{\rm min}, y_{\rm max}) + \int_{y_{\rm min}}^y 4\pi r^2 \Delta\rho(r){\rm d}r, \tag{2.78}$$

where F and G are constant mass contributions depending on the range of radii investigated:

$$F(y_{\rm min}, y_{\rm max}) = \pi y_{\rm min}^2 \Delta\Sigma(y_{\rm min}) + \int_{y_{\rm min}}^{y_{\rm max}} 2\pi r\Delta\rho(r) \left[\frac{2r^2 - y_{\rm min}^2}{\sqrt{r^2 - y_{\rm min}^2}} - 2r \right] {\rm d}r; \tag{2.79}$$

$$G(y_{\rm min}, y_{\rm max}) = \int_{y_{\rm max}}^\infty 2\pi r\Delta\rho(r) \left[\frac{2r^2 - y_{\rm min}^2}{\sqrt{r^2 - y_{\rm min}^2}} - 2r \right] {\rm d}r. \tag{2.80}$$

While F is a known constant mass contribution that may be determined from the above inversion procedure, G depends on signals outside the observed radii. Figure 2.9 indicates that F is important only at low radii. However, as Figure 2.9 also demonstrates, the contribution of G in general is quite small as to be negligible. Interestingly, then, the largest uncertainty with this method of integration lies in the mass density and not in the final mass obtained.

This method may be contrasted with Johnston et al. (2007a), who do not integrate the derivative and instead calculate the derivative from the slope of a log-log interpolation between points on the GMCF. Figure 2.11 through Figure 2.14 compare the two methods with no added errors, while Figure 2.15 through Figure 2.16 add Gaussian errors at the 5% level. The derivative-less method finds less mass than the method outlined in Johnston et al. (2007a). The differences are not dramatic; the derivative of $\Delta\Sigma$ is largely stable closer in to the halo, while the large oscillations at the edge of the halo only negligibly affect the mass profile.

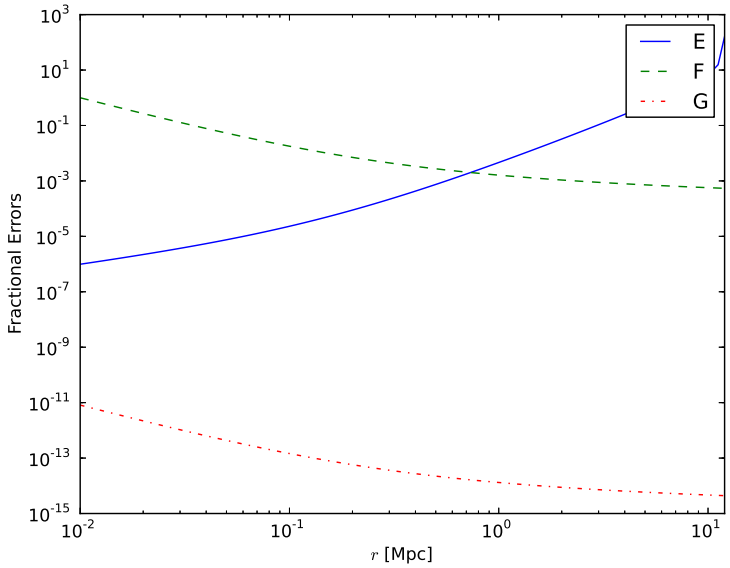

Figure 2.9: Fraction of total density and mass for functions E, F, G with $M_{200} = 10^{14} M_{\odot}$, $z = 0.5$, and $(y_{\min}, y_{\max}) = (0.01, 12) h^{-1}$ Mpc. As expected, F ($\sim$ the mass fraction inside radius $y_{\min}$) starts at one. In contrast, E (the error in the $\Delta\rho$ profile due to a finite maximum radius), starts small and grows to a large proportion at around 5 Mpc. G ($\sim$ the mass obtained by considering the density profile outside of the maximum radius) is extremely small as to be negligible; most of the mass signal resides within our choice of maximum radius.

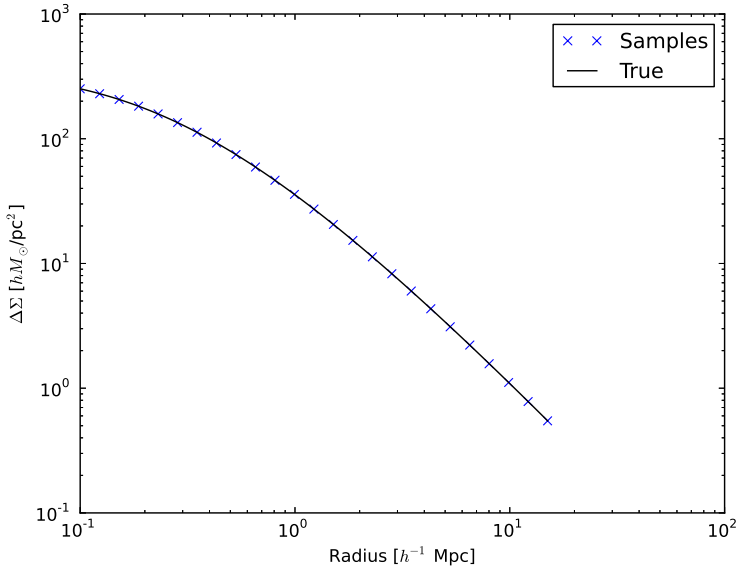

Figure 2.10: This figure plots the sampled points from Sheldon et al. (2004) for a surface mass density contrast profile.

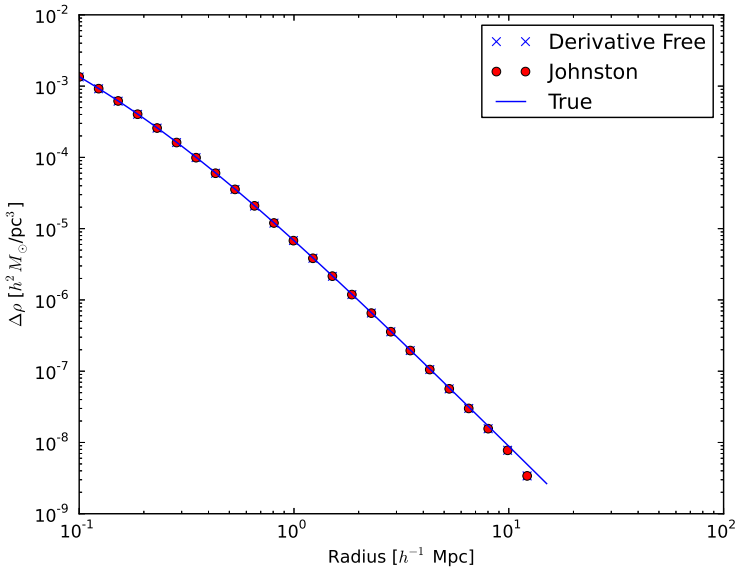

Figure 2.11: This figure plots the analytic NFW density profile along with the derivative-less and method outlined in Johnston et al. (2007a) for reconstructing the density profile. Both recover the expected analytic profile quite well.

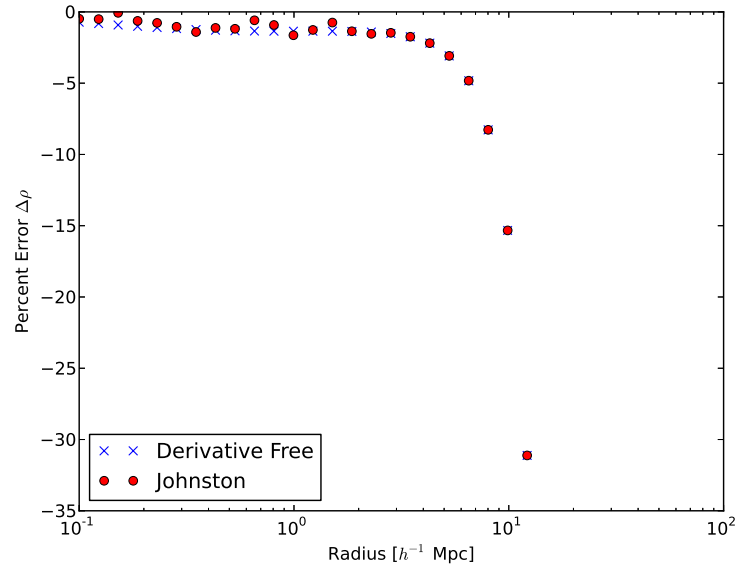

Figure 2.12: This figure plots the percent difference in value with the true for both the derivative-less and the method outlined in Johnston et al. (2007a) for $\Delta\rho$. Significantly, the reconstructions become wildly inaccurate at larger radii as fewer and fewer data points are available for integration.

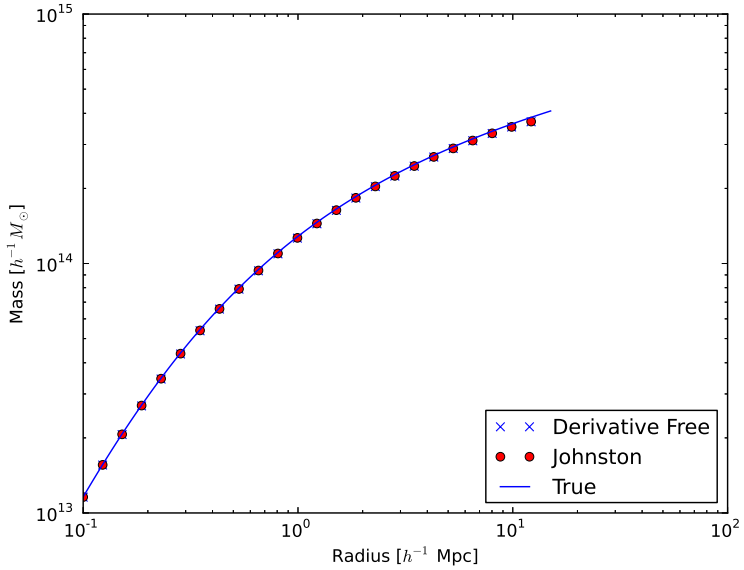

Figure 2.13: This figure plots the analytic NFW mass profile along with the derivative-less and method outlined in Johnston et al. (2007a) for reconstructing the mass profile.

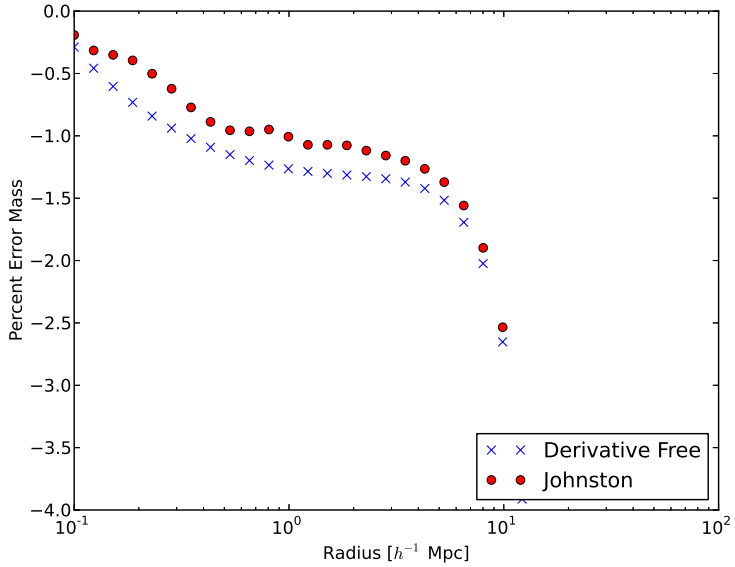

Figure 2.14: This figure plots the percent difference in value with the true for both the derivative-less and the method outlined in Johnston et al. (2007a) for M. The errors are much smaller than Figure 2.12, although they again drop off at larger radii.

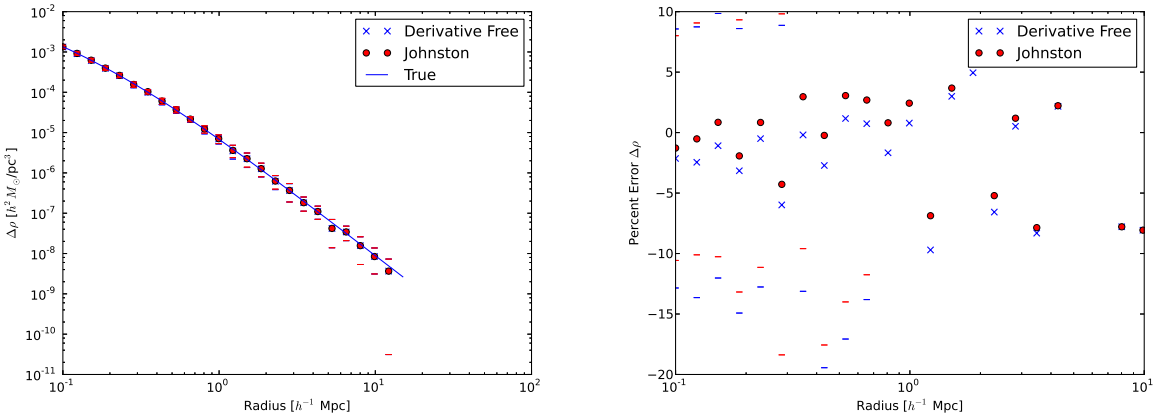

Figure 2.15: A 5% Gaussian error is added and realized 25 different times. Here we plot the mean of the realizations. Notice that errors in the $\Delta\Sigma$ propagate through both versions significantly, although the derivative-less version in generally find one percent less mass than method outlined in Johnston et al. (2007a), regardless of whether the latter over- or underestimates the mass.

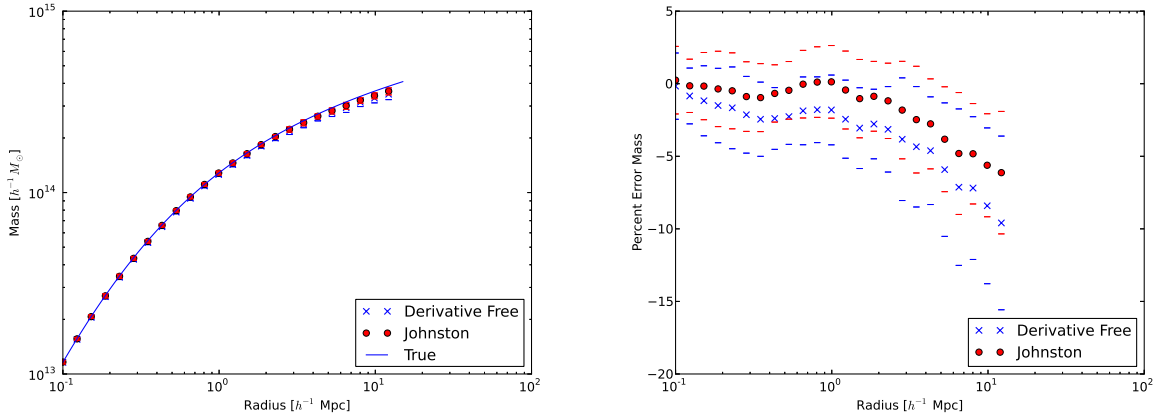

Figure 2.16: A 5% Gaussian error is added. The derivative-less version calculates a smaller mass than the method outlined in Johnston et al. (2007a). Significantly, the major errors present in Figure 2.15 disappear; the 5% error in the measurement of $\Delta\Sigma$ is not exacerbated in the mass measurement.

2.5 Ellipticity Bias

There is no reason a cluster should be spherical. However, in the absence of systematic errors, there is no reason why the aggregate of several clusters should *not* be spherical; a truly random sample of clusters would have no preferred orientation and so the mean profile should appear spherical. Unfortunately, the real world is not so simple: in local patches of the sky, large scale structure may create local orientation preferences. More important to wide area surveys are the orientation biases that result from the selection of clusters and the assignment of richness. Prolate [10] clusters are easier to locate in the sky than oblate (pancake-shaped) clusters because more galaxies are concentrated in a smaller area of the sky. This means that, in general, one expects the average shape of identified clusters to be prolate. For similar reasons, cluster finders tend to find more galaxies in a prolate clusters, leading to an assignment of richness (roughly, the number of galaxies in a cluster) that is biased high; prolate clusters will appear richer than oblate clusters. Thus, orientation biases may also have a richness dependence. This is important because richness is often used as a trace for mass, so clusters with mis-identified richnesses may contaminate the mass calibrations.

In this section we see how we can measure orientation biases in the selection of clusters from weak lensing measurements, and specifically how these orientation biases affect resulting measurements of the lensing signal and the reconstructed mass profile. We outline the method using the elliptical NFW profile,[11] although we shall see that the results are general.

Start with the NFW profile (Navarro et al. 1997) which may be written

$$\rho_{\rm NFW}(r;r_{\rm s}) = \frac{\delta_{\rm c}\rho_{\rm crit}r_{\rm s}^3}{r(r_{\rm s}+r)^2}, \tag{2.81}$$

where $r_{\rm s} \equiv r_{200}/c$ is the scale radius, $\delta_{\rm c}$ is a characteristic density dependent on the local concentration parameter, and $\rho_{\rm crit} = 3H^2/8\pi G$ is the critical density for closure.

Define the elliptical radius of the NFW halo as

$$r^2 = x^2 + q^2y^2, \tag{2.82}$$

where $q^2 > 1$ is prolate, $q^2 < 1$ is oblate, and $q^2 = 1$ is spherical.

The surface mass density is obtained from the Abel transform in Equation (2.74) which may be fully written out using Equation (2.81) as

$$\Sigma(y;r_{\rm s}) = 2\int_0^\infty {\rm d}x\, \rho(\sqrt{x^2+q^2y^2};r_{\rm s}) \tag{2.83}$$

$$= 2\int_0^\infty {\rm d}x\, \frac{\delta_{\rm c}\rho_{\rm crit}r_{\rm s}^3}{\sqrt{q^2y^2+x^2}(r_{\rm s}+\sqrt{q^2y^2+x^2})^2}, \tag{2.84}$$

where we have substituted Equation (2.82) into the form of the NFW profile.

[10] Cigar-shaped with regard to our line of sight.

[11] For other references on the subject of elliptical NFW profiles, see Corless and King (2007).

Now we want to obtain $\Sigma' = \frac{d\Sigma}{dy}$. Taking the derivative with respect to y, we find

$$\Sigma'(y;r_s) = -2\int_0^\infty dx\, q^2 y \rho(\sqrt{x^2+q^2y^2};r_s)\frac{3\sqrt{q^2y^2+x^2}+r_s}{\sqrt{q^2y^2+x^2}(\sqrt{q^2y^2+x^2}+r_s)}, \tag{2.85}$$

which, using the polar substitution from Equation (2.82), may be rewritten as

$$\Sigma'(y;r_s) = -2q^2 y\rho_0 r_s^3 \int_{qy}^\infty \frac{dr}{r^2\sqrt{r^2-q^2y^2}}\frac{3r+r_s}{(r+r_s)^3} \tag{2.86}$$

$$= -2q^2 y \int_{qy}^\infty \frac{dr}{r\sqrt{r^2-q^2y^2}}\frac{3r+r_s}{r+r_s}\rho_{NFW}(\sqrt{x^2+q^2y^2};r_s). \tag{2.87}$$

Next we wish to find the inverse Abel transform of this mass profile, assuming spherical symmetry:

$$\rho^{inv}_{NFW}(r;q,r_s) = -\frac{1}{\pi}\int_r^\infty \frac{dy}{\sqrt{y^2-r^2}}\Sigma' \tag{2.88}$$

$$= \frac{2}{\pi}\rho_c r_s^3 q^2 \int_r^\infty \frac{y dy}{\sqrt{y^2-r^2}}\int_{qy}^\infty \frac{dr}{r^2\sqrt{r^2-q^2y^2}}\frac{3r+r_s}{(r+r_s)^3}, \tag{2.89}$$

where we have substituted in the NFW profile into ρ in Equation (2.89). However, this may be rewritten in terms of an NFW profile using the substitutions $qu = r$ and $qu_s = r_s$:

$$\rho^{inv}_{NFW}(r;q,r_s) = \frac{2q\delta_c\rho_c u_s^3}{\pi}\int_r^\infty \frac{y dy}{\sqrt{y^2-r^2}}\int_y^\infty \frac{du}{u^2\sqrt{u^2-y^2}}\frac{3u+u_s}{(u+u_s)^3} \tag{2.90}$$

$$= \frac{2q}{\pi}\int_r^\infty \frac{y dy}{\sqrt{y^2-r^2}}\int_y^\infty \frac{du}{u\sqrt{u^2-y^2}}\frac{3u+u_s}{(u+u_s)}\rho_{NFW}(u;r_s/q) \tag{2.91}$$

But Equation (2.91) is really the formula for a spherical NFW profile:

$$\rho^{inv}_{NFW}(r;q,r_s) = -\frac{q}{\pi}\int_r^\infty \frac{\Sigma'(y;u_s=r_s/q)dy}{\sqrt{y^2-r^2}} \tag{2.92}$$

$$= q\rho_{NFW}(r;r_s/q). \tag{2.93}$$

Equation (2.93) indicates that if there is an ellipticity in the aggregate NFW profile (for example, from a systematic selection of "richer" appearing clusters), the observed profile is similar to an NFW profile multiplied by the ellipticity with an observed r_{200} that is also proportional to the ellipticity. Thus, if one knows the true r_{200} (as in N-body simulations), then it is possible to directly measure the ellipticity through weak lensing simulations via this relation. Even if this information is not known, this method makes it quite simpler to estimate the error in mass that elliptical biases propagate.

It is perhaps more intuitive to consider the implications in terms of mass instead of size. Because $r_s = r_{200}/c$ and $M_{200} = 200\frac{4\pi}{3}r_{200}^3\rho_{crit}$, it is also possible to interpret this

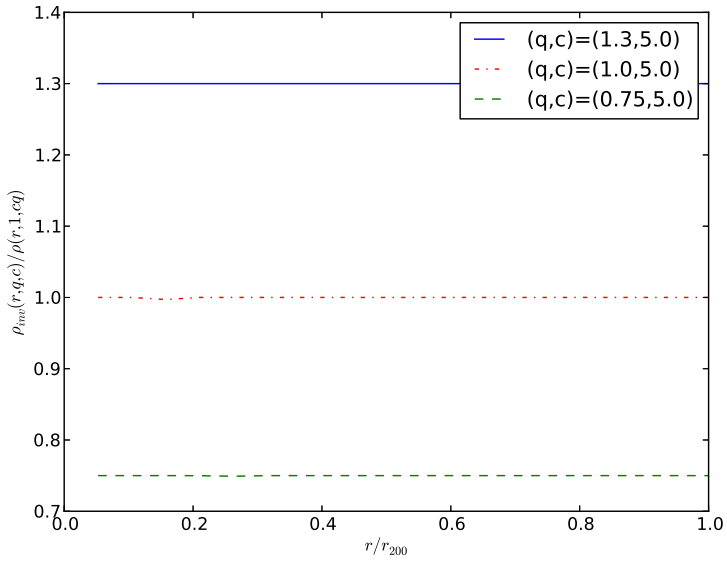

Figure 2.17: This figure compares the numerical integration of the spherical inversion of an elliptical NFW profile with the spherical scaled NFW profile, verifying Equation (2.93).

relation as, instead of a reduction in observed size, as a reduction in observed mass. The resulting ratio in masses at the true r_{200} radius may be written as:

$$M_{200,\rm obs}/M_{200} = q^{-2}\left[\ln(1+cq) - \frac{cq}{1+cq}\right] / \left[\ln(1+c) - \frac{c}{1+c}\right]. \tag{2.94}$$

Figure 2.18 and Figure 2.19 illustrate the over and under estimation of the mass for a single concentration parameter and for a wide parameter space for q and c.

Another interesting result is that this relation holds for generalized density relations like Equation (2.38):

$$\rho_{\rm NFW-Like}(r;r_{\rm s}) = \frac{\rho_{\rm crit}\delta_{\rm c}}{(r/r_{\rm s})^{\alpha}(1+r/r_{\rm s})^{\beta}} \tag{2.95}$$

The only modification occurs in Equation (2.87):

$$\Sigma'(y;r_{\rm s}) = -2q^2 y\int_{qy}^{\infty}\frac{{\rm d}r}{r\sqrt{r^2-q^2y^2}}\frac{(\alpha+\beta)r+\alpha r_{\rm s}}{r+r_{\rm s}}\rho_{\rm NFW-Like}(\sqrt{x^2+q^2y^2};r_{\rm s}). \tag{2.96}$$

The explanation arises by considering the chain rule in the calculation of Σ', which may be rewritten as:

$$\Sigma' = 2\int_{qy}^{\infty}\left({\rm d}r\frac{{\rm d}x}{{\rm d}r}\right)\left(\frac{{\rm d}\rho}{{\rm d}r}\frac{{\rm d}r}{{\rm d}y}\right) \tag{2.97}$$

$$= 2\int_{\rho_i}^{\rho_f}{\rm d}\rho\,\frac{{\rm d}x}{{\rm d}y}, \tag{2.98}$$

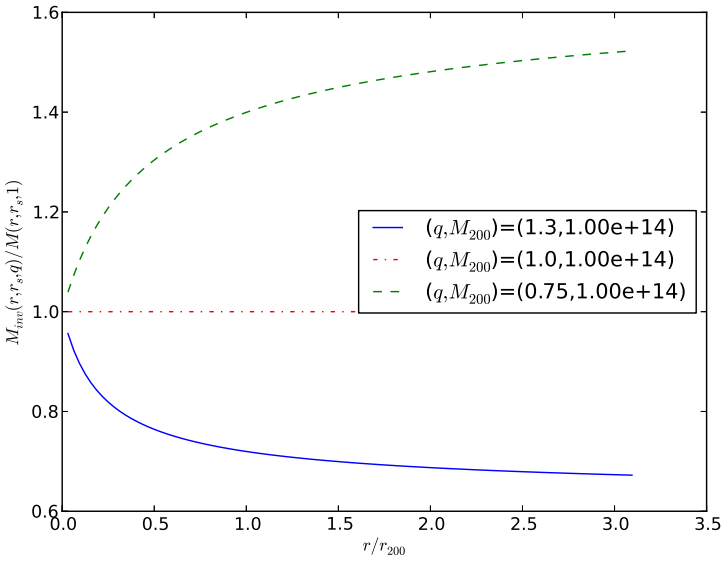

Figure 2.18: This figure compares the observed mass from an assumed spherical inversion of an elliptical NFW profile with the mass contained inside a spherical NFW profile with the same properties otherwise as a function of radius.

where ρ_i and ρ_f are the densities at qy and ∞, respectively. However, the differential $\mathrm{d}\rho$ does not gain or lose any powers of q through the coordinate transformation $(r;r_\mathrm{s}) \rightarrow (qu;qu_\mathrm{s})$.[12] The power of q comes entirely from the ellipticity relation $r^2 = x^2 + q^2y^2 = q^2u^2$, such that $\mathrm{d}x/\mathrm{d}y = -qy/\sqrt{u^2-y^2}$.

This result is general: any elliptical function $\rho_{\rm Elliptical}(r;q,r_\mathrm{s})$ corresponding to some spherically-symmetric density function $\rho_{\rm Spherical}(r;r_\mathrm{s})$, when naively integrated as a sphere, will appear as $q\rho_{\rm Spherical}(r;r_\mathrm{s}/q)$, where r_s sets the scale length. So for example, the singular isothermal sphere profile may be rewritten

$$\rho(r) = \frac{A}{2\pi G}\left(\frac{r}{r_\mathrm{s}}\right)^{-2}, \tag{2.99}$$

where $Ar_\mathrm{s}^2 = \sigma_V^2$.[13] The natural result (that the inferred mass scales as q^{-1}) quickly follows. The clear advantage of this method of analysis is that it quickly identifies the effects of this type of ellipticity on the measured mass profile for any density profile. However, because q is difficult to measure from the mass profile alone, it must be used in conjunction with other information to obtain quantitative results.

[12] A coordinate transformation does not – can not – change an observable.

[13] The singular isothermal sphere is just a generalized NFW with $(\alpha,\beta) = (-2,0)$.

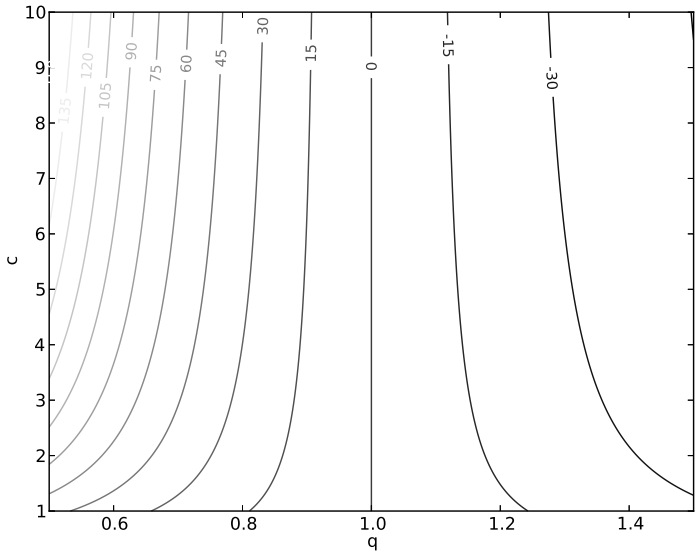

Figure 2.19: This figure compares the observed mass from an assumed spherical inversion of an elliptical NFW profile with the mass contained inside a spherical NFW profile with the same properties otherwise as a function of the concentration parameter and the ellipticity at $r = r_{200}$. The contours plot the percent difference of the recovered mass from the true mass.

Chapter 3

Methods

3.1 Data

The Dark Energy Survey Mock Catalogs (DES Mocks) are the results of N-body simulations conducted in preparation of the Dark Energy Survey for the purpose of checking systematics as well as for developing accurate and powerful scientific numerical tools in preparation of actual observational data. The data in this thesis comes from version 3.04, although versions 2.13 and 3.02 were used at earlier iterations of this project.

The two major types of objects analyzed are halos and clusters. Halos refer to the spherical structures of dark matter that arise due to structure formation. Clusters refer to the galaxies that arise in dark matter halos and trace the halo mass distribution. Clusters can be observed through electromagnetic radiation; halos may only be observed through their gravitational effects.

Halos were found in an N-body simulation with a spherical overdensity finder. A cluster catalog created by the cluster finder *redMaPPer* is also used which mimics an observational survey of the sky for clusters of galaxies and dark matter halos. A cluster is selected when a large group of galaxies are believed to be associated, with the center chosen to be at the brightest central galaxy. As such, the mapping between the cluster catalog and the halo catalog is neither one-to-one (a cluster may be identified as a member of multiple halos) nor onto (a cluster may be a part of a "fake" halo, or a halo may have no clusters identified with it – there may be false positives or negatives).

Extracting Observables from the Mocks

In the DES Mocks, the exact location, redshift, and shear (along two directions in the sky) are known for all halos and galaxies. From these values, the critical density, two-dimensional angular and physical separations, and the tangential shear may be derived. Because the tangential shear and the convergence are both small, the tangential shear is approximately equal to the tangential reduced shear (i.e. what would be observed). True values of the shear are used, with no random dispersions caused by intrinsic shape or seeing conditions.

The critical density is calculated according to equation (2.55), where D_d corresponds to the angular distance of the lens, D_s is the angular distance of the source, and D_ds is the angular distance between the lens and source. A standard ΛCDM cosmology was used, with $\Omega_\mathrm{M} = 0.25, \Omega_\Lambda = 0.75$.

The radius R is converted to a two-dimensional angular separation by the following equation, which may be derived considering spherical trigonometry and which takes advantage of the small angle approximation $\sin\theta \approx \theta$ for small θ:

$$\theta = \sqrt{(\delta_\mathrm{d} - \delta_\mathrm{s})^2 + \cos\delta_\mathrm{d}\cos\delta_\mathrm{s}(\alpha_\mathrm{d} - \alpha_\mathrm{s})^2}, \tag{3.1}$$

where α is the Right Ascension, δ is the Declination. A physical distance is quickly obtained by multiplying θ by the transverse comoving distance to the lens, D_d^M. The polar angle between the lens and the source in the lens plane is given by the arctangent between the differences in angle:

$$\phi = \arctan\frac{\delta_\mathrm{s} - \delta_\mathrm{d}}{\alpha_\mathrm{s} - \alpha_\mathrm{d}}. \tag{3.2}$$

From Equation (3.2) and the magnitude of the given shear γ, the tangential shear is found by

$$\gamma_+ = -\Re[\gamma e^{-2\imath\phi}] \tag{3.3}$$
$$= -\gamma_1\cos(2\phi) - \gamma_2\sin(2\phi), \tag{3.4}$$

where we have used the fact that $\gamma = \gamma_1 + \imath\gamma_2$. Similarly, the cross shear is found to be

$$\gamma_\times = -\Im[\gamma e^{-2\imath\phi}] \tag{3.5}$$
$$= \gamma_1\sin(2\phi) - \gamma_2\cos(2\phi) \tag{3.6}$$

The reference angle that ϕ is compared to is the plane of the sky, with γ_1 corresponding to the right ascension, and γ_2 to the declination. In observation, however, DECam will be mounted with a position angle of 90 degrees,[1] so the following transformation is made:

$$\gamma_1 \to -\gamma_1, \qquad \gamma_2 \to -\gamma_2. \tag{3.7}$$

Additionally, the right ascension in the detector plane increases from right to left, so the next transformation is also necessary:

$$\gamma_1 \to \gamma_1, \qquad \gamma_2 \to -\gamma_2. \tag{3.8}$$

Taken together, the transformations read

$$\gamma_1 \to -\gamma_1, \qquad \gamma_2 \to \gamma_2, \tag{3.9}$$

so equations (3.4) and (3.6) are transformed into

$$\gamma_+ = \gamma_1\cos(2\phi) - \gamma_2\sin(2\phi) \tag{3.10}$$
$$\gamma_\times = -\gamma_1\sin(2\phi) - \gamma_2\cos(2\phi). \tag{3.11}$$

[1] That is, North is to the left and East is down.

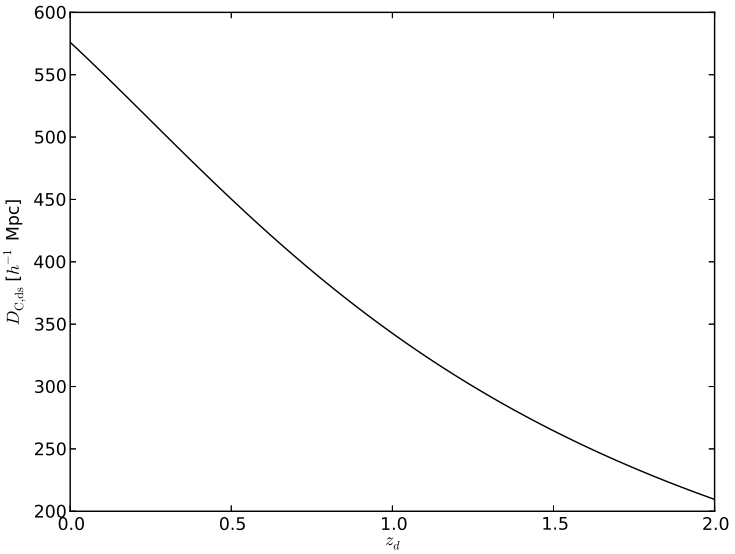

Figure 3.1: The minimum comoving distance between lens and source as a function of redshift. All selected source galaxies are well past the lens halos, which have a typical size of 1 Mpc.

Selection of Data

Lens candidates (halos and clusters) were binned according to redshift and either the mass contained within a radius that surpasses 200 times the critical density, M_{200}, or the richness, Λ. Richness is measured by the number of galaxies in a cluster. Richness bins are chosen to correspond to the N_{200} bins used in Johnston et al. (2007b). Lens candidates that were within 30 h^{-1} Mpc to the edge of the simulation were discarded. Source candidates were chosen to be galaxies within 30 h^{-1} Mpc of a lens and with a redshift $z_{\rm s} > z_{\rm d} + 0.2$, so as to prevent halo galaxies from contaminating the sample. Right ascension and declination information were transformed into radial and angular positions, and the shear information was converted into tangential and cross shear as outlined above. The chosen "effective radius" of a bin was the mean radius of the samples in the bin, which was typically within a couple percent of the logarithmic mean radius of the bin.

N_{200}	Λ	$N_{\rm Halo}$	$N_{\rm Cluster}$	$\langle\Lambda\rangle$
0–3	15.0–19.7	1745	1825	17.1
3–4	19.7–21.3	386	404	20.5
4–5	21.3–22.8	284	286	22.0
5–6	22.8–24.4	240	217	23.6
6–7	24.4–26.0	212	202	25.2
7–8	26.0–27.5	184	201	26.8
8–9	27.5–29.1	146	157	28.2
9–12	29.1–33.8	348	301	31.3
12–18	33.8–43.2	347	322	38.0
18–26	43.2–55.8	165	155	48.8
26–41	55.8–79.3	136	125	64.2
41–71	79.3–126.3	61	58	95.1
71–221	126.3–361.6	30	29	185.0

Table 3.1: The number of clusters and halos in each richness bin. Because it is possible to identify false positives and negatives, as well as misidentify the cluster richness, the number of halos and clusters may not be equal.

3.2 Analysis of "Observed" Simulation Data

Determining the Mass Distribution

Tangential shears were first multiplied by their critical densities, then binned logarithmically to 20 bins ranging from $R = 2.5 \times 10^{-2} h^{-1}$ Mpc to $R = 30 h^{-1}$ Mpc, and finally averaged. In order to reconstruct the mass as outlined in Section 2.4, an interpolated fit was made between the logarithmic values of the of the surface mass density contrasts and the radii. Negative-valued observables were "thrown out" by setting their value to 10^{-10}. Errors were calculated from the covariance matrix between surface mass density contrast $\Delta\Sigma_i$ and radius R_j, or $\mathcal{C}^{\Delta}_{ij}$. For the interpolation scheme in use, the covariances are well approximated by their first-order Taylor expansions (Johnston et al. 2007a). The covariances were then propagated via

$$\mathcal{C}^{\rho}_{ij} = \mathcal{A}_{ik}\mathcal{C}^{\Delta}_{kl}\mathcal{A}^{\rm T}_{lj}, \qquad \mathcal{A}_{ij} = \frac{\partial \rho_i}{\partial \Delta\Sigma_j}, \tag{3.12}$$

$$\mathcal{C}^{M}_{ij} = \mathcal{B}_{ik}\mathcal{C}^{\Delta}_{kl}\mathcal{B}^{\rm T}_{lj}, \qquad \mathcal{B}_{ij} = \frac{\partial M_i}{\partial \Delta\Sigma_j}, \tag{3.13}$$

where $\mathcal{A}_{ij}$ and $\mathcal{B}_{ij}$ are calculated using the finite difference method. Diagonal terms correspond to the statistical uncertainties at each point, while off diagonal terms may arise observationally from lensing shape noise, sample variance, or systematic errors in the

$0 < r_{200}$
$0.5 < z < 1$
$0 < c$
$0 < p_c < 1$
$0 < \sigma_s$

Table 3.2: The allowed ranges in parameter space for the fitted parameters. As long as the parameters are in their allowed ranges, no penalty is induced for a particular parameter choice.

point-spread function correction. Generally, if $\boldsymbol{C}^{\Delta}$ is diagonal, then $\boldsymbol{C}^{\rho}$ is also diagonal. However, because $M(r)$ is a cumulative statistic and hence correlated with its neighboring bins, $\boldsymbol{C}^{M}$ typically has large off-diagonal terms (Johnston et al. 2007a).

Determining the Mass – Halos

In the case of the halos, the method for reconstructing the mass distribution is relatively straight-forward. Halos are assumed to follow the NFW profile.[2] The parameters r_{200}, c, and z are left free for halos and fitted for an NFW surface mass density contrast. The fitting algorithm used is the Constrained Optimization BY Linear Approximation (COBYLA), which allows for constraints to be put in place on the various parameters fitted (Powell 1994). The ranges for allowed parameters is detailed in Table 3.2. From the fit the mass at 200 times the critical density, M_{200}, may quickly be determined by

$$M_{200} = \frac{800\pi}{3}\rho_{\rm crit}(z)r_{200}^3. \tag{3.14}$$

The fitted parameters r_{200}, z, and M_{200} provide quick checks versus the halos themselves in determining the effectiveness of the mass calibration.

Determining the Mass – Clusters

The case for clusters is more complicated, because some fraction of clusters are not aligned with the mass distribution. These miscenterings arise largely from the method of identification: a cluster center is chosen by the location of the brightest central galaxy (BCG). Even though the BCG is typically the largest and most massive galaxy, and hence the closest to the center of the halo, this is no guarantee that it is at the center of the halo. Additionally, the wrong galaxy may be identified as the BCG. To account for these effects, a centering term must be added, such that the observed lensing signal becomes

$$\Delta\Sigma_{\rm obs}(R) = p_c\Delta\Sigma_{\rm NFW}(R) + (1-p_c)\Delta\Sigma^s_{\rm NFW}(R), \tag{3.15}$$

[2]See Section 2.3 above.

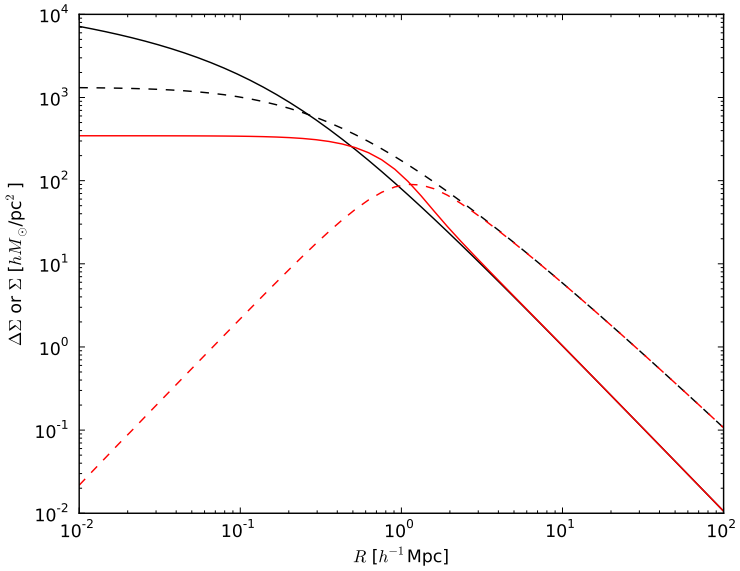

Figure 3.2: The effects of a miscentering on the measured Σ and $\Delta\Sigma$ profiles. The black solid curve shows Σ for an NFW halo with $c = 5$, $r_{200} = 1h^{-1}$ Mpc, and $z = 1.0$. The black dashed curve shows the corresponding $\Delta\Sigma$ profile. The red curves show the resulting profiles when the distribution of miscenterings is a two dimensional Gaussian with dispersion $\sigma_s = 0.5h^{-1}$ Mpc. Miscentering has the effect of making Σ^s nearly flat at small scales, such that $\Delta\Sigma^s$ drops significantly. The position at which $\Delta\Sigma^s$ peaks is around $r \approx 2.5\sigma_s$, although the effect is slightly dependent on c.

where p_c represents the fraction of properly aligned halos and $\Delta\Sigma^s_{NFW}$ is the profile that results from a miscentered NFW halo. The miscentering significantly affects the determination of the mass at two hundred times the critical radius, M_{200}: Johnston et al. (2007b) note that, without the centering term, halo mass estimates are biased low by a factor of $\sim p_c$, as M_{200} is mostly determined by the amplitude of $\Delta\Sigma$ on scales within $R \sim 1h^{-1}$ Mpc, where $\Delta\Sigma^s$ is very small.

Let us consider the centering term in more depth. If the two dimensional offset in the lens plane is R_s, then the azimuthally averaged $\Sigma(R)$ profile is given by

$$\Sigma(R|R_s) = \frac{1}{2\pi}\int_0^{2\pi} d\theta \Sigma(\sqrt{R^2 + R_s^2 + 2RR_s\cos\theta}) \tag{3.16}$$

(Yang et al. 2006). Following Johnston et al. (2007b), we assume that the probability distribution of the offsets for the miscentered clusters, $P(R_s)$, is that of a two dimensional Gaussian distribution with a mean offset of zero:

$$P(R_s) = \frac{R_s}{\sigma_s^2}\exp(-\frac{1}{2}(R_s/\sigma_s)^2). \tag{3.17}$$

The resulting mean surface mass profile for the miscentered clusters is then

$$\Sigma^s_{NFW}(R) = \int dR_s P(R_s)\Sigma_{NFW}(R|R_s), \tag{3.18}$$

and so we find that

$$\Delta\Sigma^{\mathrm{s}}_{\mathrm{NFW}}(R) = \bar{\Sigma}^{\mathrm{s}}_{\mathrm{NFW}}(< R) - \Sigma^{\mathrm{s}}_{\mathrm{NFW}}(R). \tag{3.19}$$

The parameters p_c and σ_{s} are determined empirically for sample set by examining the catalog of matched clusters and halos. For the *redMaPPer* catalog, about 40% of clusters are "well aligned" (chosen by having an angular distance with their matched halo of less than 1×10^{-1} arcminutes), while σ_{s} is generally around $0.2h^{-1}$ Mpc.[3] The empirical values are used as a prior.

[3]See Section 4.2.

Chapter 4

Results

4.1 Halos

Fitting Stacked NFW Halos

It is important to consider the impact of stacked NFW profiles on the reconstruction of the halos. There is no guarantee that the averaged NFW density profile over a range of parameters will correspond to the averaged r_{200} or c parameters; the effective parameters may not equal the average of the true parameters. In other words, it may be the case that

$$\langle \Delta\Sigma_{\rm NFW}(r; r_{200}, c, z) \rangle \neq \Delta\Sigma_{\rm NFW}(r; \langle r_{200} \rangle, \langle c \rangle, \langle z \rangle), \tag{4.1}$$

where $\langle x \rangle$ is the mean of x, although the latter may prove to be a useful prior in fitting data to the former. Similarly (and perhaps more significantly for comparative purposes), the mean and effective masses may not be equal:

$$\langle M_{200} \rangle \neq M_{200}(\langle r_{200} \rangle, \langle c \rangle, \langle z \rangle) \equiv M_{200,\rm Effective}. \tag{4.2}$$

This is to say that the very question of how one characterizes the stacked versus the individual halo may be fraught with difficulties. Fitting stacked halo NFW profiles to an effective NFW profile may yield a significantly different mass to that of the selected halos.

To explore these possible disconnects, halos were selected in the manner described in Section 3.1 and binned according to halo mass. However, instead of selecting galaxies in the mock data set about each halo, halo r_{200} and z values were used to determine c (see Duffy et al. 2008) and hence the surface density contrast of the individual halo, $\Delta\Sigma_{{\rm NFW},i}$. The simulated lens signal (assuming an NFW profile) was stacked and averaged, with the resulting profile then fitted to a single NFW profile with an effective r_{200}, c, and z. This method empirically models the effects of the probability distribution of the halos as a function of redshift and mass.

As Figure 4.1 demonstrates, the stacked NFW profile retains the essential shape of an NFW profile. Further, the mean of each of the parameters well describes the NFW profile, recovering the mean mass to within one percent. We have confirmed that it is reasonable

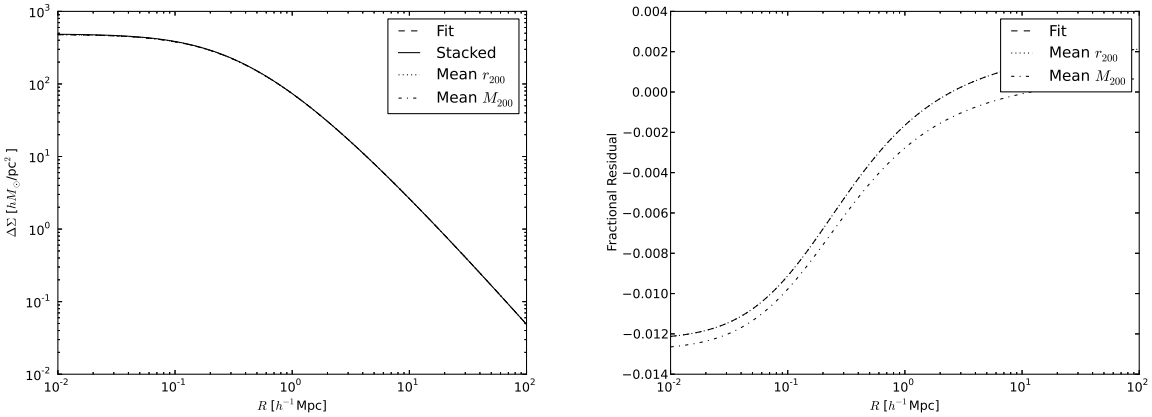

Figure 4.1: An illustrative stacked NFW profile over the mass range $M_{200} = 2.00 \times 10^{14} - 2.88 \times 10^{14}$ and $z = 0.0 - 1.0$. The best fit parameters and the mean parameters may be found in Table 4.1. Also plotted is the residual fraction, $(\Delta\Sigma_{\rm Fit}/\Delta\Sigma_{\rm Stacked} - 1)$, as a function of radius. Note that the fitted and mean r_{200} profiles are equal.

M_{200}	$r_{200,\rm mean}$	$c_{\rm mean}$	$z_{\rm mean}$	$M_{200,\rm mean}$	$r_{200,\rm fit}$	$c_{\rm fit}$	$z_{\rm fit}$	$M_{200,\rm fit}$
3.16–6.61	0.461	4.194	0.660	4.347	0.461	4.194	0.660	4.312
6.61–9.55	0.567	3.997	0.637	7.807	0.567	3.997	0.637	7.818
9.55–13.80	0.644	3.870	0.631	11.350	0.644	3.870	0.631	11.368
13.80–19.95	0.730	3.768	0.610	16.218	0.730	3.768	0.610	16.218
19.95–28.84	0.831	3.657	0.596	23.480	0.831	3.657	0.596	23.518
28.84–89.13	1.004	3.553	0.535	39.518	1.004	3.553	0.535	38.959

Table 4.1: This table examines the goodness of fits for stacked NFW halos binned by mass. r_{200} is in units h^{-1} Mpc, while M_{200} is in $10^{13}h^{-1}M_\odot$. With this binning, the fitting procedure accurately recovers the mass to within one percent.

Λ	$r_{200,\mathrm{mean}}$	c_{mean}	z_{mean}	$M_{200,\mathrm{mean}}$	$r_{200,\mathrm{fit}}$	c_{fit}	z_{fit}	$M_{200,\mathrm{fit}}$
19.7–21.3	0.464	4.06	0.744	5.40	0.464	4.06	0.744	4.82
21.3–22.8	0.472	4.06	0.734	5.68	0.472	4.06	0.734	5.03
22.8–24.4	0.502	4.04	0.700	6.50	0.502	4.04	0.700	5.83
24.4–26.0	0.506	3.97	0.744	7.10	0.506	3.97	0.744	6.25
26.0–27.5	0.524	3.98	0.710	7.41	0.524	3.98	0.710	6.69
27.5–29.1	0.510	3.93	0.763	7.24	0.510	3.93	0.763	6.54
29.1–33.8	0.528	3.90	0.763	8.21	0.528	3.90	0.763	7.25
33.8–43.2	0.554	3.83	0.774	9.41	0.554	3.83	0.774	8.46
43.2–55.8	0.601	3.74	0.777	11.91	0.601	3.74	0.777	10.88
55.8–79.3	0.651	3.64	0.793	15.51	0.651	3.64	0.793	14.02
79.3–126.3	0.734	3.51	0.805	21.33	0.734	3.51	0.805	20.39
126.3–361.6	0.765	3.41	0.860	25.68	0.765	3.41	0.860	24.54

Table 4.2: This table examines the goodness of fits for stacked NFW halos binned by richness. r_{200} is in units h^{-1} Mpc, while M_{200} is in $10^{13}h^{-1}M_{\odot}$. The fit finds the mean parameters exactly. The errors in mass come from the disconnect between the mean M_{200} of the stacked halos and the M_{200} that is calculated from the the parameters r_{200} and z. This difference is more pronounced for richness binning than for mass binning, indicating the presence of bin contamination. Notably, the recovered mass is consistently less than the mean mass of the halos by about 10 percent.

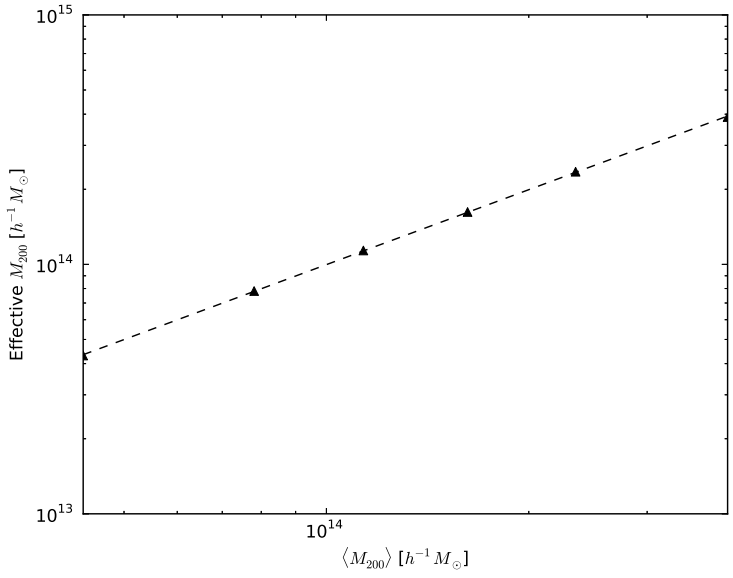

Figure 4.2: A comparison between the mean mass of the lenses in stacked mass bins and the effective mass that characterizes the resultant NFW profile. The effective mass is typically less than the mean mass by about one percent.

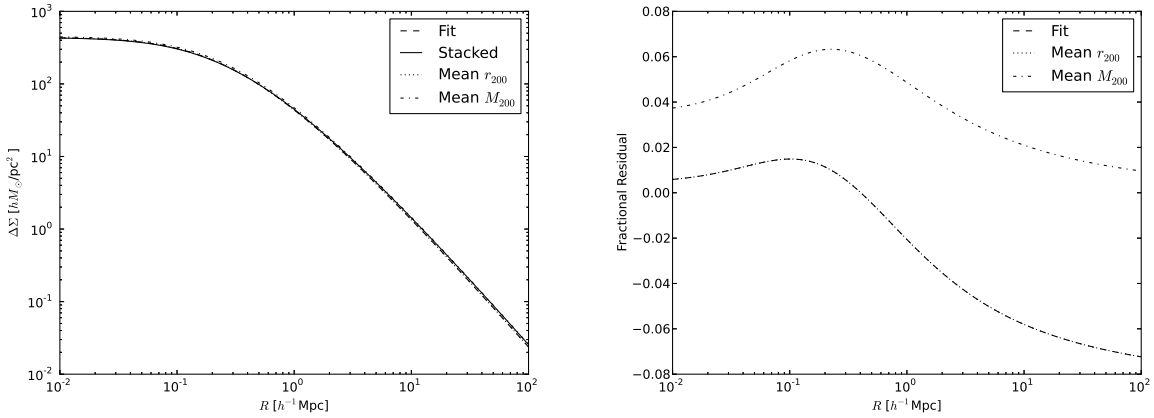

Figure 4.3: An illustrative stacked NFW profile over the richness range $\Lambda = 43.23 - 55.77$ and $z = 0.0 - 1.0$. The best fit parameters and the mean parameters were $(r_{200}, c, z) =$. Also plotted is the residual fraction, $(\Delta\Sigma_{\rm Fit}/\Delta\Sigma_{\rm Stacked} - 1)$, as a function of radius.

to assume that the effective parameterization of the stacked cluster resides somewhere near the mean of parameters. Interestingly, the mean mass is worse at characterizing the stacked halos; the effective mass recovered is *not* the mean mass. Figure 4.2 indicates that the effective mass obtained is actually slightly less than the mean mass and may be characterized by the following empirical fitting:

$$M_{200,\rm Effective} = 1.065 \times \langle M_{200} \rangle^{0.998}. \tag{4.3}$$

It is also useful to repeat this procedure for halos binned by richness instead of mass. While there is a mass-richness relation (see Johnston et al. 2007b; Tinker et al. 2012, for example), intrinsic scatter in the relationship as well as errors in the determination of either variable can propagate into errors in the determination of the the effective profile and especially the M_{200}. For example, if the scatter in richness increases with mass, then some larger halos may be misidentified as poor clusters, contaminating the richness bin and increasing the effective mass of the bin. Similarly, prolate (oblate) clusters (along the line of sight) will appear richer (poorer) than spherical clusters of similar mass, contaminating the richness bin and decreasing (increasing) the effective mass of the bin.

A combination of the intrinsic scattering caused by richness binning and the misidentification of richness due to cluster ellipticities propagate to larger errors in the fit and the mean parameters – on the order of several percent. These errors result in an average fractional error in mass estimation $M_{200,\rm obs}/M_{200,\rm mean} = 0.8791 \pm 0.0151$. This result indicates a systematic in the *redMaPPer* cluster identification procedure. Significantly larger masses will affect the mean mass to a greater degree than the surface mass density contrast. A consistent underestimation of the mass therefore indicates that the cluster catalog suffers contamination by larger mass halos.

In general, we find that reconstruction of the mean mass from stacked lenses will obtain to $-1.0 \pm 1.5\%$ of the correct halo M_{200} mass if the halos are binned by mass. However, if the halos are binned by richness, the mean mass obtained by fitting the stacked

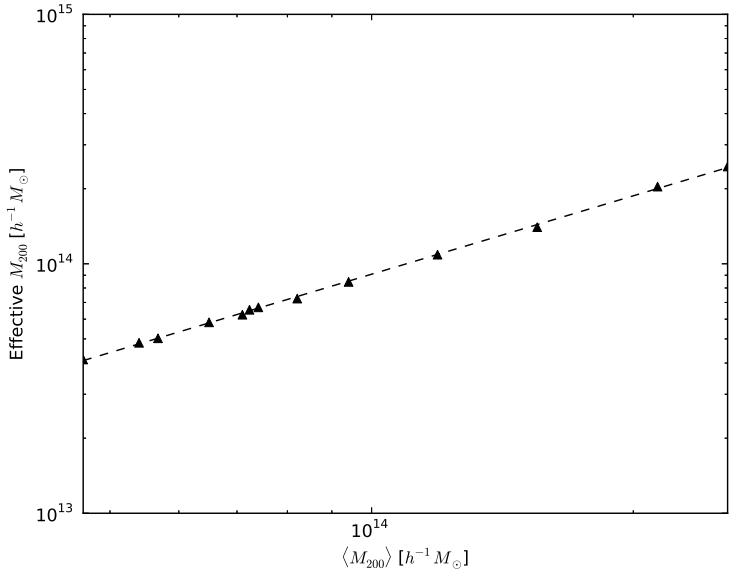

Figure 4.4: A comparison between the mean mass of the lenses in stacked richness bins and the effective mass that characterizes the resultant NFW profile. The effective mass is often 10% less than the mean mass.

lenses to an NFW profile is on average $12 \pm 1.5\%$ short, where lower richness bins are typically worse affected than higher richness bins. Figure 4.4 indicates that the effective mass obtained is consistently less than the mean mass and may be characterized by the following empirical fitting:

$$M_{200,\text{Effective}} = 0.220 \times \langle M_{200}\rangle^{1.044}. \tag{4.4}$$

This is consistent with the theory that the cluster catalog may misidentify more massive clusters as less rich, or vice versa. For instance, an oblate halo will appear less rich than a prolate halo of the same mass and ellipticity. These poorer clusters bring the mean mass up to a greater degree than they bring up the surface mass density contrast; an outlier cluster may has a mass multiple times the other members, but its surface mass density contrast will only be a fraction greater. However, this may also be due to orientation bias. As discussed earlier, the assignment of cluster richness is also biased by the orientation, such that less massive prolate clusters may be identified as richer. Finally, these results set a rough estimate on the errors in obtaining characteristic M_{200} values. We can expect that the effective mass obtained by fitting an NFW profile to stacked halos will consistently underestimate the mean mass by 10%, following Equation (4.4).

It is also interesting to briefly consider the mass-richness relation. Figure 4.5 plots the expected mass-richness relation assuming the halos are perfect NFW profiles. The empirical fitting is found to be

$$M_{200,\text{Effective}} = 4.596 \times 10^{12} M_\odot \langle \Lambda\rangle^{0.799}. \tag{4.5}$$

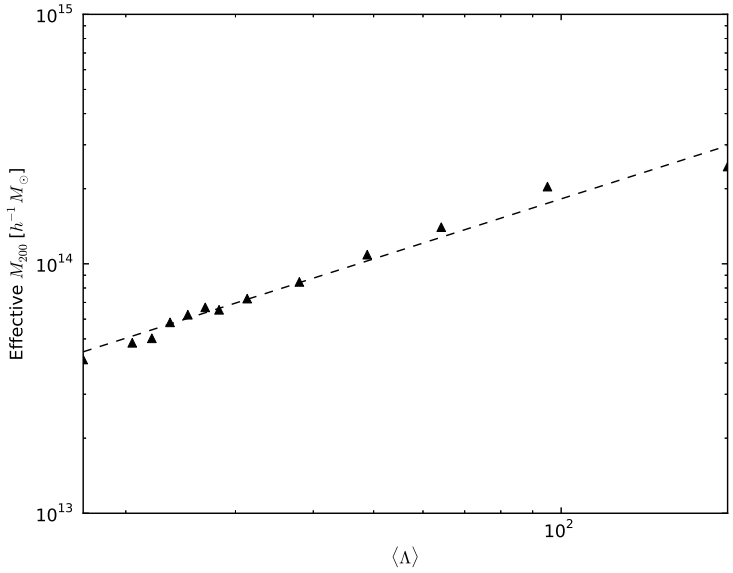

Figure 4.5: A comparison between the mean richness of the lenses in stacked richness bins and the effective mass that characterizes the resultant NFW profile. A power law well characterizes the relation.

If one were to characterize the probability distribution of the masses in a cluster bin, one could account for this underestimation by integrating over the convolution of the probability distribution with the surface mass density contrast signal, that is

$$\Delta\Sigma^{\text{Stacked}}(R) = \int \mathrm{d}M_{200} P(M_{200}) \Delta\Sigma(R|M_{200}), \tag{4.6}$$

where $\Delta\Sigma(R|M_{200})$ is just the individual halo surface mass density contrast function.

We have shown that the binning of halos by richness introduces a systematic bias in the estimation of the mass. The naive stacking of clusters binned by richness without consideration of the effects of the distribution of cluster or halo masses leads to an underestimation between the characteristic mass of the stack of clusters and the actual mean mass of order 10 percent.

Fitting "Observed" Halo Lensing

The effects of binning must be considered. Consider a bin of size $\Delta\boldsymbol{r}$ at some vector $\boldsymbol{r}$. The mean value of some function $f(\boldsymbol{r})$ is equal to the integral of the function over some number density divided by its volume, that is:

$$\langle f(\boldsymbol{r})\rangle = \frac{\int_{\boldsymbol{r}}^{\boldsymbol{r}+\Delta\boldsymbol{r}} f(\boldsymbol{r}')\sigma(\boldsymbol{r}')\mathrm{d}\boldsymbol{r}'}{\int_{\boldsymbol{r}}^{\boldsymbol{r}+\Delta\boldsymbol{r}} \sigma(\boldsymbol{r}')\mathrm{d}\boldsymbol{r}'}, \tag{4.7}$$

where $\sigma(\boldsymbol{r})$ is the number density of the region, such that the denominator in Equation (4.7) functions as a normalization. In the simplest case – the discrete addition of

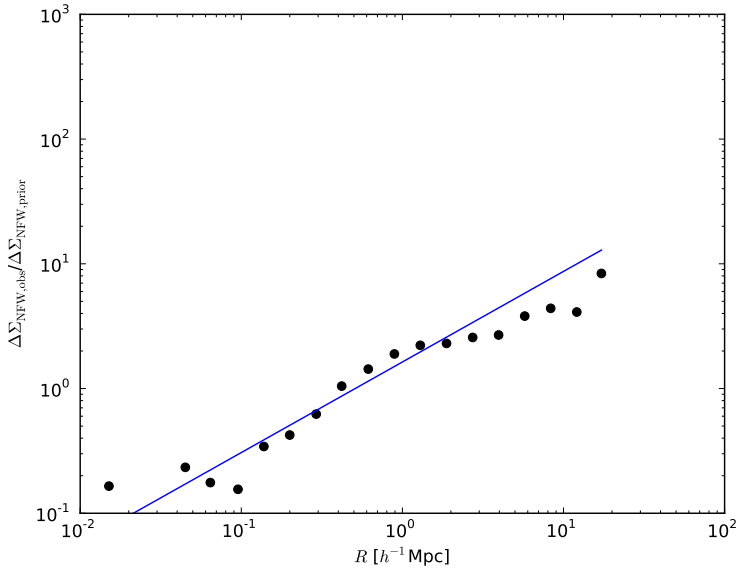

Figure 4.6: The ratio between observed NFW and theoretical NFW profiles over the richness range $\Lambda = 43.23 - 55.77$ and $z = 0.0 - 1.0$. The relationship is approximately logarithmic and fitted by $\alpha = 0.713$ and $\beta = 0.183$.

terms over a one dimensional width Δx of equal probability – Equation (4.7) may be reduced to the familiar form

$$\langle f \rangle = \frac{\frac{1}{N}\sum_i^N f_i}{\Delta x}. \tag{4.8}$$

Sadly, reality is more complicated. Here, at least, perfect simulation data means that magnification effects on number density may be neglected (see Schneider et al. 2000). The nature of N-body simulations of dark matter halos leads to a host of possible systematics. Nevertheless, it is reasonable to expect that halo lensing profiles are well-described by NFW profiles (e.g., Hoekstra et al. 2004; Mandelbaum et al. 2006; Merritt et al. 2006; Mandelbaum et al. 2008a), especially because our simulations consist of dark matter particles only; galaxies do not contribute mass. The problem then becomes a matter of determining the number density distribution and properly normalize the bins. To do this, the ratio between the observed and expected halo profiles was calculated. As Figure 4.6 demonstrates, the ratio was found to be a power law in nature, obeying

$$\log_{10} \frac{\Delta\Sigma_{\rm NFW,obs}}{\Delta\Sigma_{\rm NFW,prior}} = \alpha \log_{10} R + \beta, \tag{4.9}$$

where α and β were found empirically for each richness bin. The average values are $\alpha = 0.622 \pm 0.088$ and $\beta = 0.191 \pm 0.038$. Observed values are then divided by this value at each effective radius. This is equivalent to normalizing over the number density in the bin.

The normalization is applied to the observed $\Delta\Sigma$ profile. The resulting distribution is well-described by an NFW profile – though not the one given by the mean parameters;

Λ	α	β
19.7–21.3	0.625	0.227
21.3–22.8	0.626	0.208
22.8–24.4	0.581	0.294
24.4–26.0	0.632	0.166
26.0–27.5	0.597	0.198
27.5–29.1	0.566	0.196
29.1–33.8	0.556	0.281
33.8–43.2	0.547	0.232
43.2–55.8	0.726	0.213
55.8–79.3	0.690	0.216
79.3–126.3	0.851	0.250
126.3–361.6	1.243	0.095

Table 4.3: Fitted normalization distribution to the expected NFW halos.

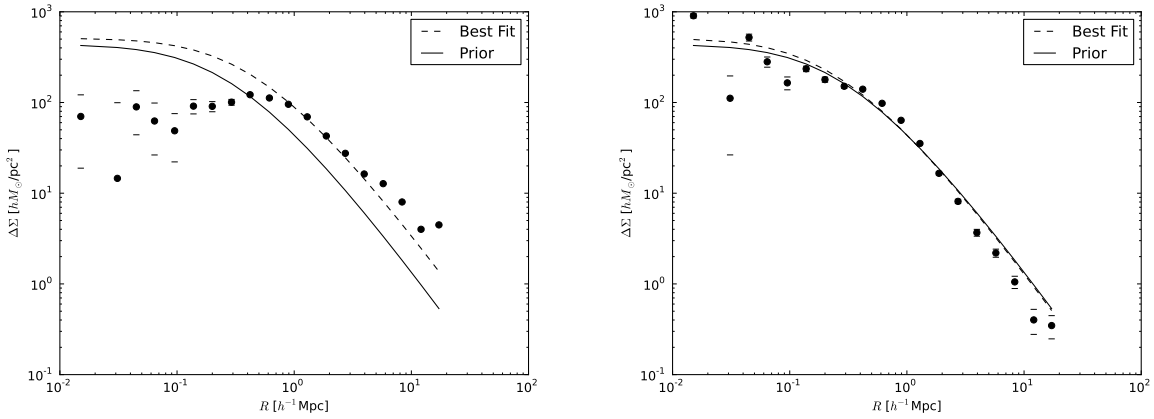

Figure 4.7: A comparison of fits for $\Delta\Sigma_{\mathrm{NFW}}$ before and after the normalization process over the richness range $\Lambda = 43.23 - 55.77$ and redshift range $z = 0.0 - 1.0$. The relationship is approximately logarithmic and fitted by $\alpha = 0.713$ and $\beta = 0.183$. Plotted are the best fit, the stacked NFW signal from the lenses, and the prior fit, which is obtained by considering the average of the parameters of the lenses. The inner four points are not included in the fit.

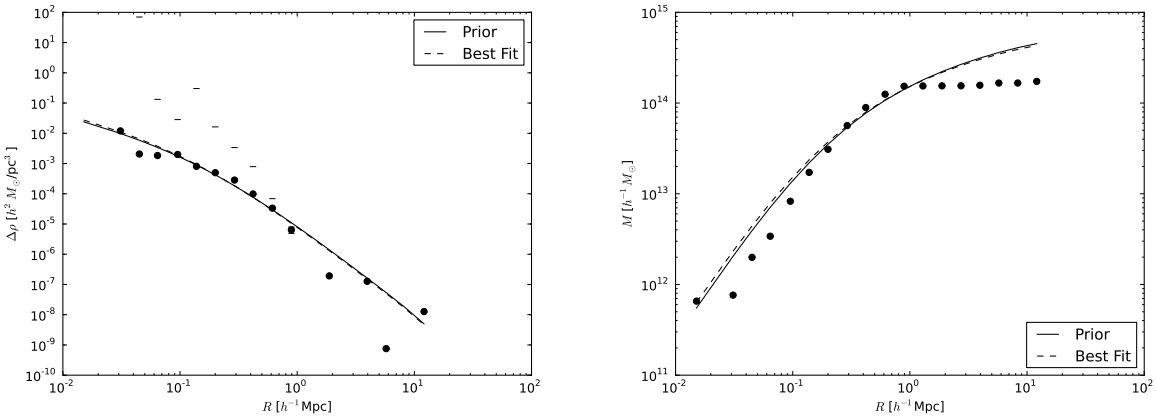

Figure 4.8: Reconstructions of the de-projected density and mass profiles over the richness range $\Lambda = 43.23 - 55.77$ and redshift range $z = 0.0 - 1.0$ versus expected distributions. The dotted lines are the expected de-projected density and mass distributions from the stacked lenses, while the dashed lines are the fitted NFW density and mass distributions. The density profile drops faster than the expected NFW profile, leading to a flattened mass distribution.

the fitting algorithm typically settled within ten percent of the average r_{200}, c, and z, but because M_{200} is extremely sensitive to small changes in any of the parameters, typical errors in the obtained M_{200} are between ten and twenty percent, even for halos.

Table 4.4 summarizes the fits for each richness bin. In general, the fitted radius to stacked halo signal is within fifteen percent of the prior radius, while the fitted redshift tends to fare much worse, often pushing the allowed parameter space. Consequently and with a few exceptions, the concentration parameter is typically found to be larger than the prior estimate. Mass estimates are generally within twenty percent of the prior mass, but with a tendency towards underestimation.

A useful check on systematics is to consider the actual number, $N(R)$, and number density, $N(R)/(2\pi R\Delta R)$, of sources in each radial bin. The number of sources should rise smoothly in a well sampled space, while the number density may reasonably be expected to be approximately constant by the principle of homogeneity. Figure 4.9 plots these relations. That the number of sources in each bin follows a power law is unsurprising, as the bin width, ΔR, is logarithmic. Further, in all richness bins, the power law is close to 2, which is to be expected for logarithmically-spaced radius bins, where ΔR is proportional to R. The number density is also approximately flat, although it does fall at greater distances.

Λ	$r_{200,\mathrm{prior}}$	c_{prior}	z_{prior}	$M_{200,\mathrm{prior}}$	$r_{200,\mathrm{obs}}$	c_{obs}	z_{obs}	$M_{200,\mathrm{NFW}}$	$M_{200,\mathrm{obs}}$
19.7–21.3	0.464	4.06	0.744	5.40	0.516	4.02	0.539	4.72	3.74
21.3–22.8	0.472	4.06	0.734	5.68	0.487	4.07	0.704	6.69	5.81
22.8–24.4	0.502	4.04	0.700	6.51	0.532	4.34	0.565	4.54	3.54
24.4–26.0	0.506	3.97	0.744	7.10	0.565	4.07	0.532	6.30	6.10
26.0–27.5	0.524	3.98	0.710	7.41	0.474	3.86	0.924	7.70	7.64
27.5–29.1	0.510	3.93	0.763	7.24	0.492	3.59	0.868	7.64	5.86
29.1–33.8	0.528	3.90	0.763	8.21	0.556	4.33	0.657	6.28	6.21
33.8–43.2	0.554	3.83	0.774	9.41	0.500	3.75	0.995	8.34	7.00
43.2–55.8	0.601	3.74	0.777	11.91	0.585	4.10	0.845	10.90	10.77
55.8–79.3	0.651	3.64	0.793	15.51	0.577	3.64	1.000	12.26	12.48
79.3–126.3	0.734	3.51	0.805	21.33	0.639	3.51	1.000	17.40	19.86
126.3–361.6	0.765	3.41	0.860	25.68	0.706	3.41	1.000	23.14	23.39

Table 4.4: This table summarizes the prior and fitted parameters for an NFW halo binned by richness. r_{200} is in h^{-1} Mpc, while M_{200} is in $10^{13}h^{-1}M_{\odot}$. $M_{200,\mathrm{NFW}}$ is the mass found from the NFW parameters, while $M_{200,\mathrm{obs}}$ is the mass at $r_{200,\mathrm{obs}}$, found by interpolating the deprojected mass profile.

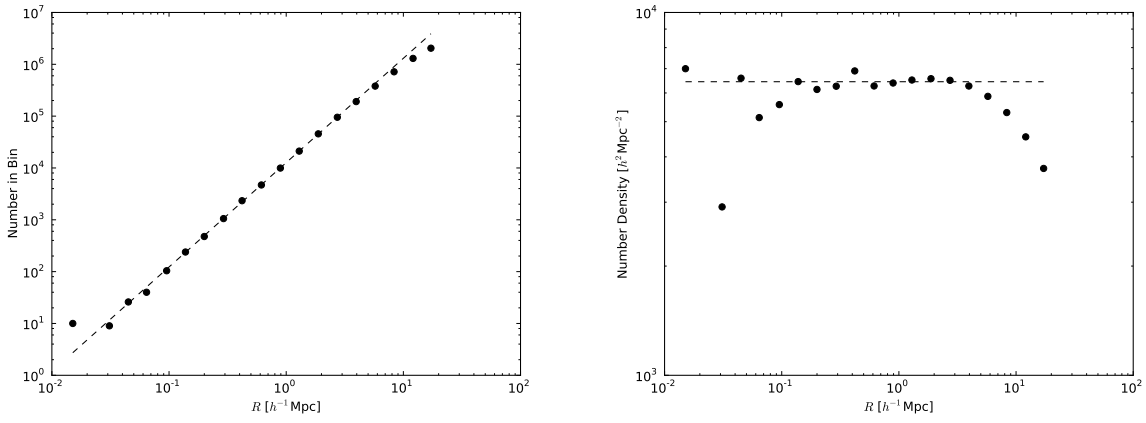

Figure 4.9: Number of sources in each radial bin and number density of sources in each bin over the richness range $\Lambda = 43.23 - 55.77$ and redshift range $z = 0.0 - 1.0$. The fitted line to the figure on the left is a power law with an exponent of 2.013 – very close to a homogeneous distribution of sources.

4.2 Clusters

Empirical Determination of p_c and σ_s

To consider the miscentering of some clusters, one must first determine how many clusters are miscentered. After this, one must then characterize the distribution of errors. Following Johnston et al. (2007b), we choose to consider the fraction of aligned halos, p_c, and the two-dimensional Gaussian centered on a mean miscentering radius of zero, $P(R_s;0,\sigma_s)$. This probability density has the advantage of being easy to compute, although we shall find that it is not the best fit to the cluster data. Matched clusters chosen by *redMaPPer* are binned by observed richness.

The probability distribution of cluster miscenterings (see Figure 4.10) has three prominent features: a steep initial logarithmic rise, a plateau, and then a softer logarithmic rise. The plateau indicates a dearth of clusters with miscenterings between $\approx 5 \times 10^{-3} - 9 \times 10^{-2}$ arcminutes. This feature is universal across all richness bins and is approximately uniform in range covered as well. The lower rise consists of clusters that are "aligned:" 10^{-3} arcminutes typically translates to a physical distance of order 10^{-4} Mpc. Clusters with miscenterings greater than the plateau may be considered the "miscentered" clusters for the purposes of this paper. In comparison with Johnston et al. (2007b), the fraction of correctly centered clusters is much lower, however, Johnston et al. (2007b) is unclear about what angular separation constitutes a "miscentering."

Miscentered clusters are chosen to be the clusters with an angular distance to their matched halo of greater than one tenth of an arcminute. The observed cumulative probability distribution is then fitted to the cumulative probability of the two dimensional Gaussian:

$$P(<R) = \int_0^R \frac{R'}{\sigma_s^2} \exp\left(-\frac{1}{2}\left(\frac{R'}{\sigma_s}\right)^2\right) \mathrm{d}R' \tag{4.10}$$

where σ_s is allowed to vary. This formalism proves to be an adequate although imperfect fit. In comparison with Johnston et al. (2007b), the dispersion of miscentered radii is much tighter – often half as much. Further, the model consistently underestimates the cumulative probability closer in and overestimates the cumulative probability further out. Indeed, the fit actually appears to be semi-logarithmic, where

$$P(<R) = \alpha \log 10R + \beta, \tag{4.11}$$

where Equation (4.11) is zero inside of some minimum radius β and zero outside of some maximum radius $10^{\frac{1-\beta}{\alpha}}$. Recalling that the probability density is related to the cumulative probability (in two dimensions with radial symmetry) by

$$P(<R) = \int_0^R P(R') 2\pi R' \mathrm{d}R', \tag{4.12}$$

one quickly finds that

$$P(R) \propto R^{-2}, \tag{4.13}$$

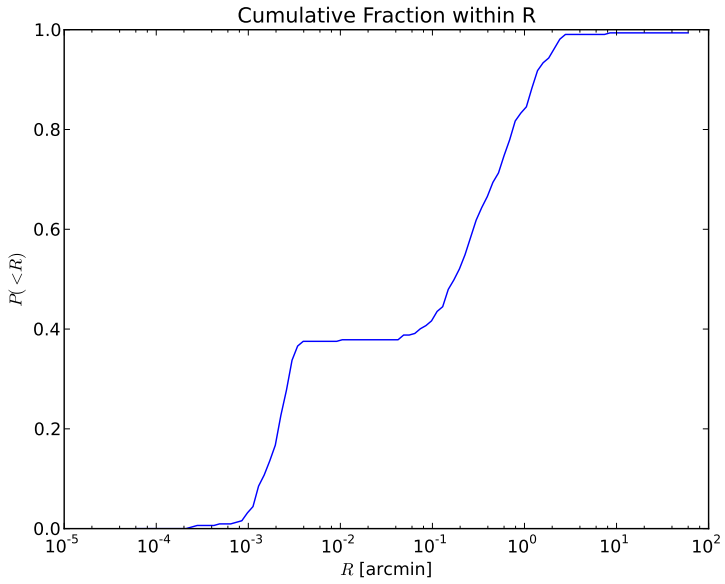

Figure 4.10: The cumulative probability distribution as a function of angular separation over the richness range $\Lambda = 43.23 - 55.77$ and redshift range $z = 0.0 - 1.0$. The plateau indicates that different systematics are at work with regards to small scale miscentering and large scale miscentering. For the purposes of this paper, a cluster is considered "aligned" if it has an angular separation of less than 0.1 arcminutes. By this definition, it is typical for around 40% of clusters to be aligned in a richness bin.

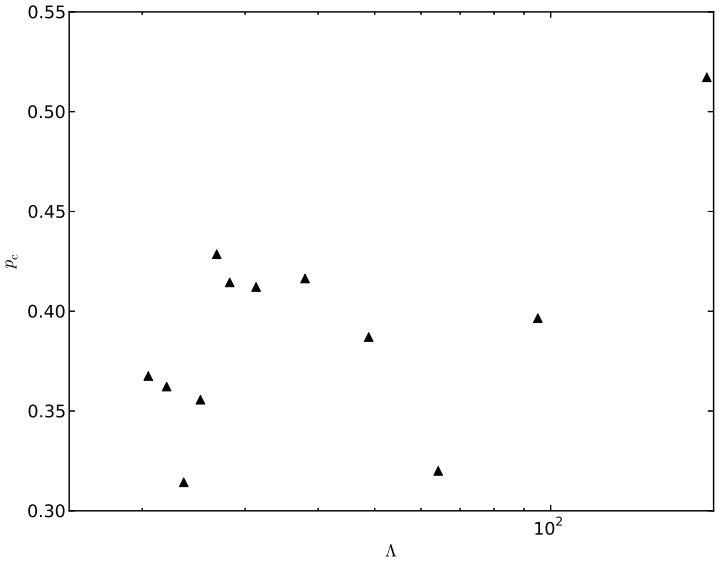

Figure 4.11: The probability that a cluster is correctly centered as a function of cluster richness, Λ, in the mock catalog. There is no obvious trend with richness.

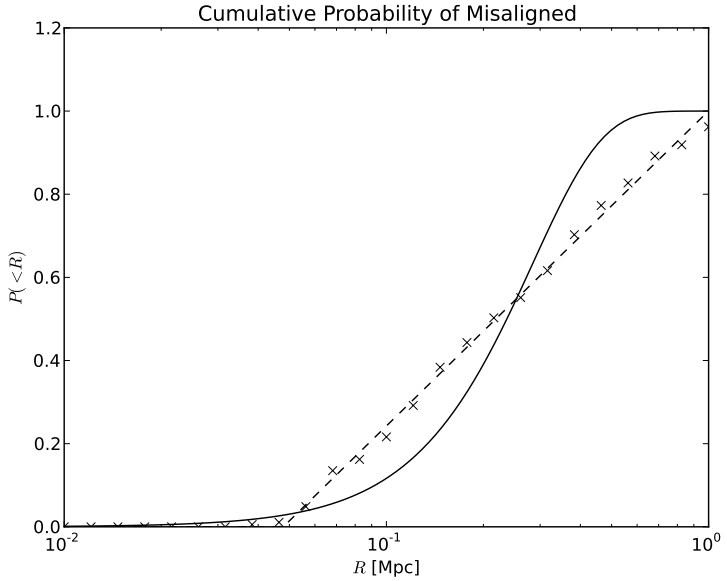

Figure 4.12: The cumulative probability distribution of the miscentered clusters as a function of physical (angular diameter) distance over the richness range $\Lambda = 43.23 - 55.77$ and redshift range $z = 0.0 - 1.0$. The solid line plots the two dimensional gaussian, with a mean miscentering of 0 h^{-1} Mpc. The dashed line plots an alternative semi-logarithmic fit to the cumulative distribution, which is equivalent to a probability density proportional to r^{-2}.

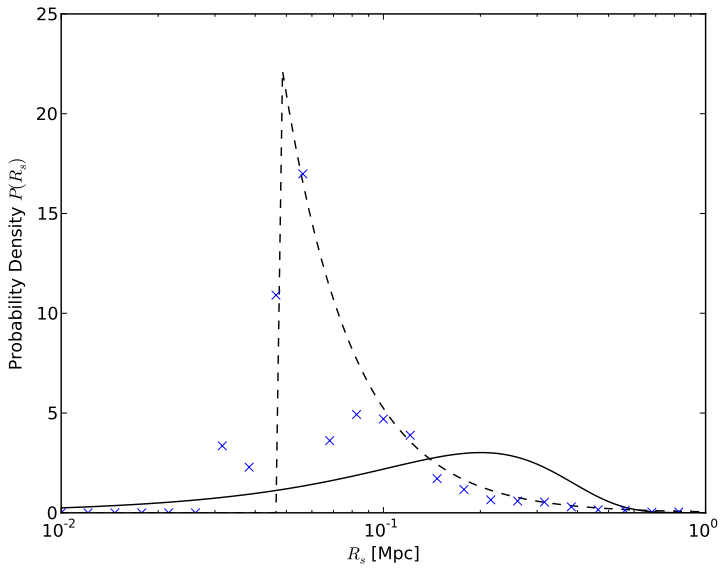

Figure 4.13: The probability density as a function of physical (angular diameter) distance over the richness range $\Lambda = 43.23 - 55.77$ and redshift range $z = 0.0 - 1.0$. The blue line plots the two dimensional gaussian, with a mean miscentering of 0 h^{-1} Mpc. The green line plots an alternative r^{-2} fit to the miscentered clusters. Because the alternative fit has hard boundaries and on one side has an extremely steep gradient at the boundary, it is normalizable but difficult to use in computations.

Λ	r_{200}	c	z	M_{200}	p_c	σ_s
19.7–21.3	0.464	4.06	0.744	5.40	0.368	0.230
21.3–22.8	0.472	4.06	0.734	5.68	0.362	0.215
22.8–24.4	0.502	4.04	0.700	6.51	0.314	0.237
24.4–26.0	0.506	3.97	0.744	7.10	0.356	0.247
26.0–27.5	0.524	3.98	0.710	7.41	0.429	0.219
27.5–29.1	0.510	3.93	0.763	7.24	0.414	0.235
29.1–33.8	0.528	3.90	0.763	8.21	0.412	0.213
33.8–43.2	0.554	3.83	0.774	9.41	0.416	0.201
43.2–55.8	0.601	3.74	0.777	11.91	0.387	0.191
55.8–79.3	0.651	3.64	0.793	15.51	0.320	0.230
79.3–126.3	0.734	3.51	0.805	21.33	0.397	0.125
126.3–361.6	0.765	3.41	0.860	25.68	0.517	0.167

Table 4.5: This table summarizes the *prior* parameters for clusters binned by richness. Their allowed ranges were detailed in Table 3.2. The effective radius, r_{200}, is in units h^{-1} Mpc, while M_{200} is in $h^{-1}10^{13}M_{\odot}$.

where the probability density is also zero in the same bounds as Equation (4.11). This result is not surprising. Centers of clusters are chosen by their brightest galaxies, which are assumed in simulations to trace the dark matter halo distribution – in this case, the NFW profile. In the interior regions, the NFW profile is proportional to R^{-1}, while in the tail it is proportional to R^{-3}. If the galaxies trace the dark matter, then miscenterings will also trace the distribution – so in reality all we have found is that an R^{-2} proportionality is closer to an NFW profile than a two dimensional Gaussian. The R^{-2} proportionality arises as an averaging of the NFW distribution. Unfortunately Equation (4.13) (and its NFW counterpart) features steep and large gradients that make it computationally expensive to use. This paper continues to use the two dimensional Gaussian fit, but leaves this evidence here as the basis for further work.

Fitting "Observed" Cluster Lensing

Because the lensing of clusters should be closely related to the lensing of halos, it is worth our time to at least briefly contrast the two data sets. Normalization was done on a bin-by-bin basis to both data sets from the empirical normalization formula derived above. Figure 4.14 mirrors many of the properties of Figure 3.2. In the interior, the cluster signal is flatter, reflecting the loss of signal from the miscentered clusters. Further out, the cluster signal closely mirrors the halo signal, again as expected. The wide variability in signal from the first four points (caused by low number statistics – see Figure 4.17) justify their exclusion when fitting Equation (3.15).

Likely because of the inadequacies of the two dimensional Gaussian model, the fitting

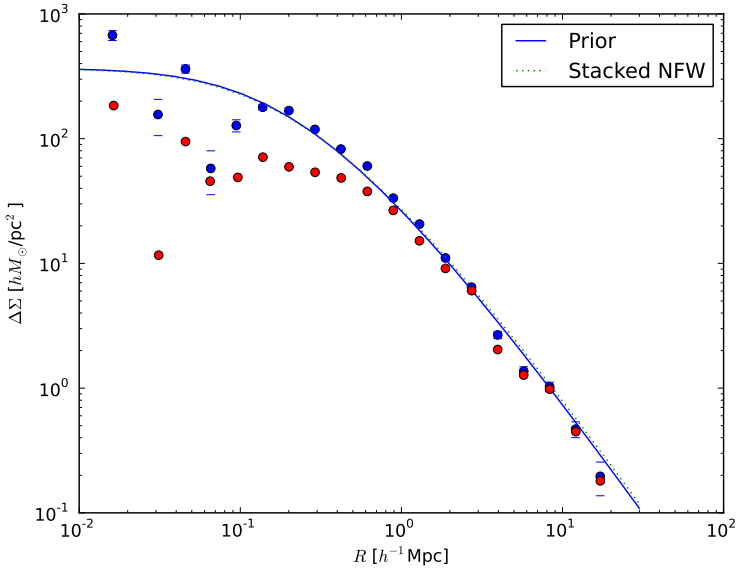

Figure 4.14: The $\Delta\Sigma$ profiles for both the halo (blue) and cluster (red) over the richness range $\Lambda = 43.23 - 55.77$ and redshift range $z = 0.0 - 1.0$. There is a clear leveling off of the cluster profile from miscenterings well before resolution errors render observation into speculation.

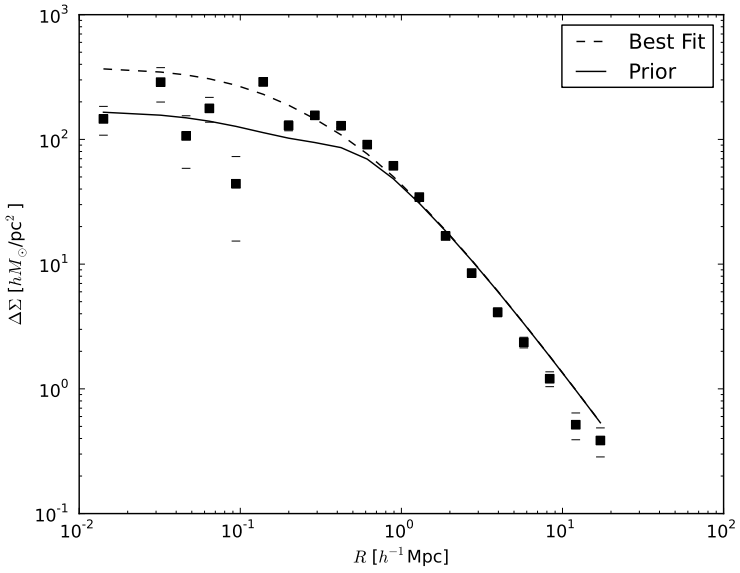

Figure 4.15: The observed $\Delta\Sigma$ profile over the richness range $\Lambda = 24.4 - 26.0$ and redshift range $z = 0.0 - 1.0$. The prior overestimates the mass in comparison with the best fit.

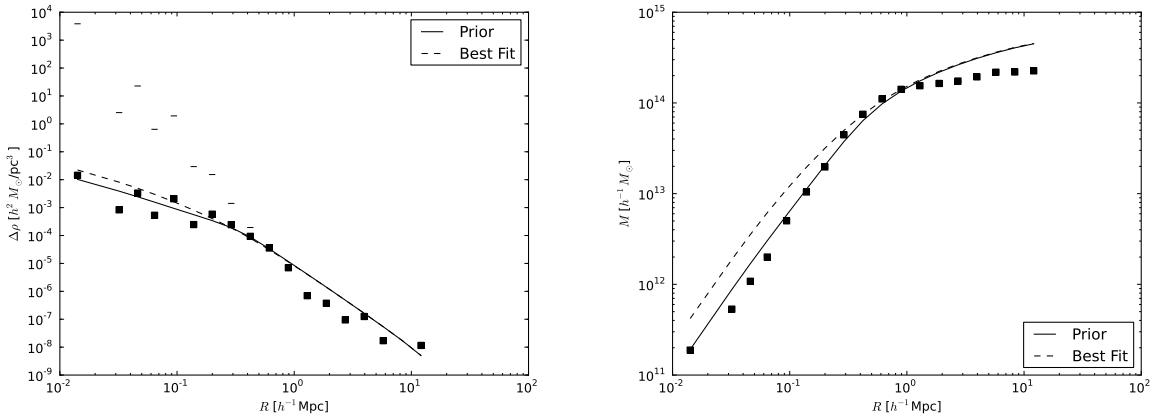

Figure 4.16: Reconstructions of the de-projected density and mass profiles over the richness range $\Lambda = 24.4 - 26.0$ and redshift range $z = 0.0 - 1.0$.

Λ	r_{200}	c	z	p_c	σ_s	$M_{200,\mathrm{NFW}}$	$M_{200,\mathrm{obs}}$
19.7–21.3	0.461	4.06	0.743	0.507	0.232	4.72	3.74
21.3–22.8	0.517	4.06	0.744	0.487	0.217	6.69	5.81
22.8–24.4	0.464	4.04	0.691	0.406	0.246	4.54	3.54
24.4–26.0	0.509	3.97	0.738	0.828	0.473	6.30	6.10
26.0–27.5	0.592	3.97	0.500	0.938	0.410	7.70	7.64
27.5–29.1	0.536	3.93	0.769	0.359	0.251	7.64	5.86
29.1–33.8	0.529	3.90	0.627	1.000	0.452	6.28	6.21
33.8–43.2	0.551	3.83	0.773	0.373	0.203	8.34	7.00
43.2–55.8	0.596	3.74	0.801	0.847	0.203	10.90	10.77
55.8–79.3	0.623	3.64	0.788	0.596	0.243	12.26	12.48
79.3–126.3	0.695	3.51	0.808	1.000	0.104	17.40	19.86
126.3–361.6	0.751	3.41	0.858	1.000	0.161	23.14	23.39

Table 4.6: This table summarizes the fitted parameters for clusters binned by richness. r_{200} is in units h^{-1} Mpc, while M_{200} is in $10^{13}h^{-1}M_\odot$. $M_{200,\mathrm{NFW}}$ is the mass of the halo found from the NFW parameters, while $M_{200,\mathrm{obs}}$ is the mass at $r_{200,\mathrm{obs}}$, found by interpolating the deprojected profile.

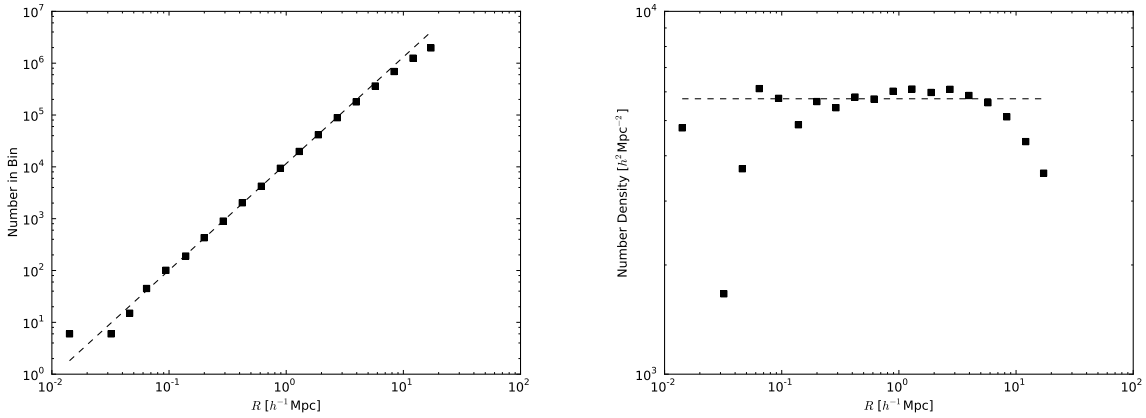

Figure 4.17: Number of sources in each radial bin and number density of sources in each bin over the richness range $\Lambda = 24.4 - 26.0$ and redshift range $z = 0.0 - 1.0$. The fitted line to the figure on the left is a power law with an exponent again close to an isotropic distribution.

algorithm pushes the fraction of properly aligned halos, p_c, much higher than is observed from the matched cluster-halo catalog. Occasionally, the algorithm even tries to mitigate the centering contribution entirely. Excepting a couple outlying parameters, fitted parameters are within 15% of their priors; the priors make reasonable "first guesses." Excepting the upper three richness bins, interpolated masses are lower than their corresponding NFW fit mass by as much as 25% in the worst case. This discrepancy may be explained by considering Figure 4.16 and Figure 4.15 in the contexts of Equation (2.69) and Equation (2.78): the deprojection of the surface mass density contrast favors contributions from interior points, which have large $\Delta\Sigma$ values, so larger discrepancies there will more significantly affect the recovered deprojected mass and mass density profiles. Additionally, false positives in the cluster catalog may dilute the signal and produce larger discrepancies.

4.3 Ellipticities

Recalling Equation (2.94), one can attempt to discern the ellipticity of a richness bin. Here we consider the ratio between the cluster and halo M_{200} masses. While Equation (2.94) operated under the assumption that all parameters save q were equal, here we allow for the two masses to have different parameters, fitting[1]

$$\frac{M_{200,\mathrm{cluster}}(r''_{200}, c'', z'', q'')}{M_{200,\mathrm{halo}}(r'_{200}, c', z', q' = 1)} = q^{-2}\left[\ln(1+cq) - \frac{cq}{1+cq}\right] / \left[\ln(1+c) - \frac{c}{1+c}\right], \quad (4.14)$$

where c is the average of the cluster and halo concentrations, while q is fitted. Figure 4.18 demonstrates the results of these calculations. The discrepancy between the NFW and

[1] See Equation (2.94).

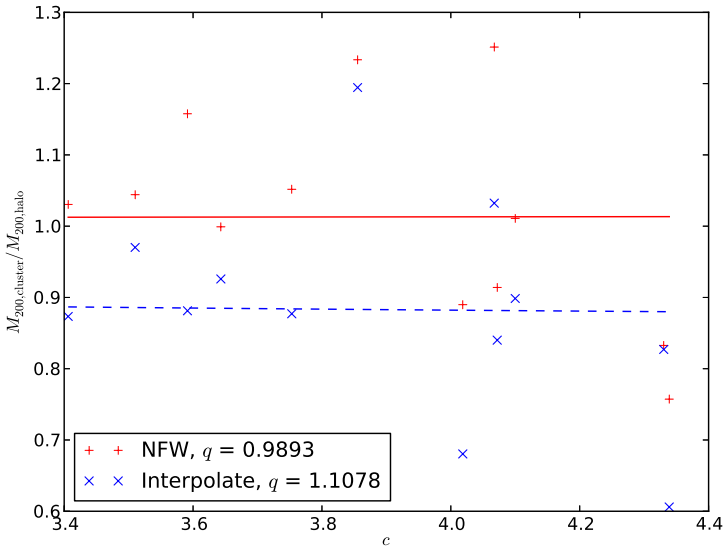

Figure 4.18: Fitted ellipticities q as a function of halo concentration for both mass estimators.

deprojected profiles is not surprising, for the NFW profile has accounted for miscenterings while the spherical inversion method has accounted for neither the miscentering of the halos nor the ellipticity. In other words, what is dominating the differences between the interpolated and fitted masses is the miscentering; what Figure 4.18 is indicating is that cluster miscentering can significantly impact the measured ellipticity. Comparing the much-higher fitted fraction of miscentered clusters with the values derived from the matched catalog, ellipticities may also be impacting the fitted miscenterings. This is to say that when fitting an assumed-spherical but miscentered cluster, the ellipticity can manifest itself as a contribution to the miscentering, and vice versa.

Chapter 5

Discussion, Further Work, and Conclusions

5.1 Discussion

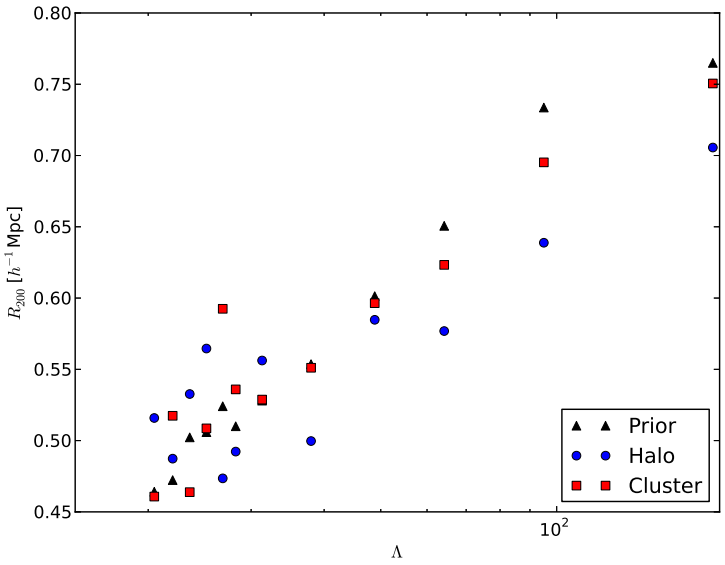

Figure 5.1: Observed and prior r_{200} radii for clusters and halos. These are the fitted r_{200} for the effective NFW profile describing the stacked halos and clusters. While there is a large amount of scatter, the expected trend – that richer clusters have larger radii – is observed.

Figure 5.1 through Figure 5.7 summarize the results of the simulated lensing observations. As Figure 5.1 demonstrates, the r_{200} radii for clusters and halos both increase with richness; as richness increases, mass increases, and so the radius increases. At lower richness bins, there is no preference for whether the halo or cluster has a larger radius, but as

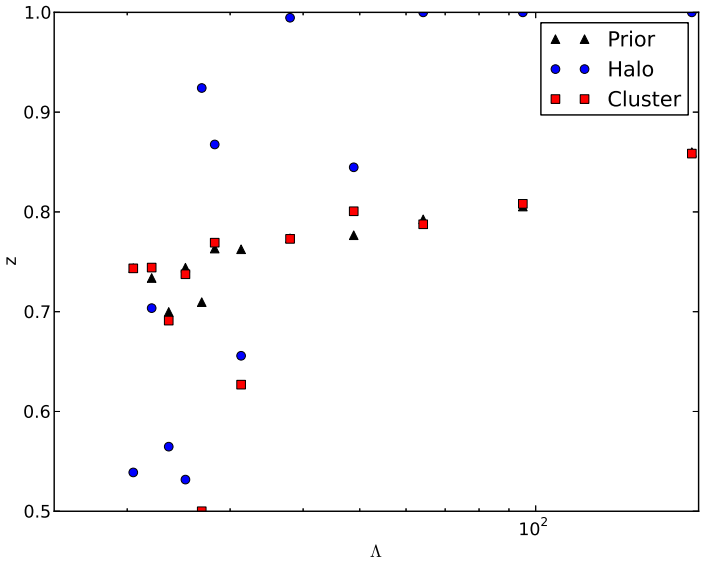

Figure 5.2: Observed and prior effective redshifts for clusters and halos. These are the fitted redshifts for the effective NFW profile describing the stacked halos and clusters. The halo redshifts push strongly against the allowed parameter space, while the cluster redshifts typically reside near the prior redshifts. There is a weak trend toward increasing effective redshift with richness.

the richness increases, clusters consistently fit larger radii than halos – although still less than the prior. This is because the high richness halos consistently fit redshifts near the maximum allowed redshift ranges, as Figure 5.2 demonstrates. Indeed, Figure 5.2 indicates that the halo redshift fits are generally quite poor. There is a weak trend in redshift with richness: as richness increases, mean redshift increases. This is to say that, in these simulations, clusters with greater numbers of galaxies (which is roughly equivalent to more massive clusters) are observed further back in time, because the volume increases dramatically with redshift.

Figure 5.3, Figure 5.4, and Figure 5.5 examine the distribution of masses obtained. Figure 5.3 examines the effective masses obtained as a function of richness. As expected, an increase in richness corresponds to an increase in effective mass. Figure 5.4 plots the fractional change from the prior empirical distribution (the dashed line on Figure 5.3). The mean masses, as discussed earlier, are consistently 10% larger. Spherical inversion-fitted halo masses tend to be higher than NFW halo masses derived from the fitted profiles, while spherical inversion-fitted cluster masses tend to be lower than NFW cluster masses. However, there is considerable spread about the empirical relation: the halo fits have an average absolute percent error about the empirical relation of 7% for the NFW and interpolated methods, while the cluster fits have an average absolute percent error of 12% and 13%, respectively. Figure 5.5 compares the effective masses obtained with the mean mass of each richness bin. Average absolute percent errors are a little worse than in Figure 5.3

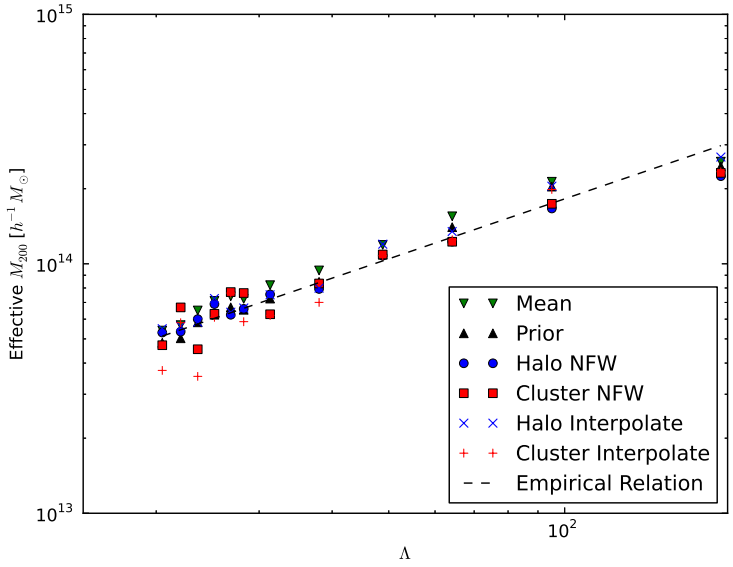

Figure 5.3: Scatter plot of found, prior, and mean masses as a function of richness. The empirical relation from Equation (4.4) is also plotted. As observed earlier, mean masses are consistently higher than the empirical relation. The other methods, however, are scattered about the empirical relation with a mean scatter of $4.571 \times 10^{13} M_\odot$.

(6%,11%, 14%, and 17% respectively).

Figure 5.6 and Figure 5.7 compare the two methods for obtaining cluster and halo masses: spherical inversion of the deprojected mass at the fitted r_{200} radius, and the mass arising from an NFW profile with the fitted parameters. Figure 5.6 compares obtained cluster and halo masses and examines whether cluster masses are consistently underestimated (arising, e.g., from ellipticities), while Figure 5.7 looks at the ratio of cluster and halo masses as a function of richness (e.g. looking at whether the ellipticity is richness dependent). The NFW fitting method does not find a net under- or overestimation of the cluster masses in comparison with the halo masses, although it does find a much wider variance at lower richness. In contrast, while the spherical inversion method also finds much wider variances in obtained masses at lower richnesses, it also consistently finds (with the exception of two bins) that measured cluster masses are lower than their equivalent halo masses.[1]

[1]See Section 4.3.

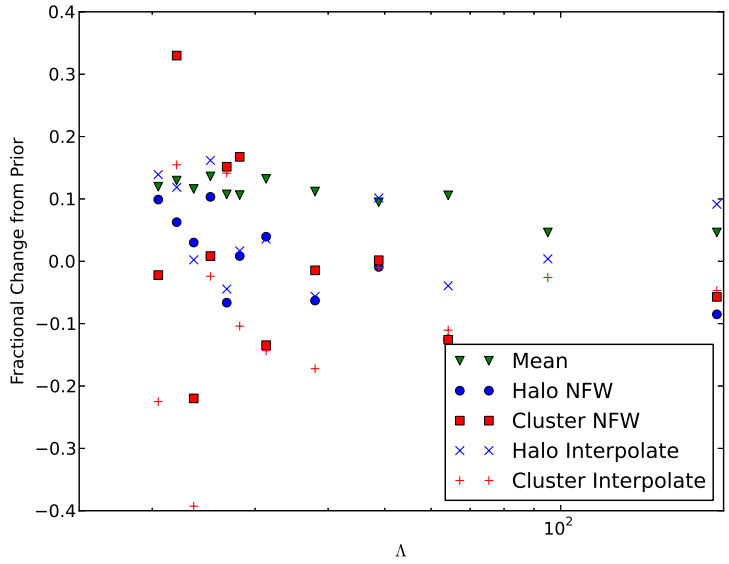

Figure 5.4: The fractional change from the prior mass for various mass determination methods. The mean mass is consistently about ten percent higher than the prior mass. Interpolated halo masses tend to be higher than NFW halo masses, while interpolated cluster masses tend to be lower than NFW cluster masses.

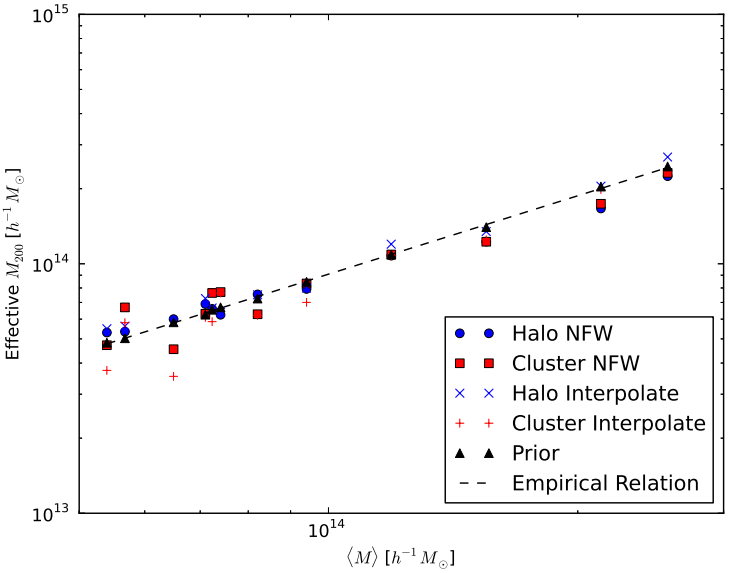

Figure 5.5: Scatter plot of found, prior, and mean masses as a function of mean mass. The empirical relation from Equation (4.3) is also plotted. While there is scatter about the empirical relation, cluster fits consistently do worse than halo fits.

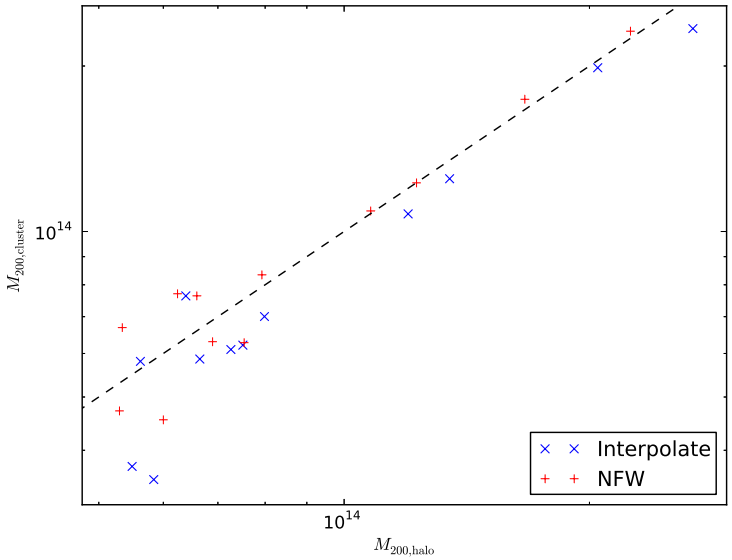

Figure 5.6: A comparison of obtained cluster and halo M_{200} masses from the two different mass models (spherical inversion and NFW). Also plotted is the dashed line $M_{200,\mathrm{cluster}} = M_{200,\mathrm{halo}}$. Interpolated mass fits consistently find cluster masses are lower than halo masses.

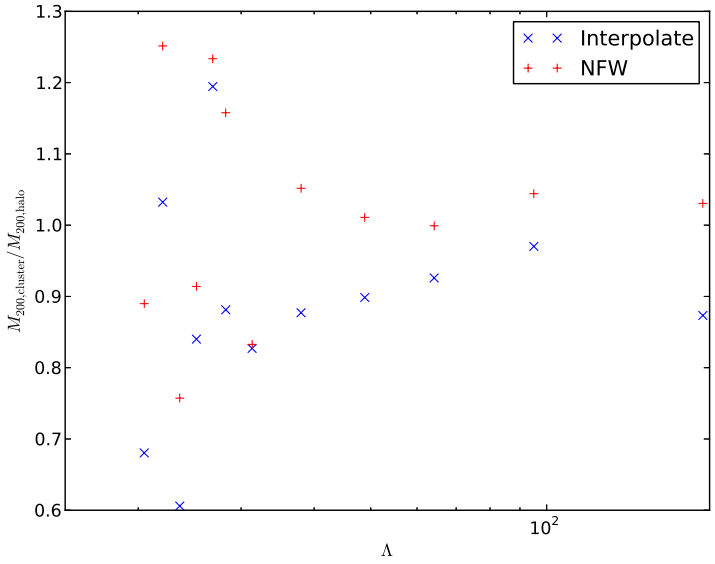

Figure 5.7: The ratio of observed cluster and halo masses. The masses are found either by calculating M_{200} from the fitted NFW parameters or from the deprojected mass profile. The interpolated mass ratios are consistently below the NFW mass profiles.

5.2 Further Work

There still remain several avenues toward further work on the topics of mass reconstruction via weak gravitational lensing and the characterization of ellipticity in selected clusters. The analysis of the clusters and halos currently does not account for effects from neighboring mass concentrations – the so-called "two-halo term" (Seljak 2000; Mandelbaum et al. 2005; Johnston et al. 2007b):

$$\rho_{2h}(r) = b(M_{200},z)\Omega_{\rm M}\rho_{\rm c,0}(1+z)^3\xi_l(r,z), \tag{5.1}$$

where $\rho_{\rm c,0}$ is the critical density at the present epoch, ξ_l is the auto-correlation function of the mass in linear perturbation theory, and b is the linear bias parameter for dark matter halos, which is predicted to depend on halo mass and redshift (Seljak and Warren 2004). This term has the most significant effect at larger radii.

Several probability distributions appear to have been mischaracterized or neglected: the two dimensional Gaussian is not a good fit for the cluster miscentering probability – it appears that an NFW-shaped probability distribution would do better. In stacking halos by richness bins, the convolution of the probability of the halo mass distribution must also be accounted for, and will likely remove the effects of the "empirical correction" derived earlier. This can be obtained, similar to the cluster miscentering probability distribution, by examining the matched cluster-halo catalog.

Because simulations always have an eye toward actual observation – especially in a project that is attempting to characterize systematic biases – observational effects on the shear fields (e.g. from galaxy ellipticities) should also be included. This is equivalent to using the ellipticity, ϵ, instead of the shear, γ, in the "observations" and then reducing the ellipticity data to shear data. Such a change also necessitates the accounting for non-linear effects, as ϵ traces the reduced shear g, not the shear γ (Mandelbaum et al. 2006).

Finally, given the number of parameters involved (which is certain to grow if the above concerns are considered), typical equation fitters like least squares and COBYLA become inefficient. As the results have demonstrated, it is possible for such fitters to become "stuck" on the edges of allowed parameter space, which may appear as local and not global minima. A better way of managing these numerous parameters is to create a likelihood function with a Markov Chain Monte Carlo (MCMC). MCMC methods generate sequences in parameter space that represent a fair sampling from the full probability distribution. MCMC methods are well-suited for using priors and non-Gaussian errors (Johnston et al. 2007b).

The precise measurement of gravitational lensing from our sun helped grant general relativity legitimacy. Although Einstein had little use for it afterwards, the field of gravitational lensing has blossomed into a uniquely powerful method for examining astrophysical and cosmological phenomena. Today, it will likely be the precise measurements of gravitationally-lensed objects that will characterize, if not answer, the questions of dark energy and dark matter. However, gravitational lensing – and especially weak gravitational lensing – is fraught with numerous difficulties, particularly in the reduction of large amounts of data. This thesis looked at the methods of reducing shear fields into

useful distributions and numbers such as the density distribution, ρ, and the mass at two hundred times the critical radius, M_{200}. Even with simplified methods (in contrast with the sophisticated methods of, e.g., in Johnston et al. (2007b)), halo masses are obtained within fifteen percent, while cluster masses are recovered to within twenty-five percent – respectable, considering that shear and deprojected mass signals both span four orders of magnitude. Significant insight into the natures of spherical deprojection of elliptical profiles and of richness binning have been made. Further work is necessary to increase the precision of these measurements and possibly identify systematic ellipticities.

5.3 Conclusions

This thesis investigated the reconstruction of three dimensional mass profiles from two dimensional weak gravitational lensing shear fields, with an eye toward quantifying the ellipticity of selected clusters. This section summarizes the salient points arising both from theory and simulation. The order of conclusions follows the order of the paper.

- The derivative-less deprojection method is consistently a couple percent below method outlined in Johnston et al. (2007a). This difference is due to the error in the integration by parts, that is, Equation (2.70). The derivative-less deprojection method is smoother than method outlined in Johnston et al. (2007a). However, because both methods consistently underestimate the deprojected three dimensional density profile, a "lucky bounce" in the derivative (from numerical artifacts) will compensate for this underestimation.

- Elliptical profiles naively deprojected assuming spherical symmetry will appear as $\rho_{\text{Elliptical}}(r; r_s, q) = q\rho_{\text{Spherical}}(r; r_s/q)$ for some ellipticity q and some scale factor r_s.

- NFW profiles binned by mass and stacked together yield a mean profile well described by the stacked parameters. The fitted M_{200} recovers the mean M_{200} of the stacked profiles.

- When binning by richness is used, the mean profile is well described by the mean parameters, but the effective mass (from those parameters) becomes disconnected from the mean mass of the stacked profiles by around 10%. The probability distribution of the masses as a function of richness must be considered.

- The two-dimensional Gaussian probability distribution does not well-characterize *redMaPPer*'s miscenterings.

- Measurements of shear in simulations, even with these simplified models, can recover halo masses to within 15%.

- Cluster mass recovery is worse – to within 25% instead.

- Spherical inversion mass fits consistently find that cluster masses are less than halo masses because the spherical deprojection does not account for cluster miscenterings. This effect is not observed with NFW mass fits, which does account for miscenterings.

- At these errors and uncertainties, it is not possible to differentiate the elliptical effects from the noise.

Chapter 6

Acknowledgements, Appendix, and Bibliography

Look up at the sky.
Ask yourselves: is it yes or no?
Has the sheep eaten the flower?
And you will see how everything changes . . . .

—Antoine de Saint-Exupéry[1]

An imagination and a willingness to believe (if only for a second) in the absurd seem to me innate traits of an astrophysicist. I would like to thank Doctor Jörg Dietrich and Professor Timothy McKay for their guidance and patience, as well as for the opportunity to do research with them. They have fostered an astrophysical imagination in me. I would also like to thank Yuan-Yuan Zhang and Jeeseon Song for their insights during our weekly lab meetings and for their help with the halo and cluster catalogs. I would finally like to thank my friends and family for their empathy and tireless support.

[1]Translation by Sarah Ardizzone.

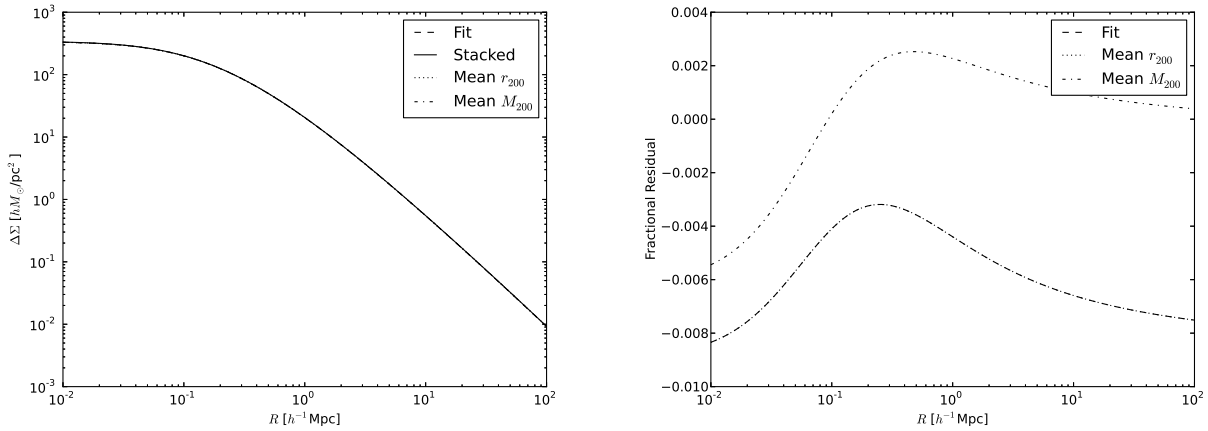

(a) $M_{200} : 3.16 - 6.61\ 10^{13} h^{-1} M_\odot$

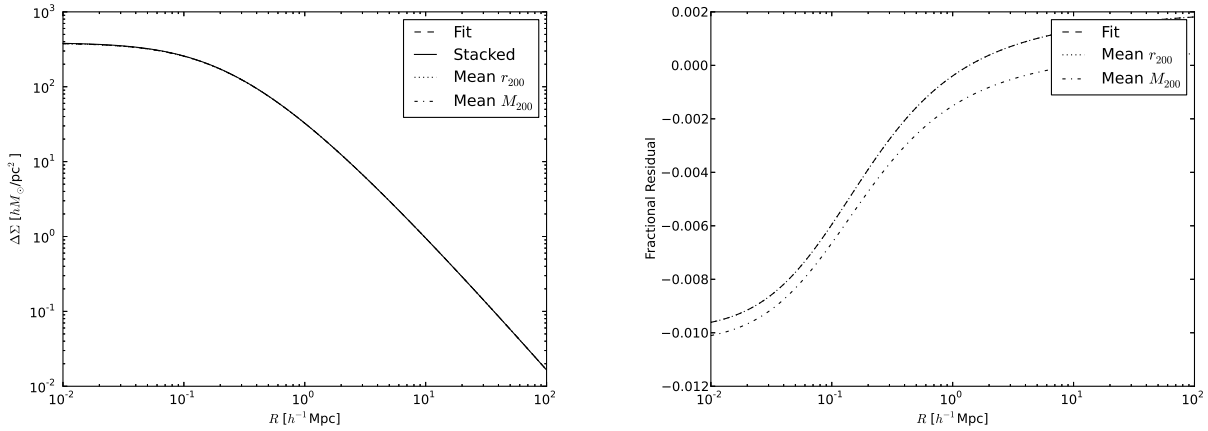

(b) $M_{200} : 6.61 - 9.55\ 10^{13} h^{-1} M_\odot$

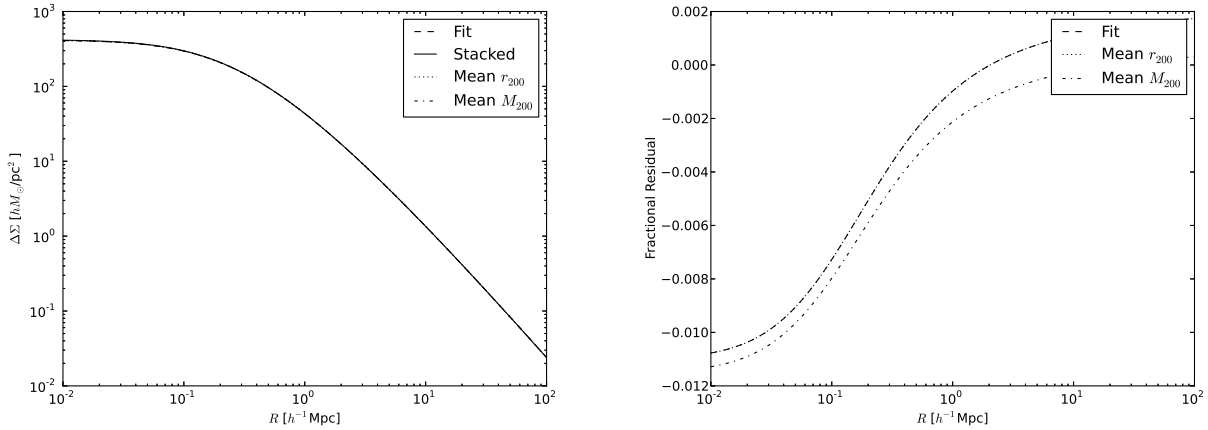

(c) $M_{200} : 9.55 - 13.80\ 10^{13} h^{-1} M_\odot$

Figure 6.1: NFW profiles binned by mass over $z = 0.0 - 1.0$ as well as their residual fraction.

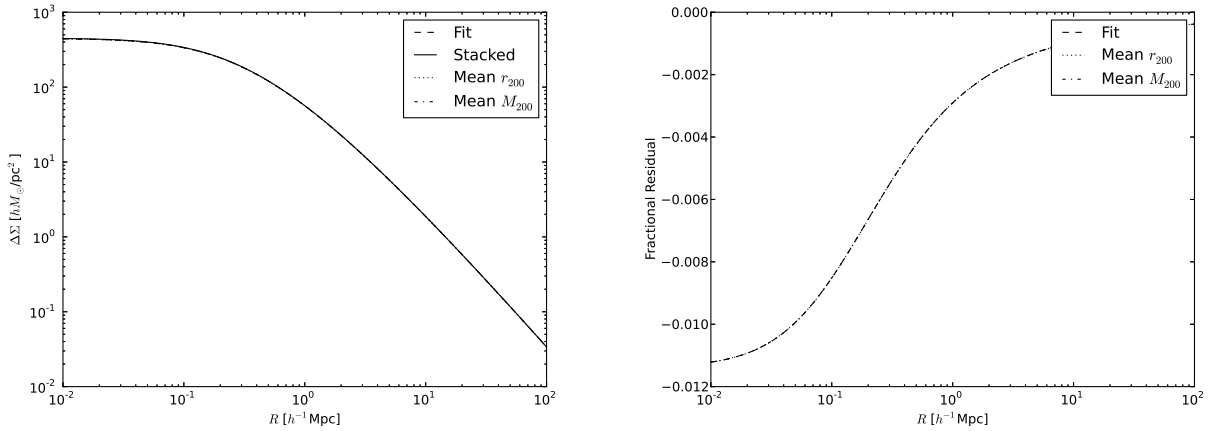

(a) $M_{200} : 13.80 - 19.95\ 10^{13} h^{-1} M_\odot$

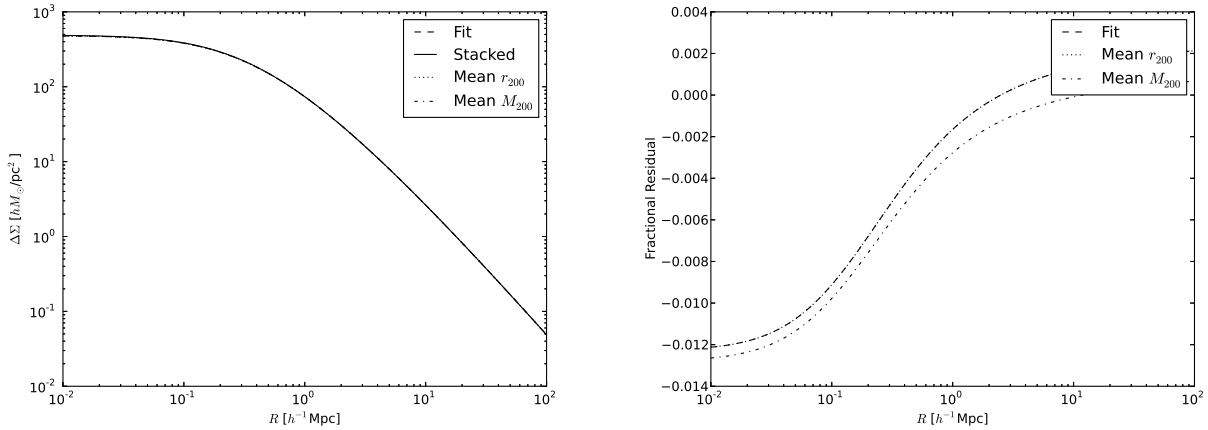

(b) $M_{200} : 19.95 - 28.84\ 10^{13} h^{-1} M_\odot$

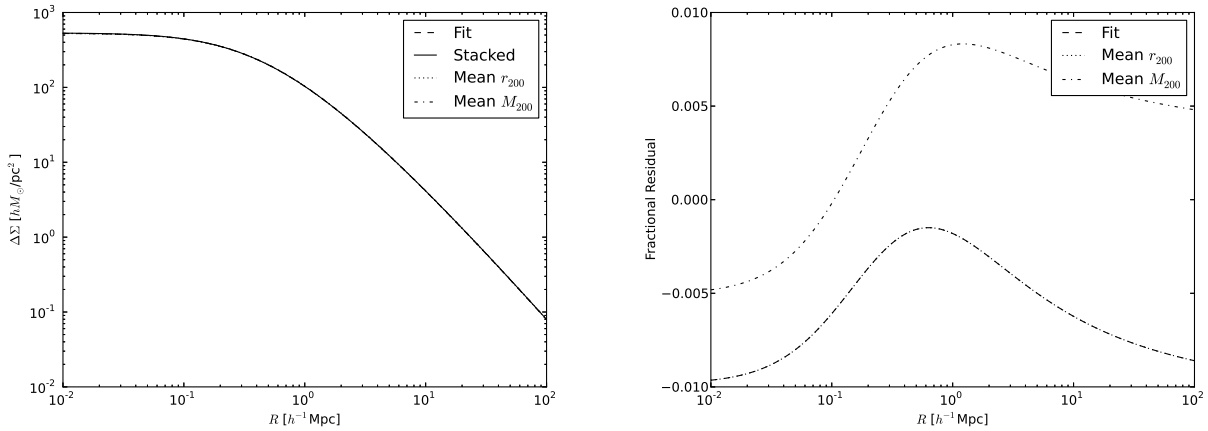

(c) $M_{200} : 28.84 - 89.13\ 10^{13} h^{-1} M_\odot$

Figure 6.2: NFW profiles binned by mass over $z = 0.0 - 1.0$ as well as their residual fraction.

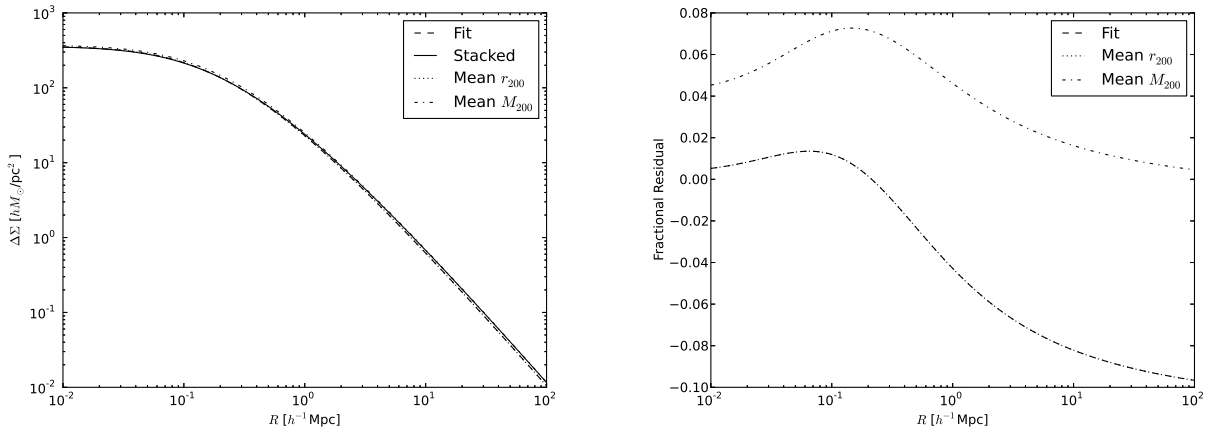

(a) $\Lambda : 19.7 - 21.3$

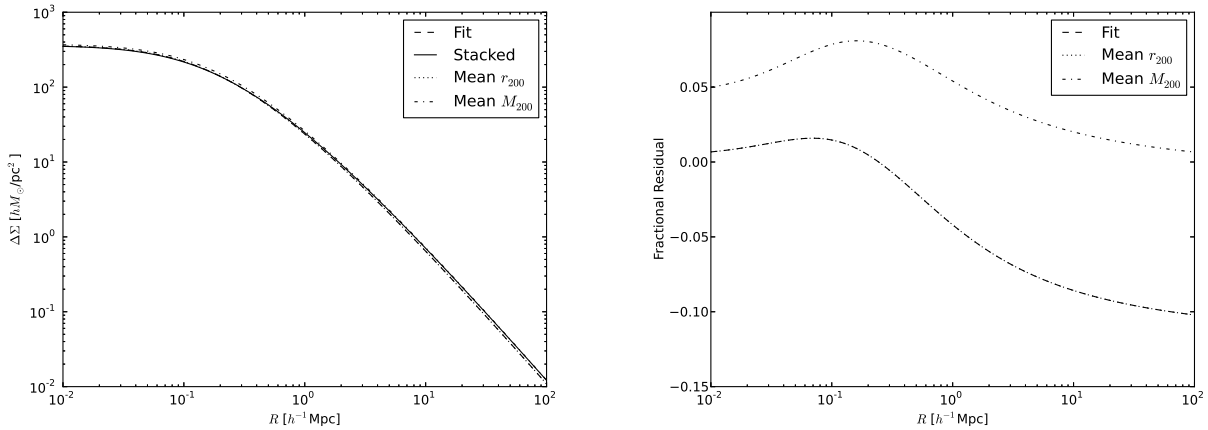

(b) $\Lambda : 21.3 - 22.8$

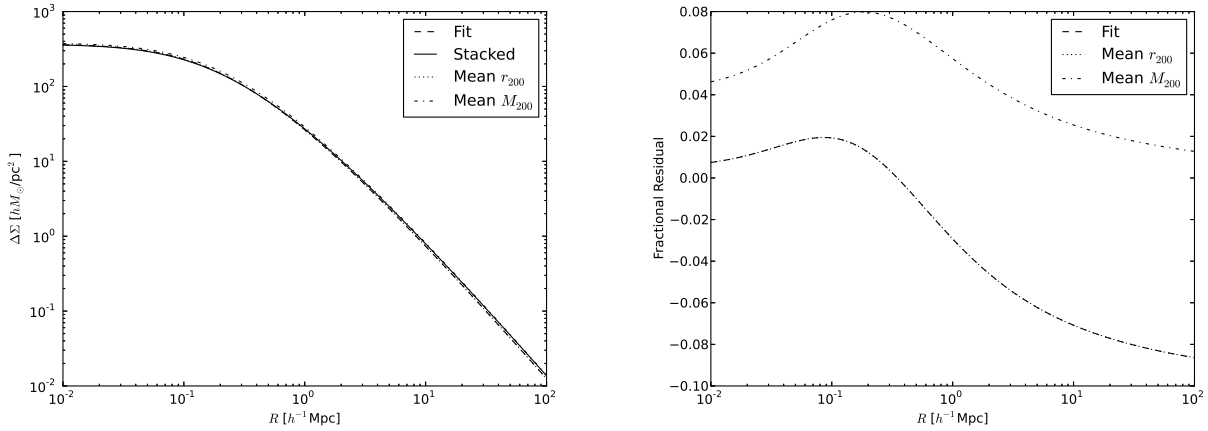

(c) $\Lambda : 22.8 - 24.4$

Figure 6.3: NFW profiles binned by richness over $z = 0.0 - 1.0$ as well as their residual.

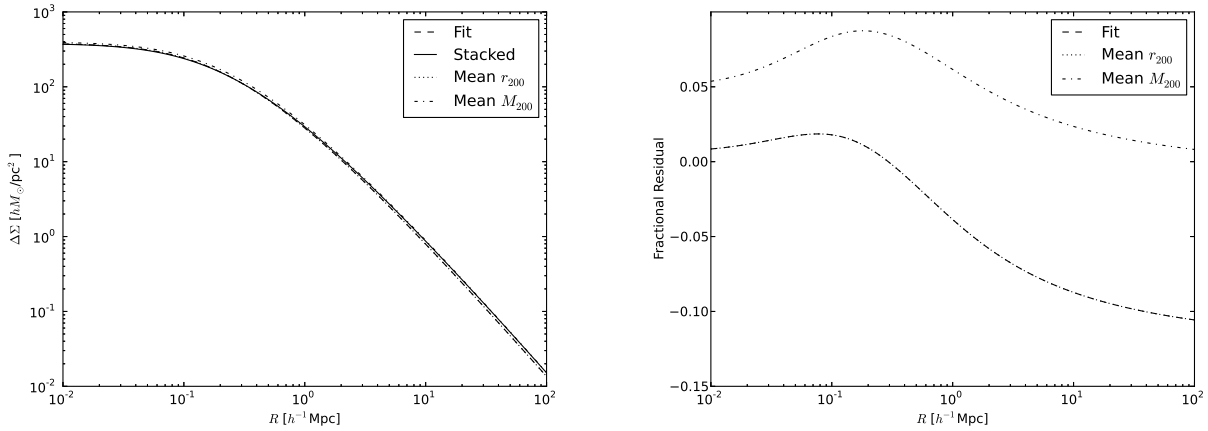

(a) $\Lambda : 24.4 - 26.0$

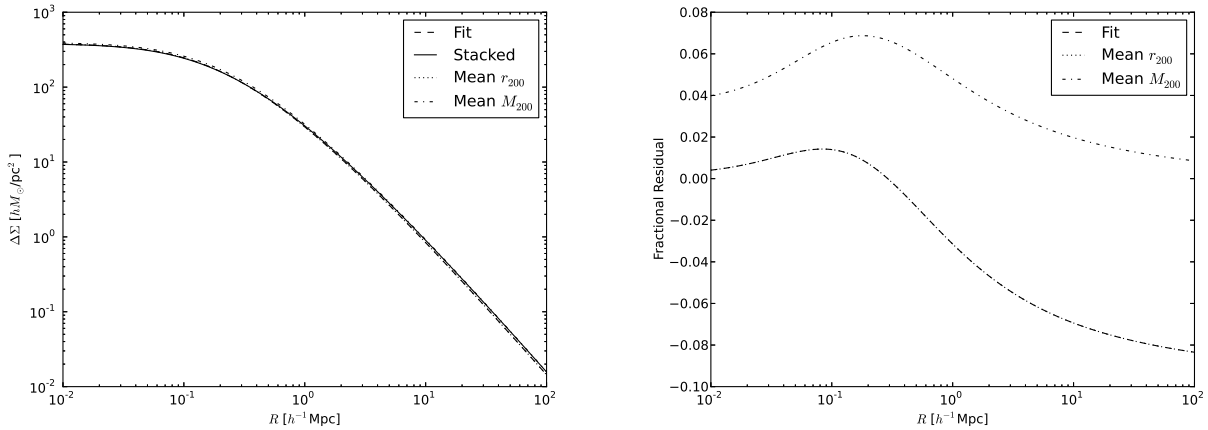

(b) $\Lambda : 26.0 - 27.5$

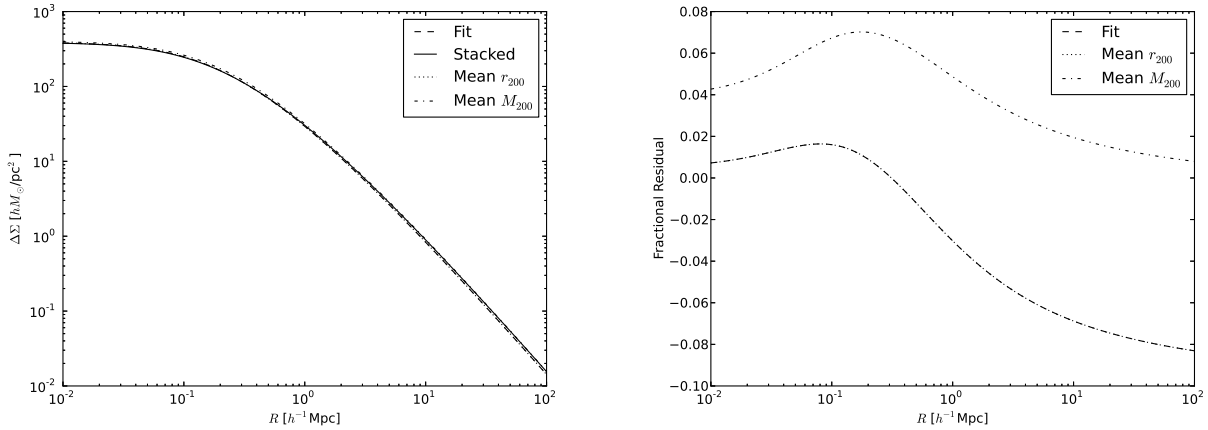

(c) $\Lambda : 27.5 - 29.1$

Figure 6.4: NFW profiles binned by richness over $z = 0.0 - 1.0$ as well as their residual.

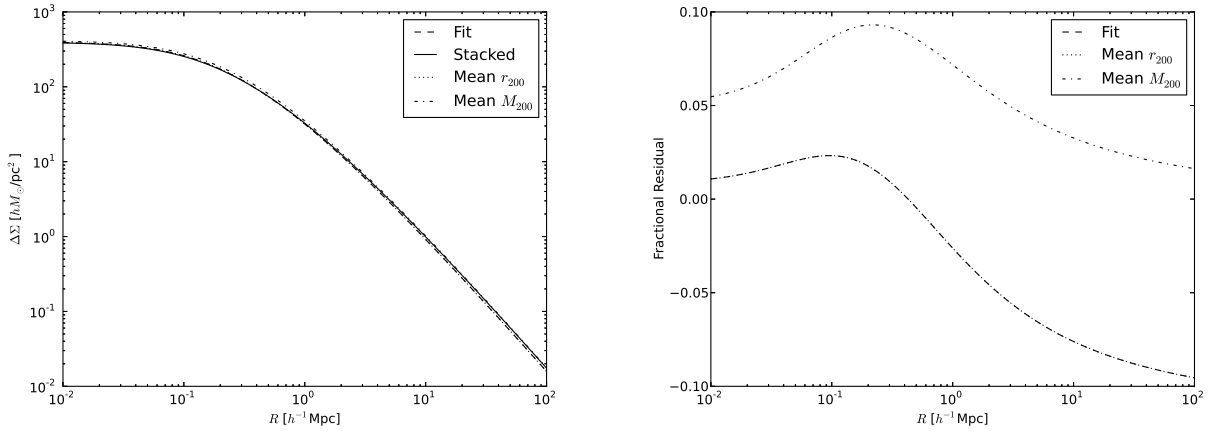

(a) $\Lambda : 29.1 - 33.8$

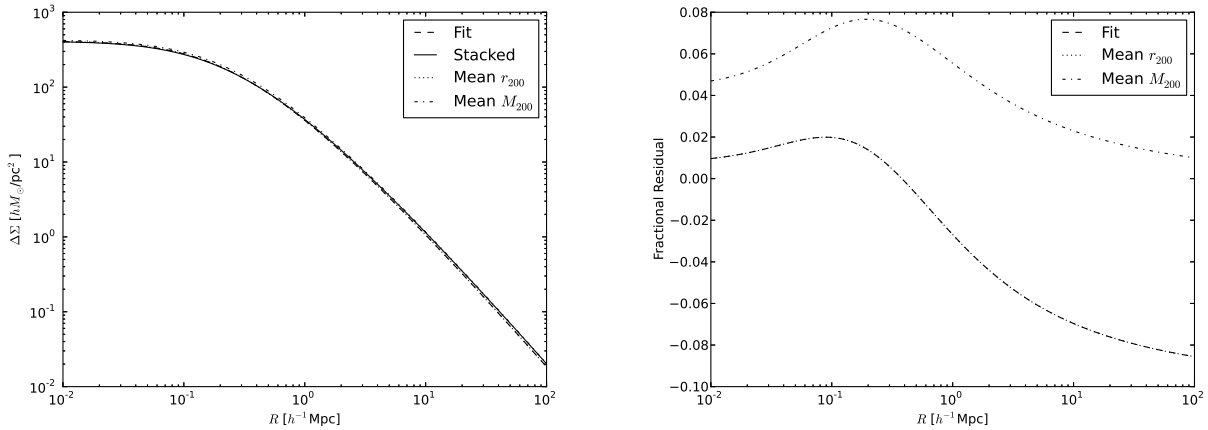

(b) $\Lambda : 33.8 - 43.2$

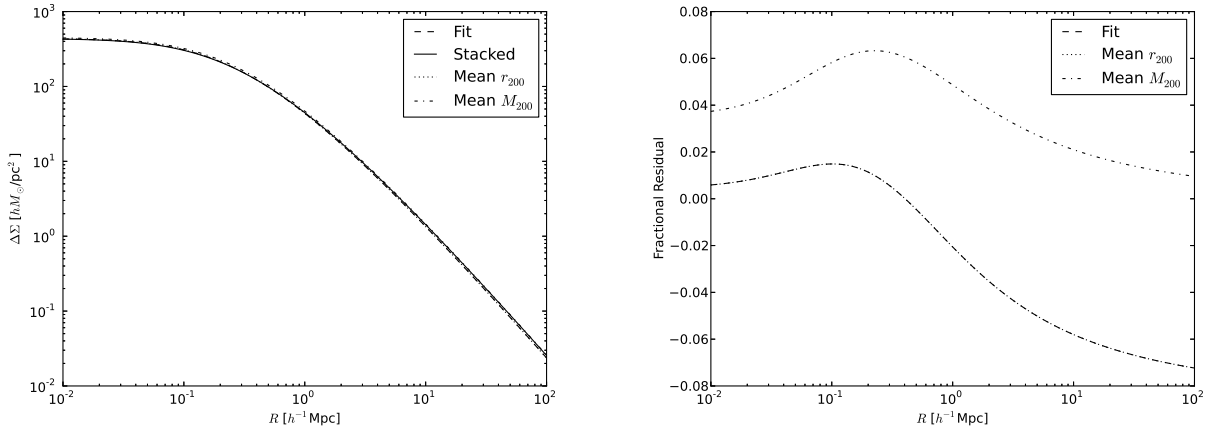

(c) $\Lambda : 43.2 - 55.8$

Figure 6.5: NFW profiles binned by richness over $z = 0.0 - 1.0$ as well as their residual.

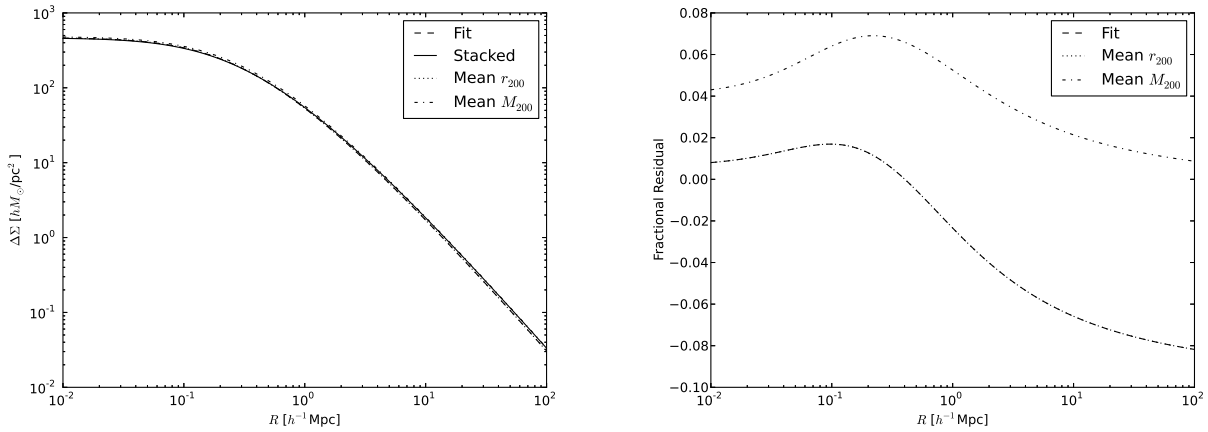

(a) $\Lambda : 55.8 - 79.3$

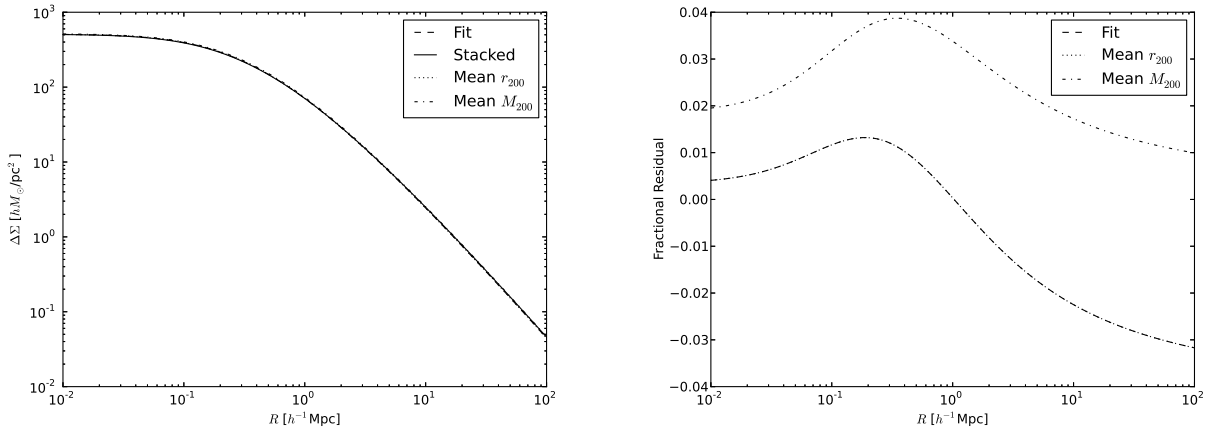

(b) $\Lambda : 79.3 - 126.3$

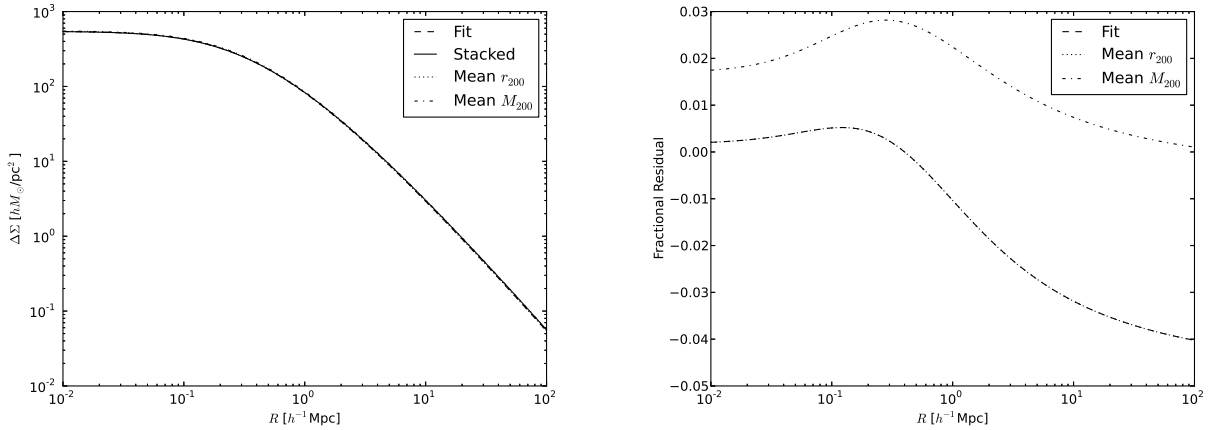

(c) $\Lambda : 126.3 - 361.6$

Figure 6.6: NFW profiles binned by richness over $z = 0.0 - 1.0$ as well as their residual.

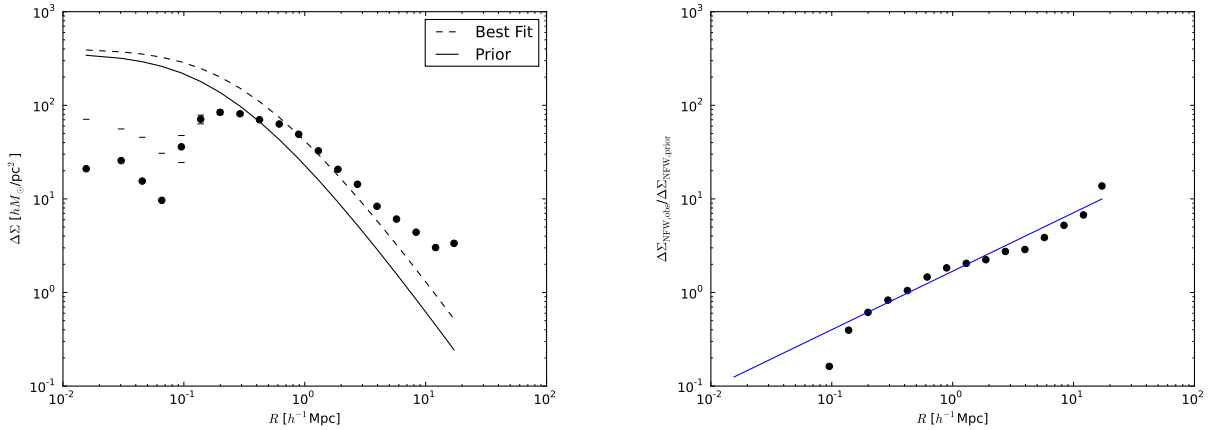

(a) $\Lambda : 19.7 - 21.3$

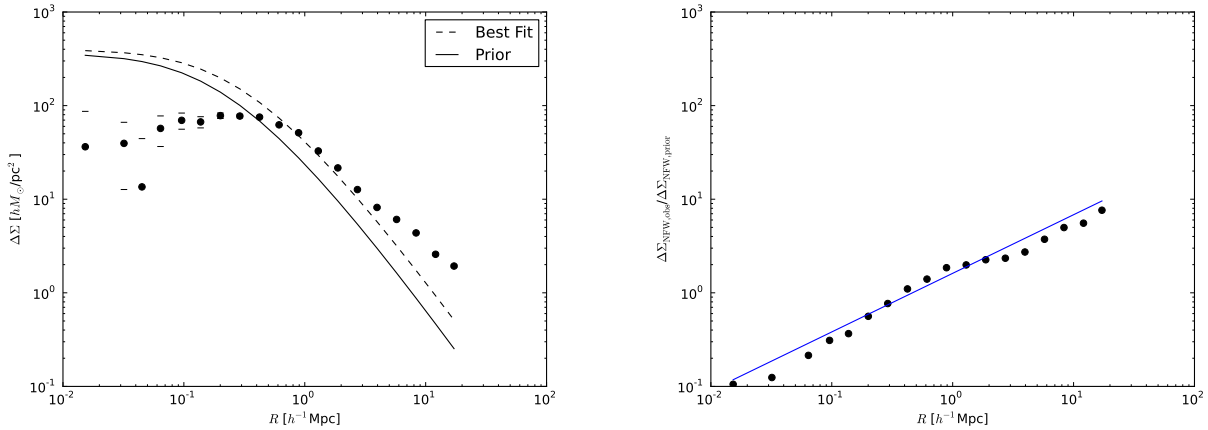

(b) $\Lambda : 21.3 - 22.8$

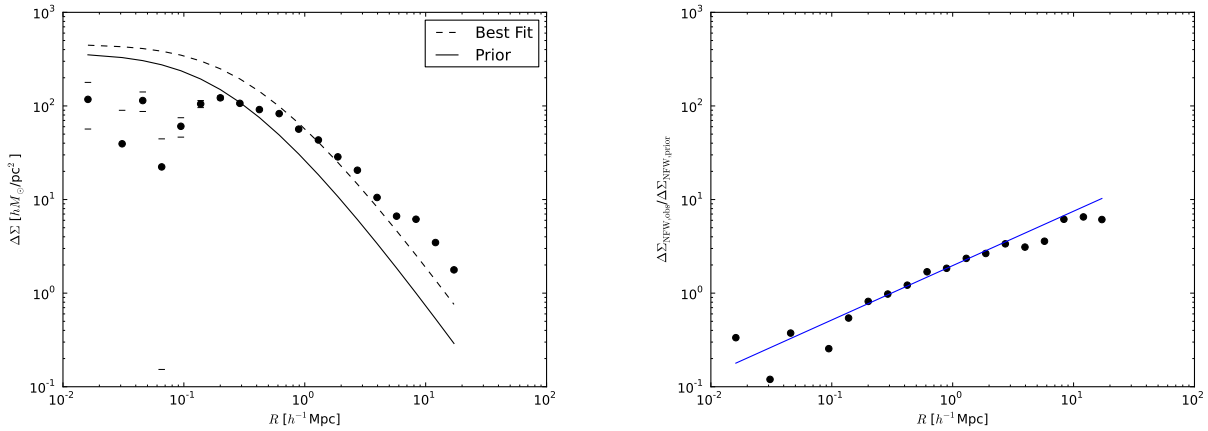

(c) $\Lambda : 22.8 - 24.4$

Figure 6.7: "Observed" $\Delta\Sigma$ profiles for halos binned by richness as well as their fractional error to the prior NFW.

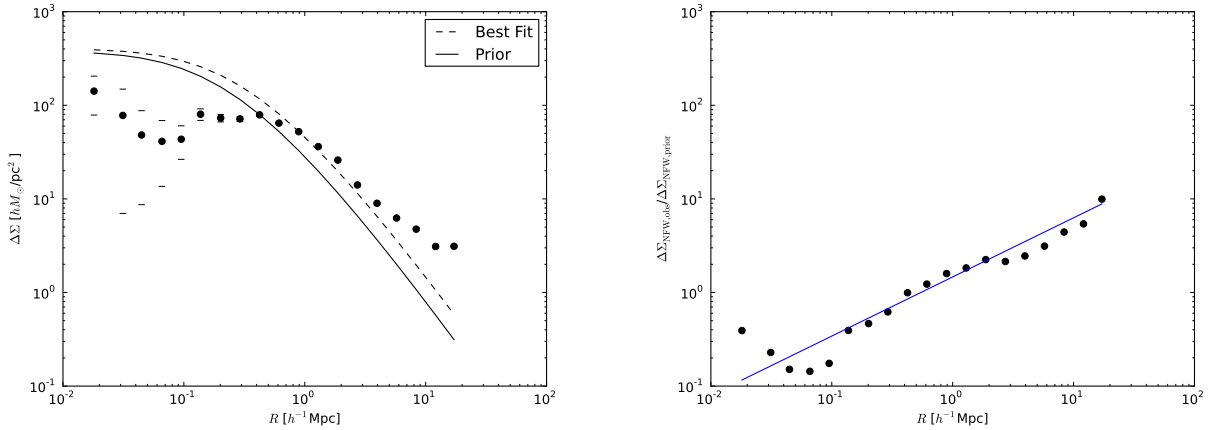

(a) $\Lambda : 24.4 - 26.0$

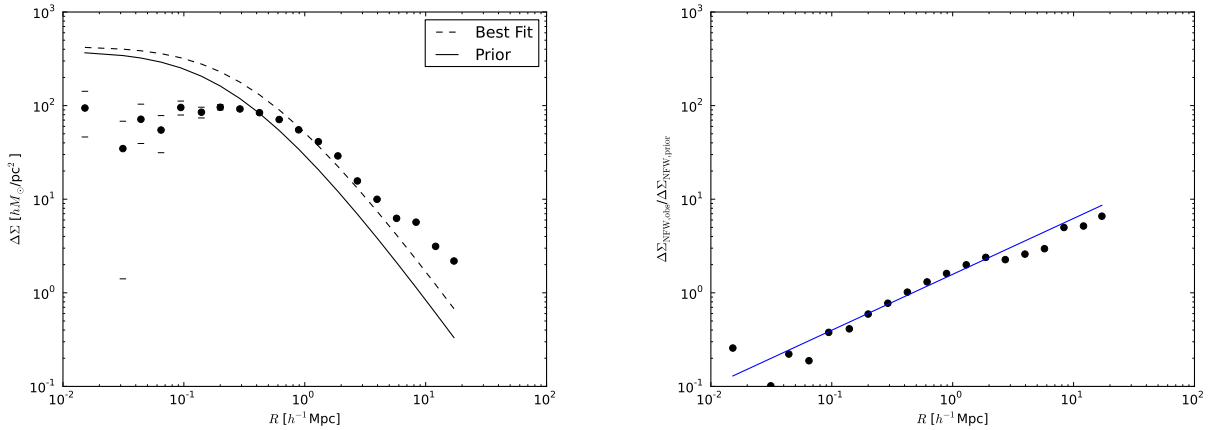

(b) $\Lambda : 26.0 - 27.5$

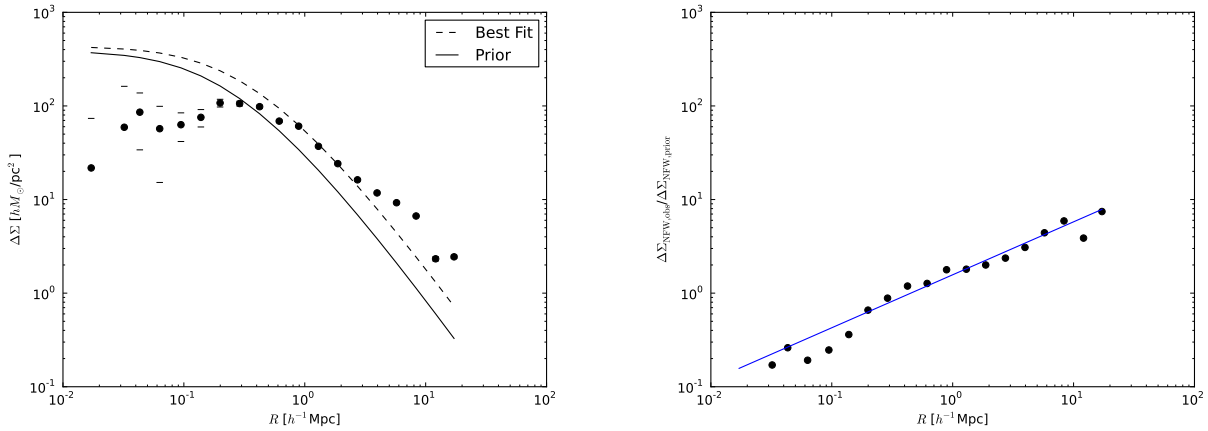

(c) $\Lambda : 27.5 - 29.1$

Figure 6.8: "Observed" $\Delta\Sigma$ profiles for halos binned by richness as well as their fractional error to the prior NFW.

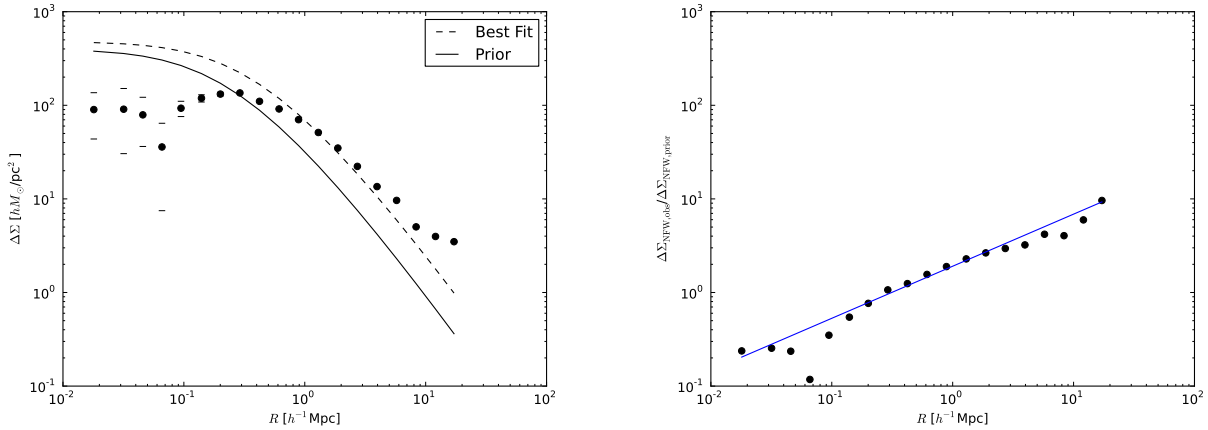

(a) $\Lambda : 29.1 - 33.8$

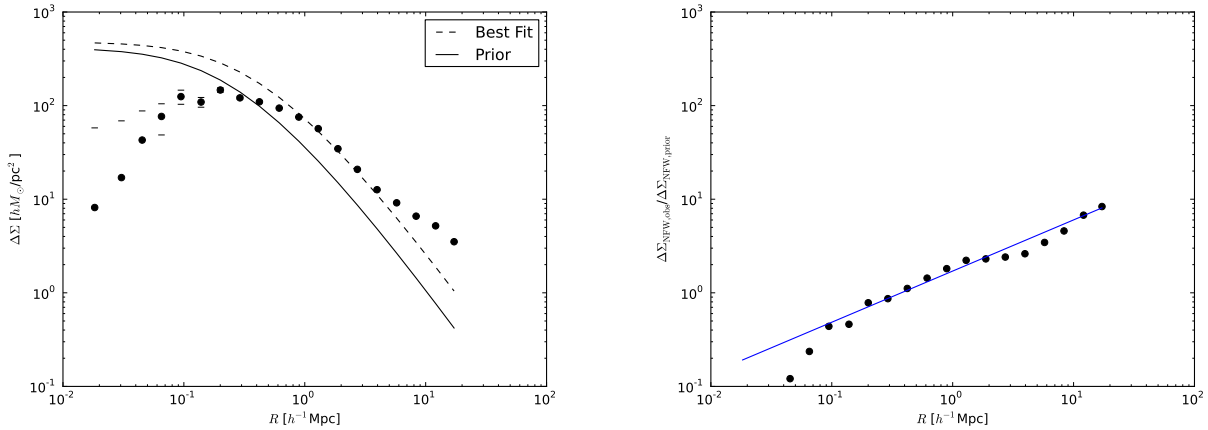

(b) $\Lambda : 33.8 - 43.2$

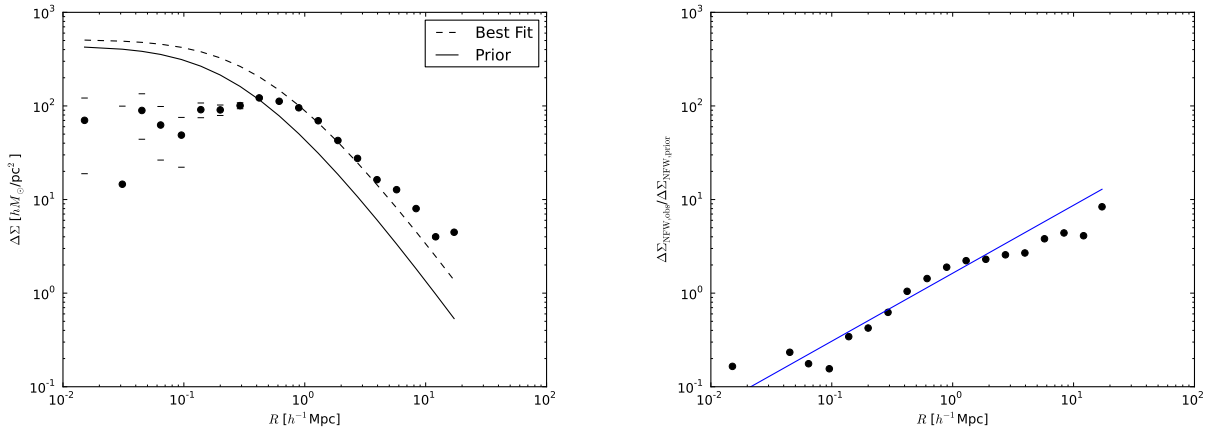

(c) $\Lambda : 43.2 - 55.8$

Figure 6.9: "Observed" $\Delta\Sigma$ profiles for halos binned by richness as well as their fractional error to the prior NFW.

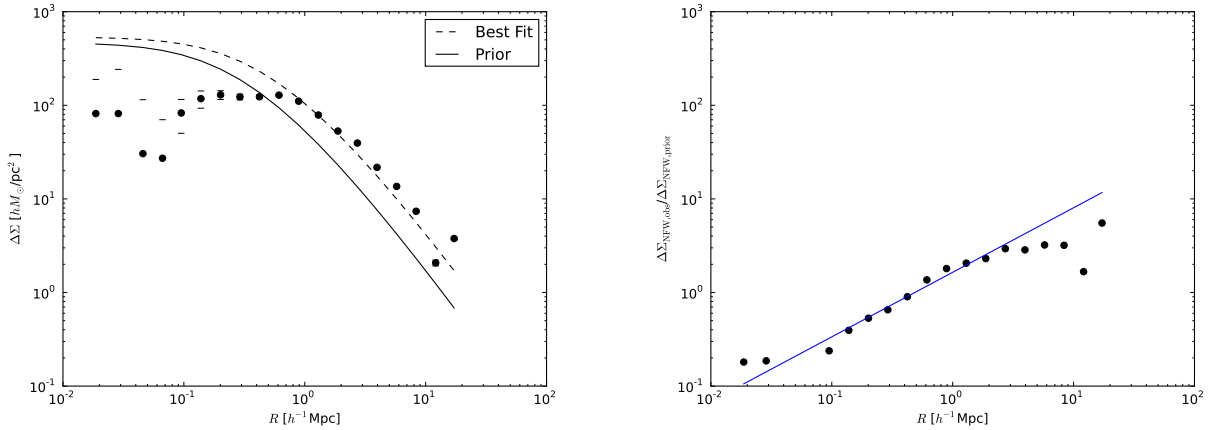

(a) $\Lambda : 55.8 - 79.3$

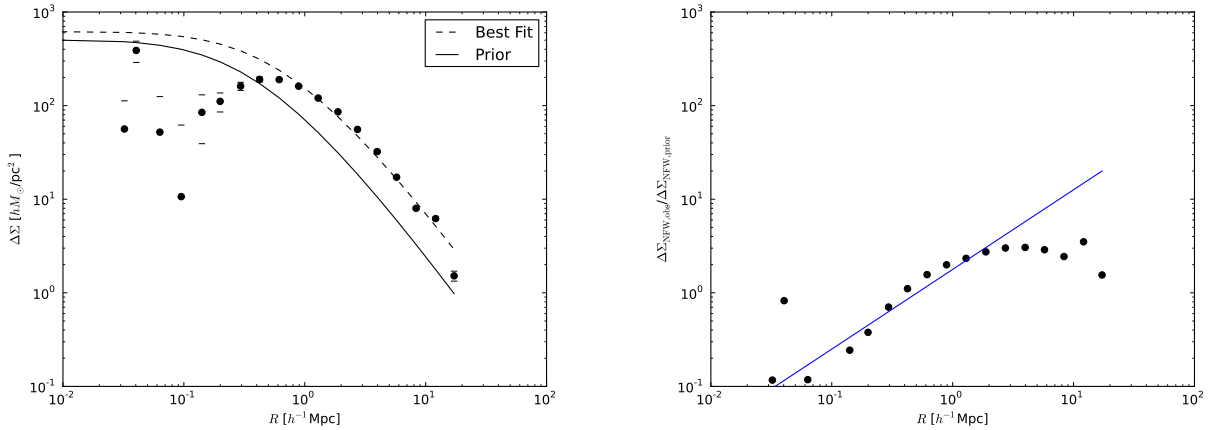

(b) $\Lambda : 79.3 - 126.3$

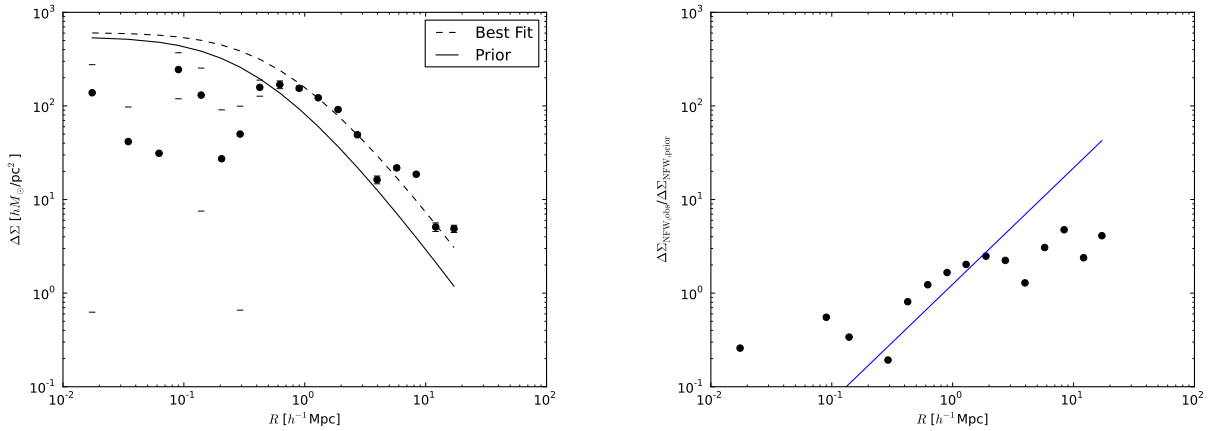

(c) $\Lambda : 126.3 - 361.6$

Figure 6.10: "Observed" $\Delta\Sigma$ profiles for halos binned by richness as well as their fractional error to the prior NFW.

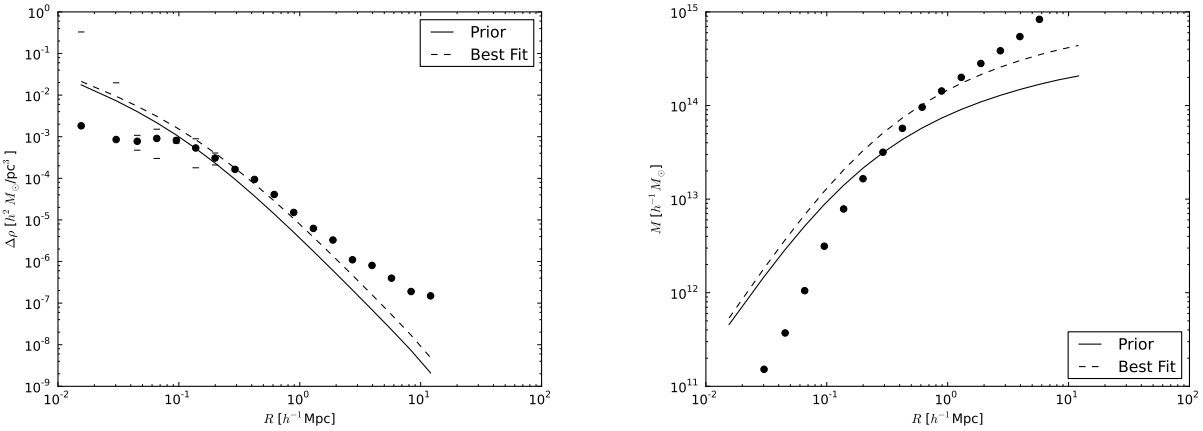

(a) $\Lambda : 19.7 - 21.3$

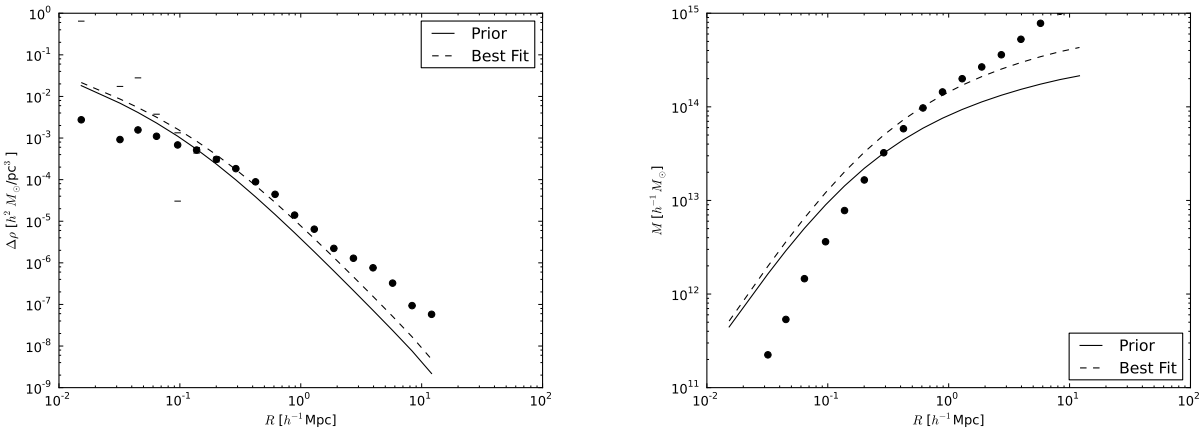

(b) $\Lambda : 21.3 - 22.8$

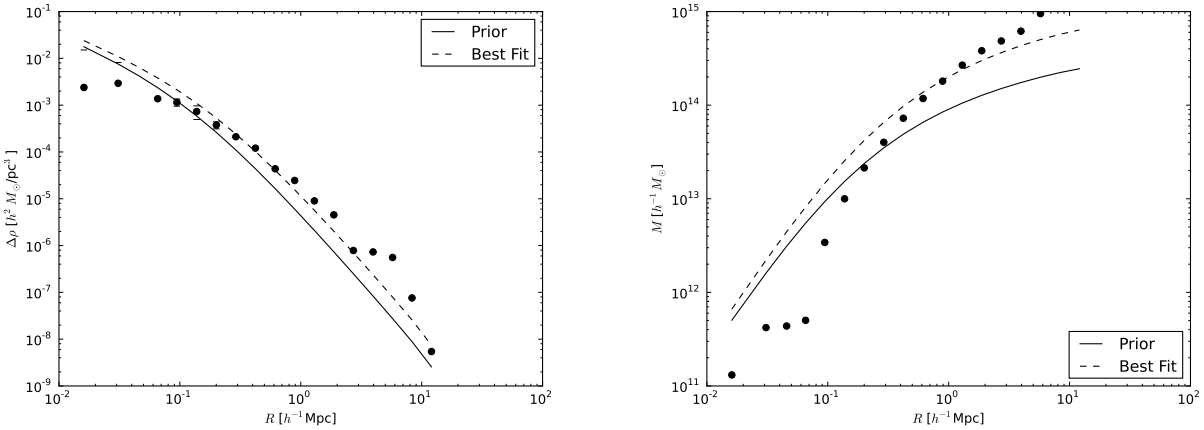

(c) $\Lambda : 22.8 - 24.4$

Figure 6.11: "Observed" deprojected $\Delta\rho$ and M profiles for halos binned by richness.

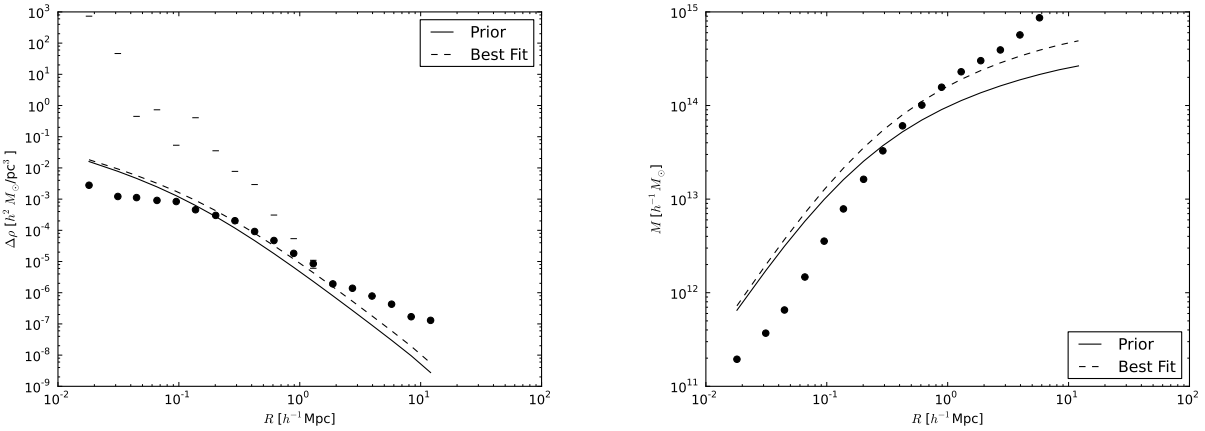

(a) $\Lambda : 24.4 - 26.0$

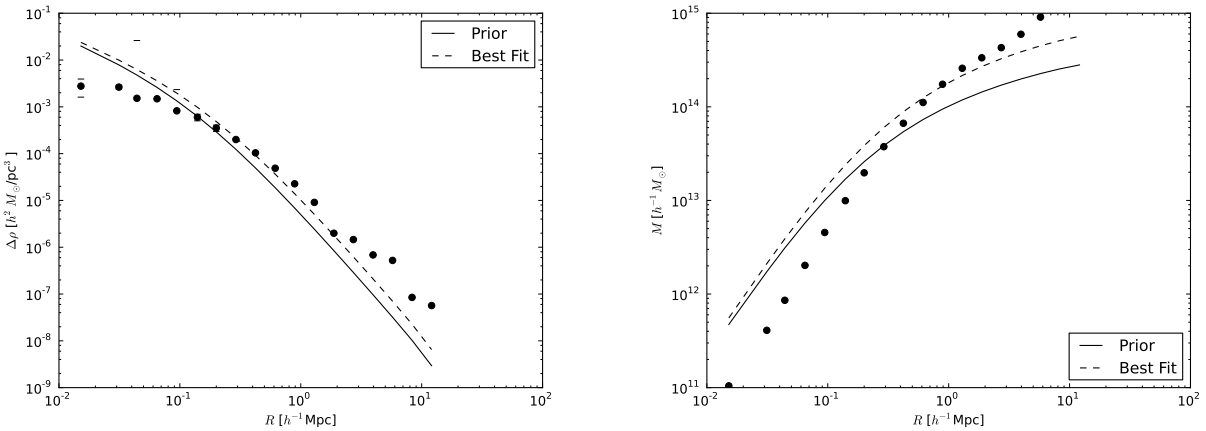

(b) $\Lambda : 26.0 - 27.5$

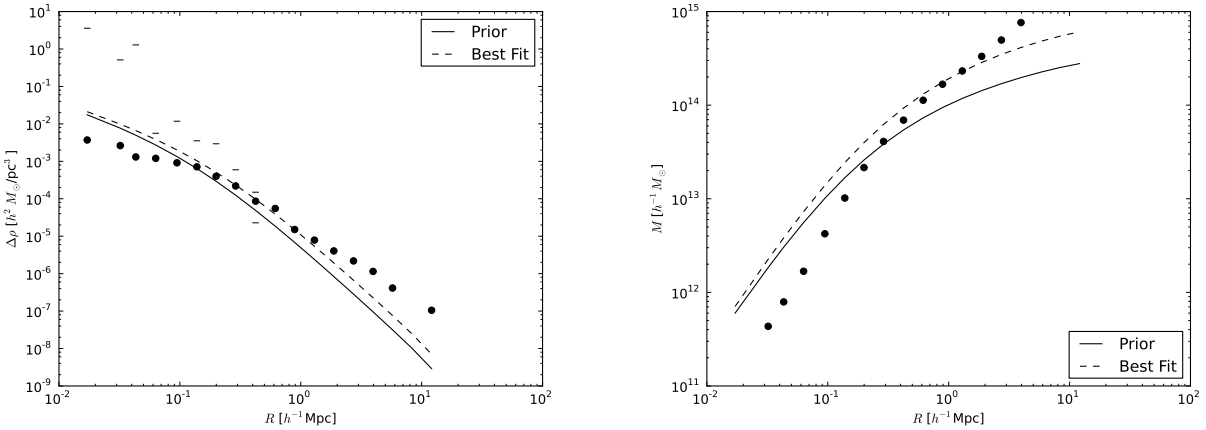

(c) $\Lambda : 27.5 - 29.1$

Figure 6.12: "Observed" deprojected $\Delta\rho$ and M profiles for halos binned by richness.

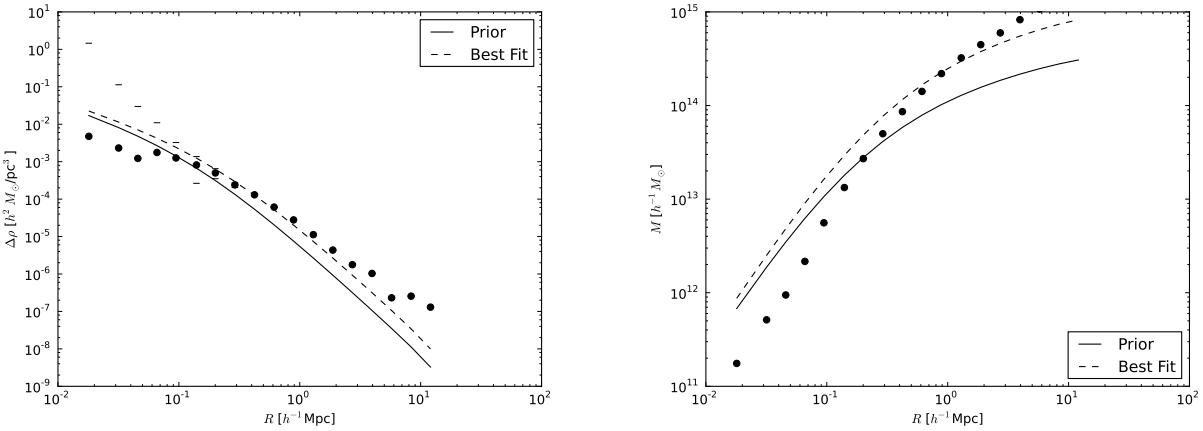

(a) $\Lambda : 29.1 - 33.8$

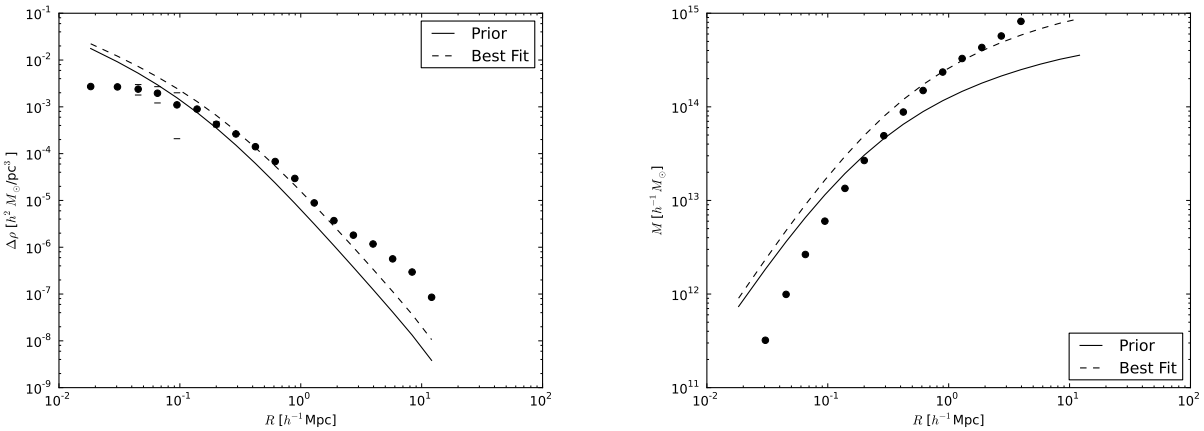

(b) $\Lambda : 33.8 - 43.2$

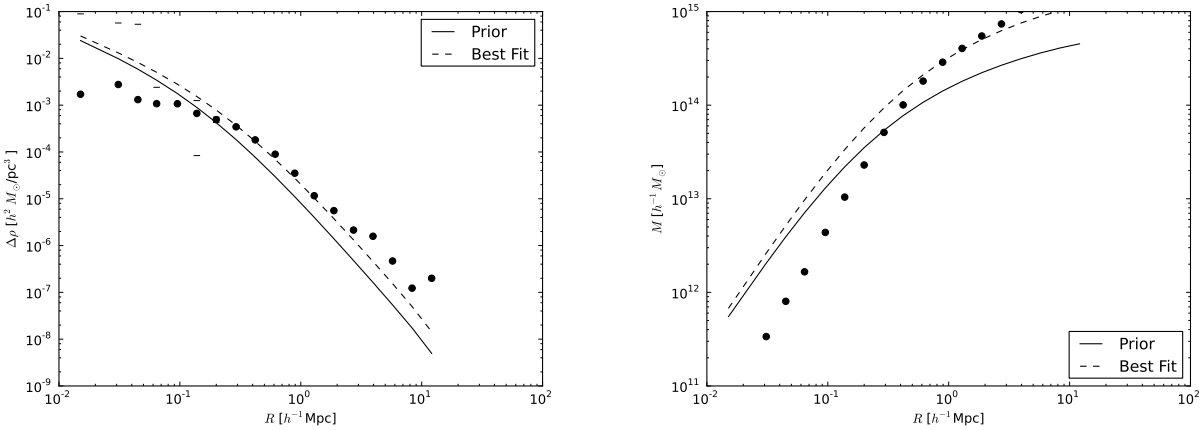

(c) $\Lambda : 43.2 - 55.8$

Figure 6.13: "Observed" deprojected $\Delta\rho$ and M profiles for halos binned by richness.

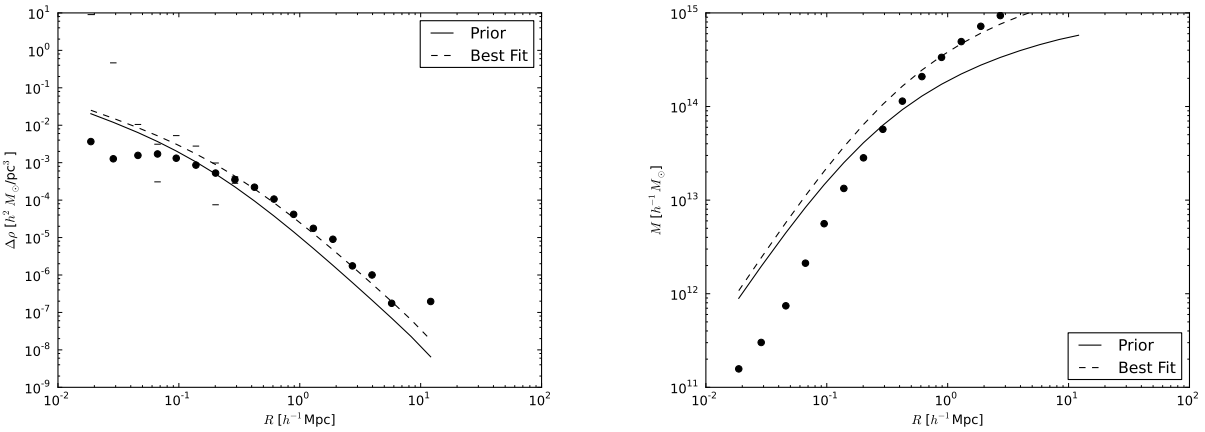

(a) $\Lambda : 55.8 - 79.3$

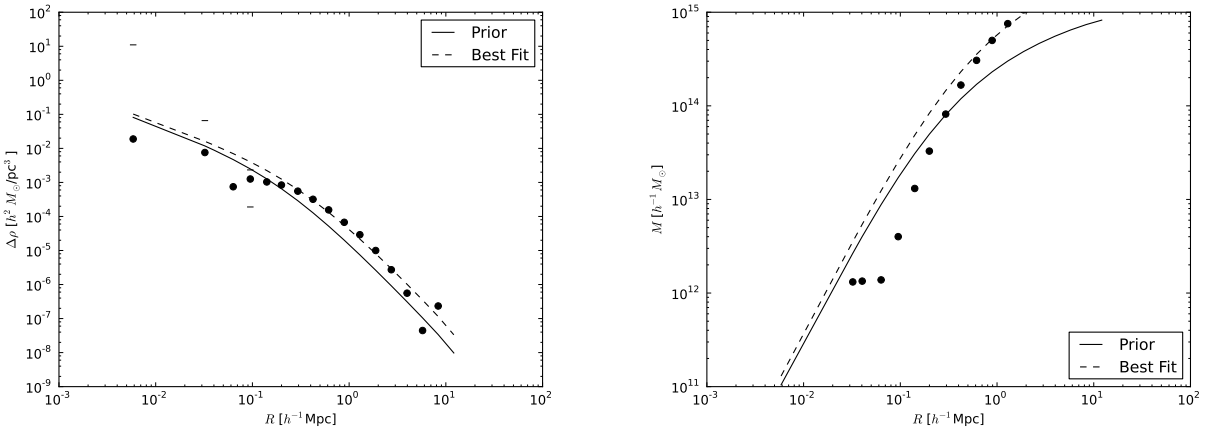

(b) $\Lambda : 79.3 - 126.3$

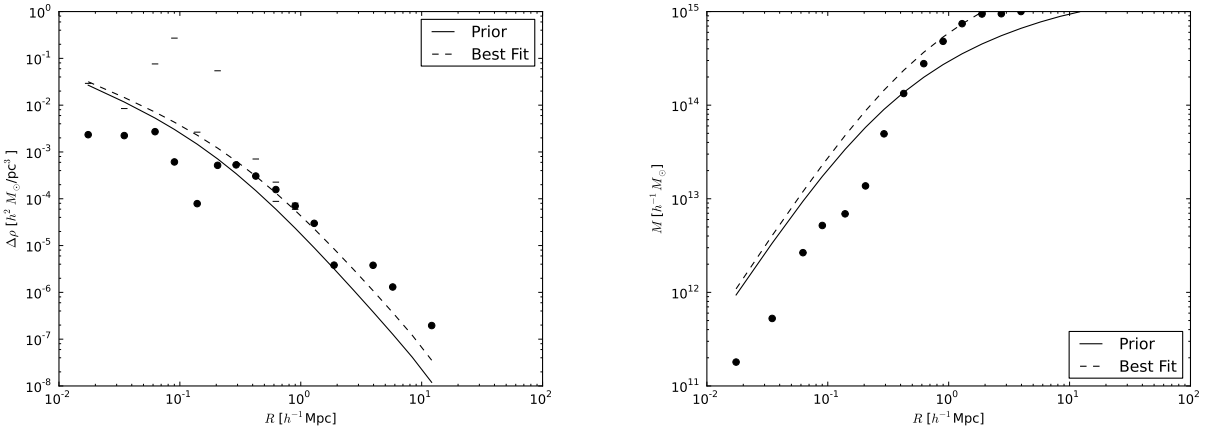

(c) $\Lambda : 126.3 - 361.6$

Figure 6.14: "Observed" deprojected $\Delta\rho$ and M profiles for halos binned by richness.

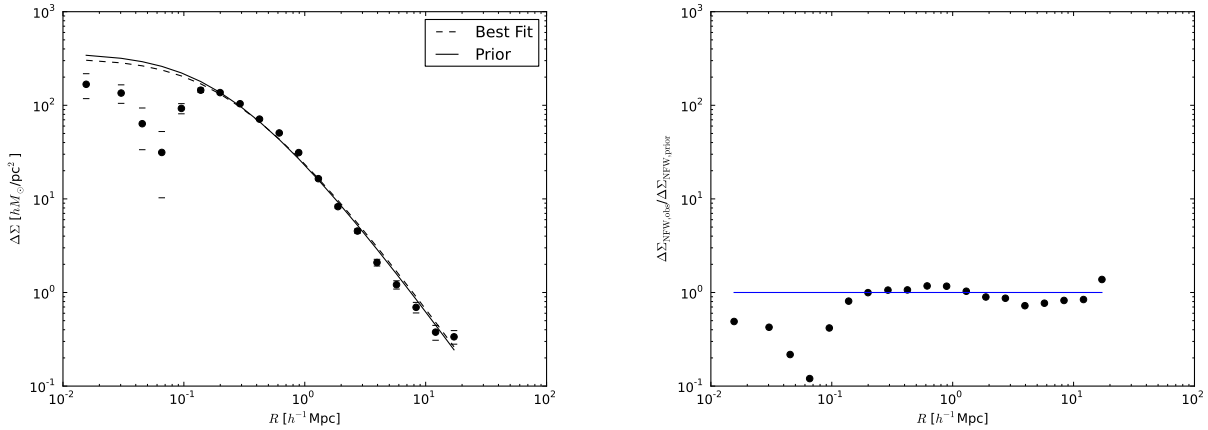

(a) $\Lambda : 19.7 - 21.3$

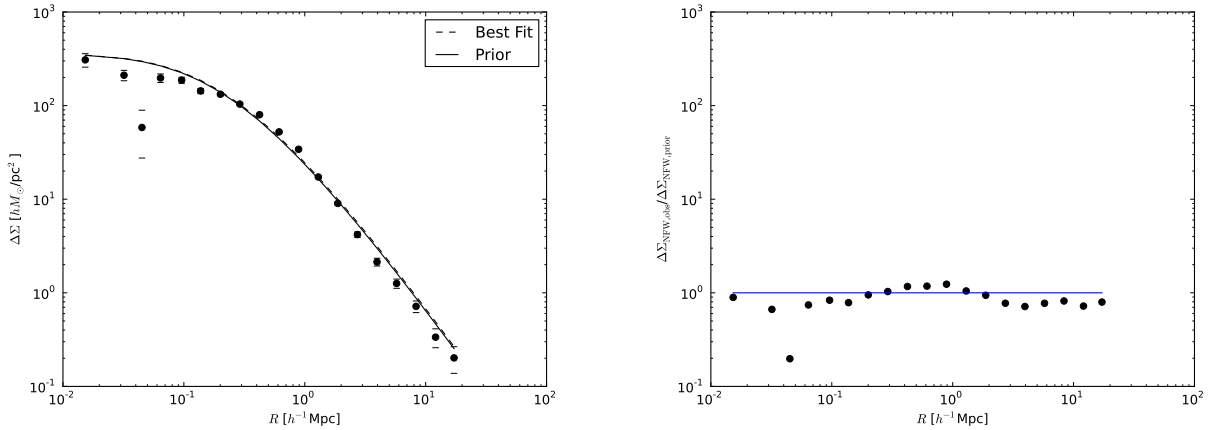

(b) $\Lambda : 21.3 - 22.8$

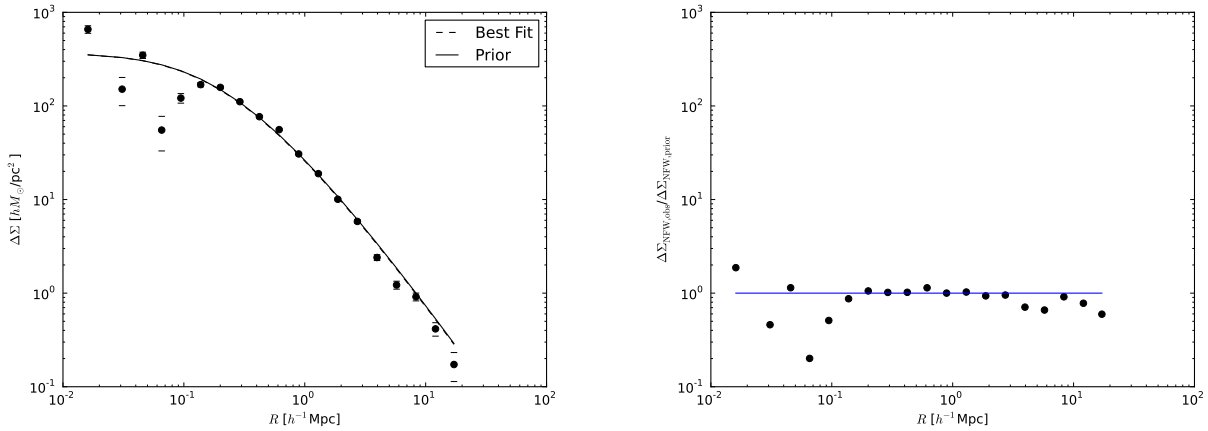

(c) $\Lambda : 22.8 - 24.4$

Figure 6.15: "Observed" and corrected $\Delta\Sigma$ profiles (see Section 4.1) for halos binned by richness as well as their fractional error to the expected NFW profile.

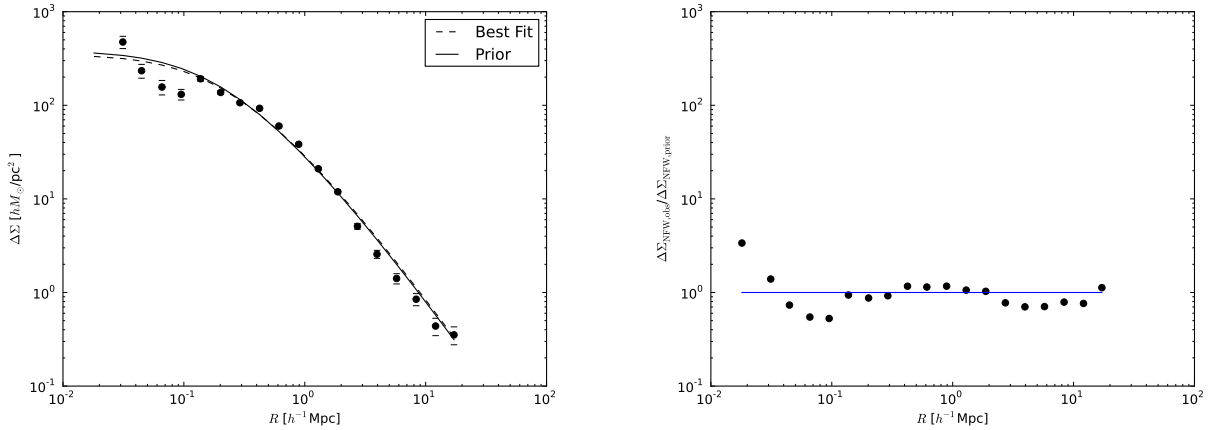

(a) $\Lambda : 24.4 - 26.0$

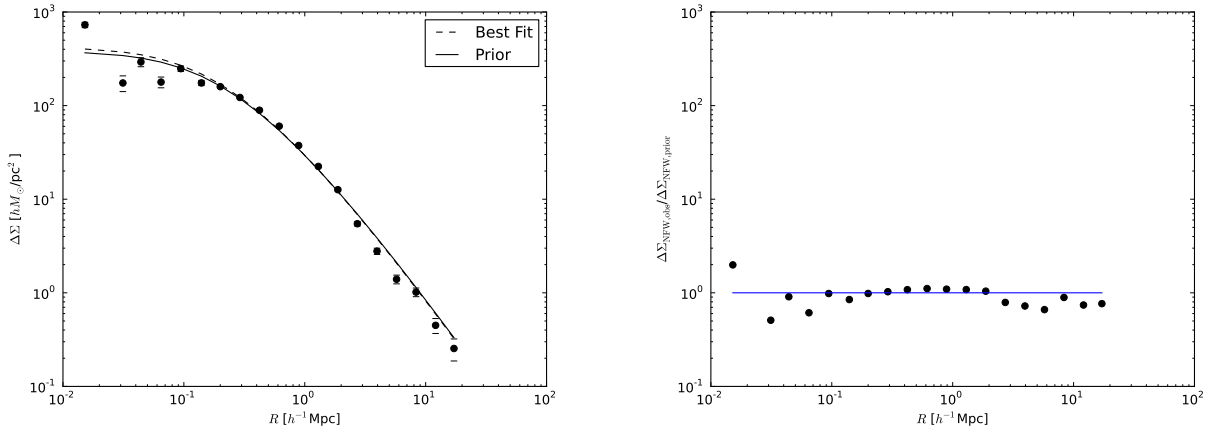

(b) $\Lambda : 26.0 - 27.5$

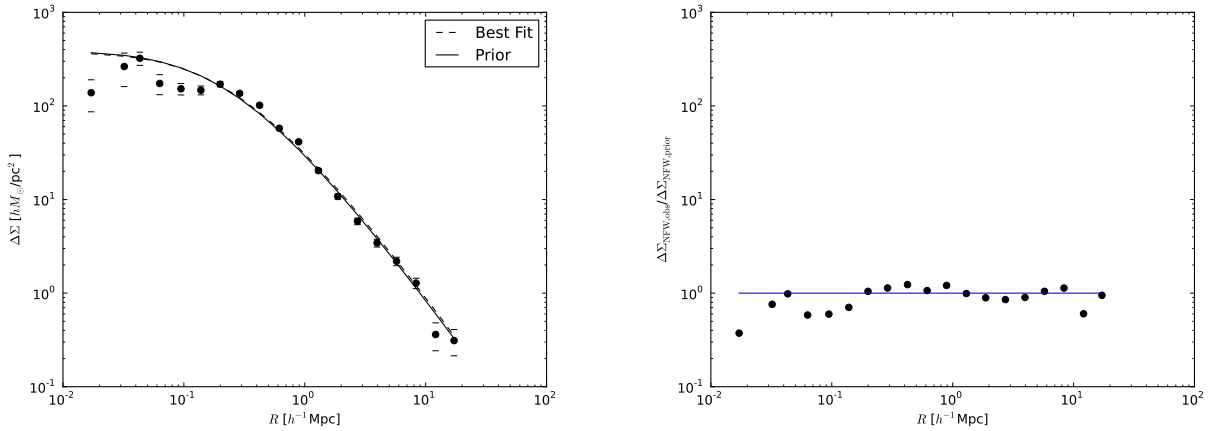

(c) $\Lambda : 27.5 - 29.1$

Figure 6.16: "Observed" and corrected $\Delta\Sigma$ profiles (see Section 4.1) for halos binned by richness as well as their fractional error to the expected NFW profile.

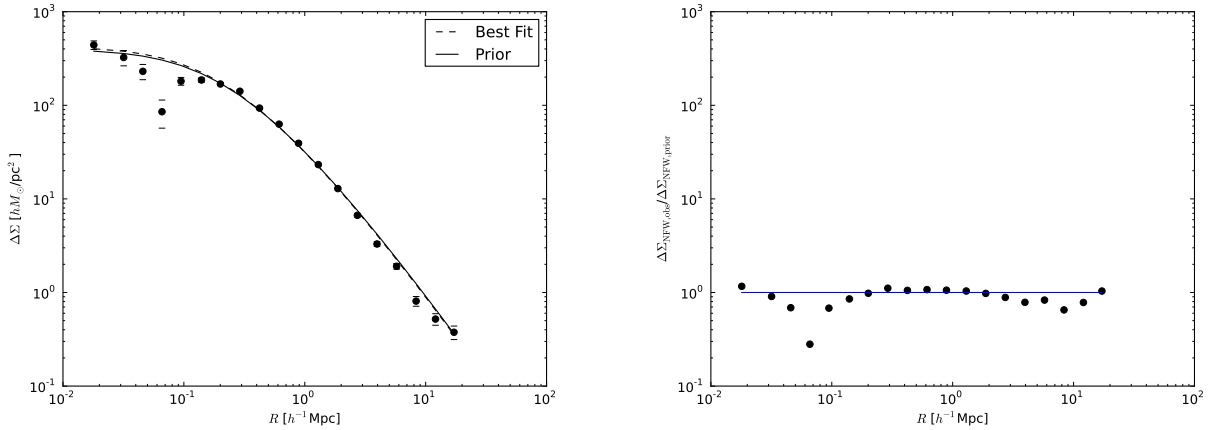

(a) $\Lambda : 29.1 - 33.8$

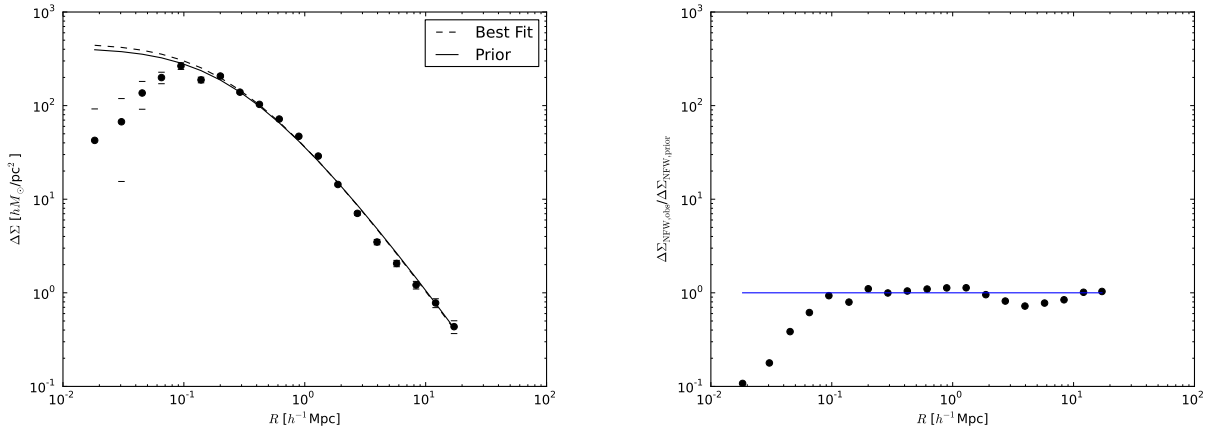

(b) $\Lambda : 33.8 - 43.2$

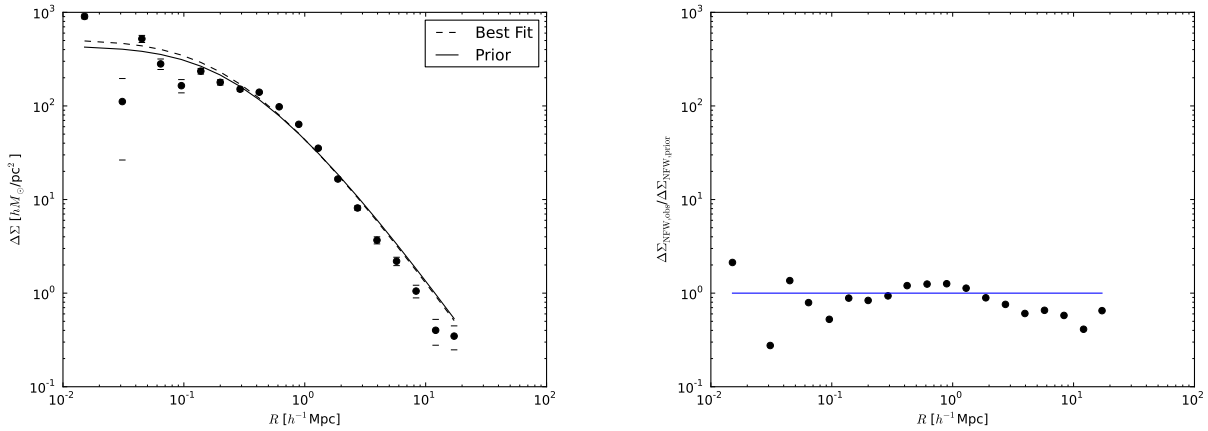

(c) $\Lambda : 43.2 - 55.8$

Figure 6.17: "Observed" and corrected $\Delta\Sigma$ profiles (see Section 4.1) for halos binned by richness as well as their fractional error to the expected NFW profile.

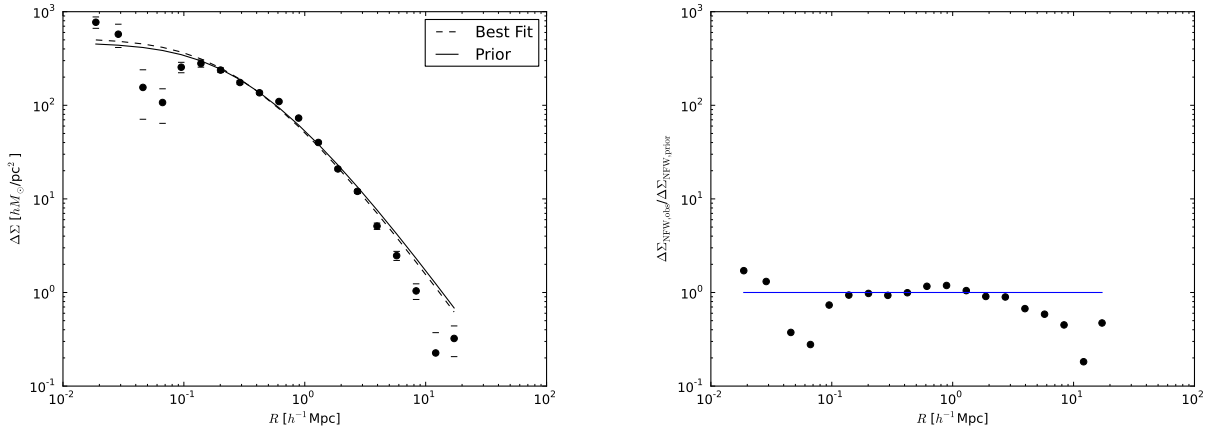

(a) $\Lambda : 55.8 - 79.3$

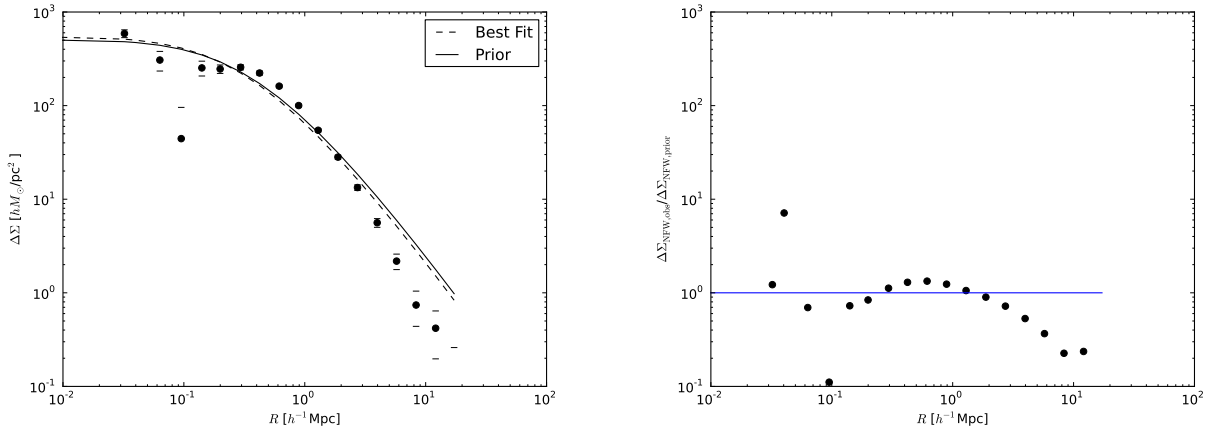

(b) $\Lambda : 79.3 - 126.3$

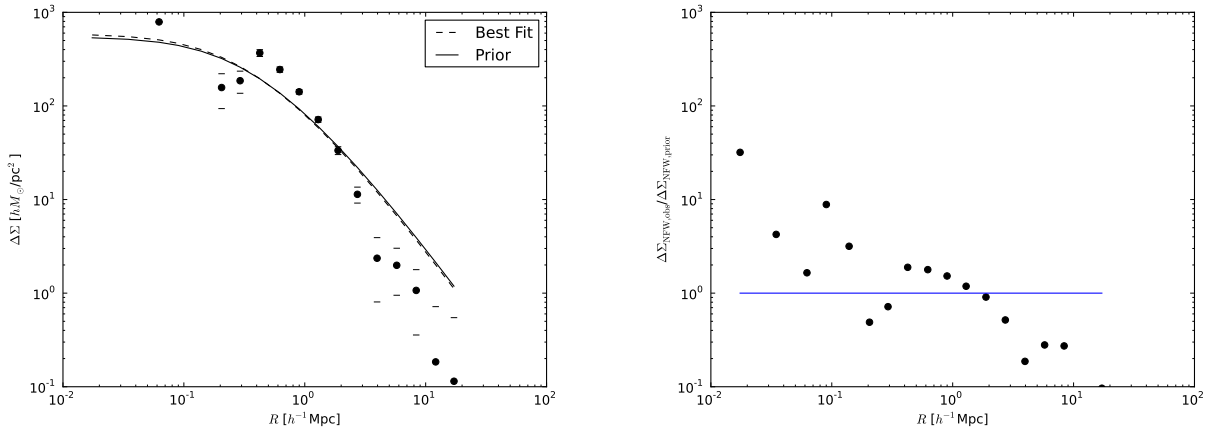

(c) $\Lambda : 126.3 - 361.6$

Figure 6.18: "Observed" and corrected $\Delta\Sigma$ profiles (see Section 4.1) for halos binned by richness as well as their fractional error to the expected NFW profile.

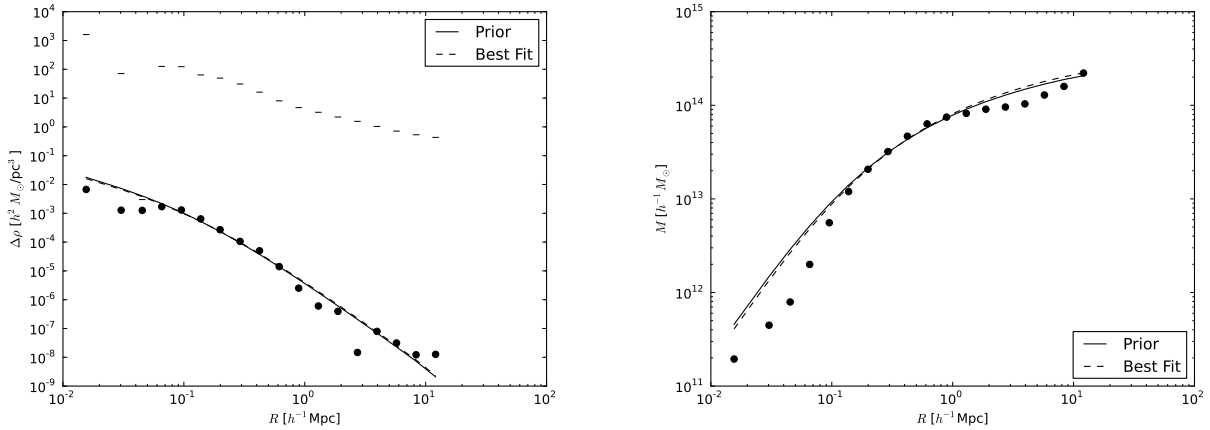

(a) $\Lambda : 19.7 - 21.3$

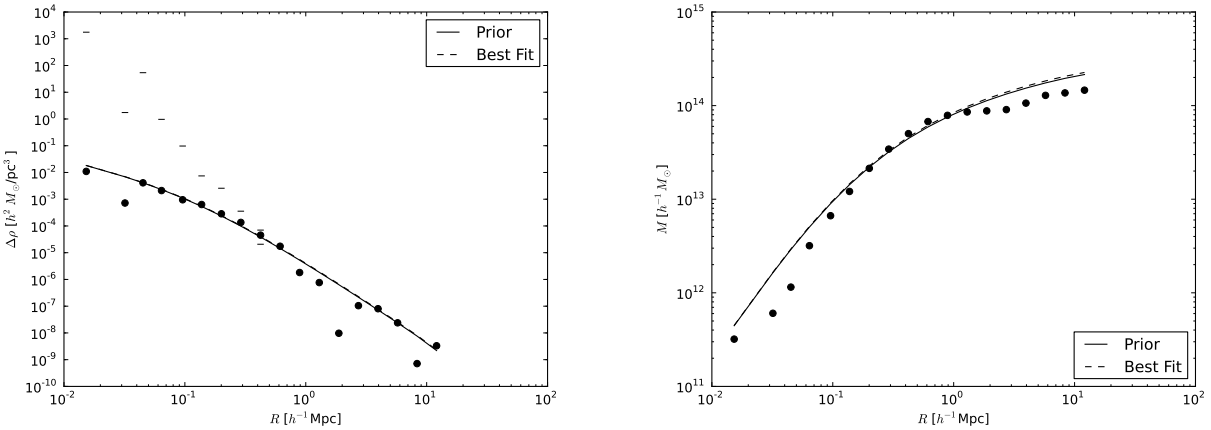

(b) $\Lambda : 21.3 - 22.8$

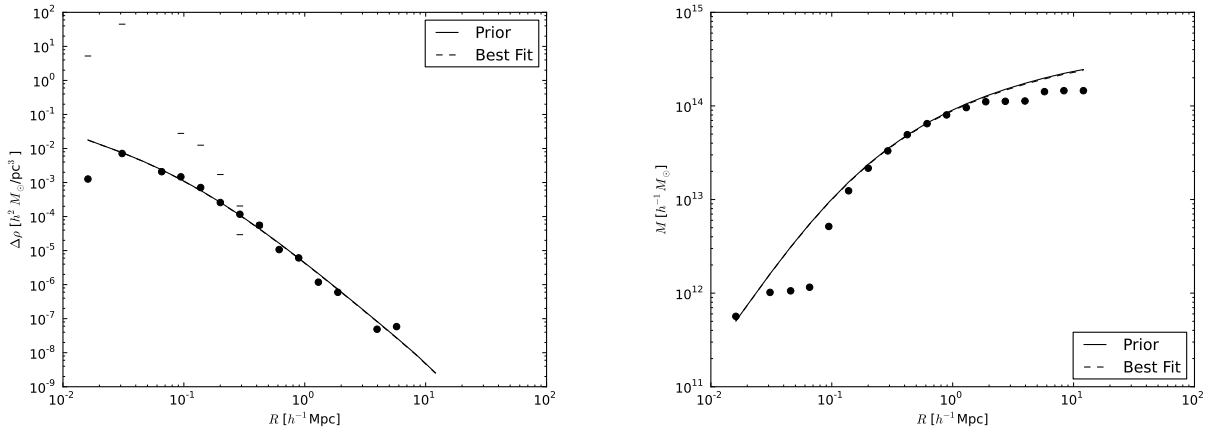

(c) $\Lambda : 22.8 - 24.4$

Figure 6.19: "Observed" and corrected (see Section 4.1) deprojected $\Delta\rho$ and M profiles for halos binned by richness.

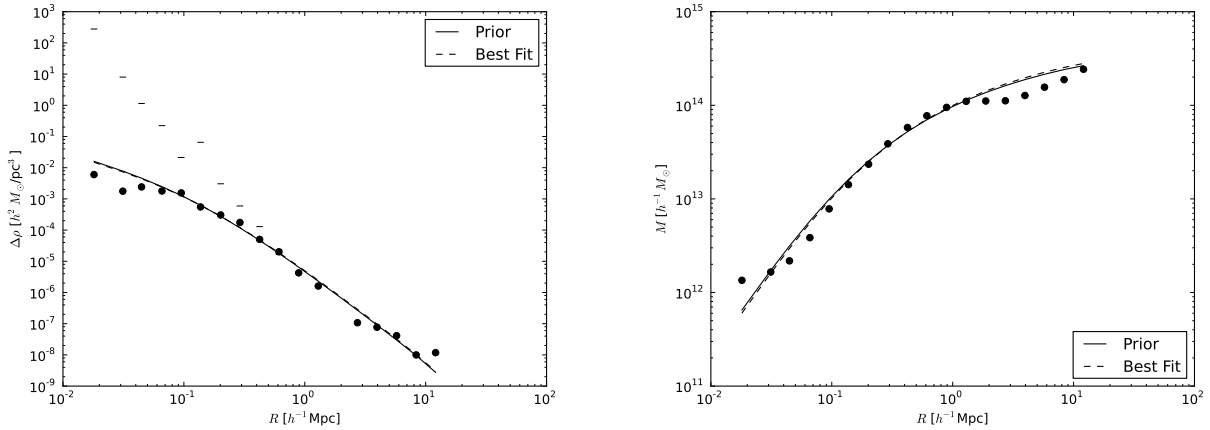

(a) $\Lambda : 24.4 - 26.0$

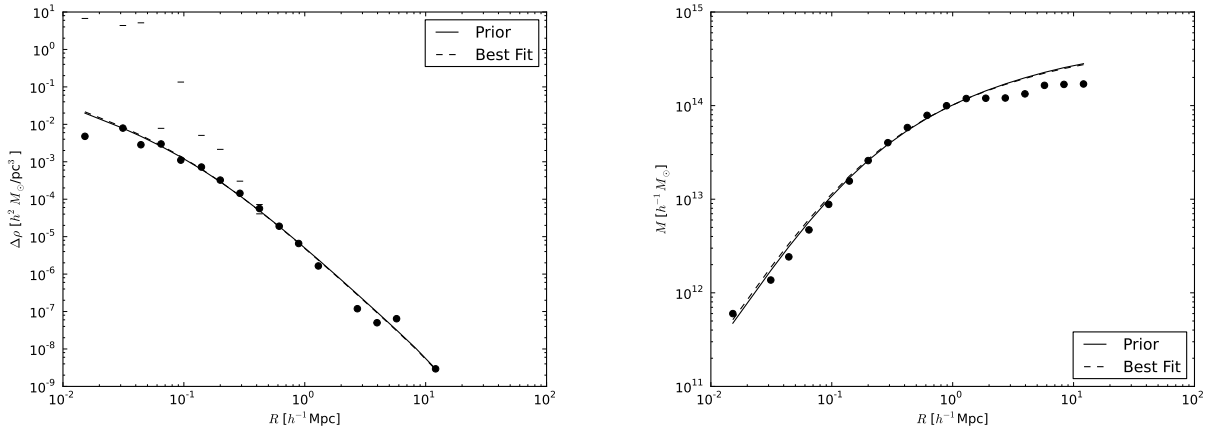

(b) $\Lambda : 26.0 - 27.5$

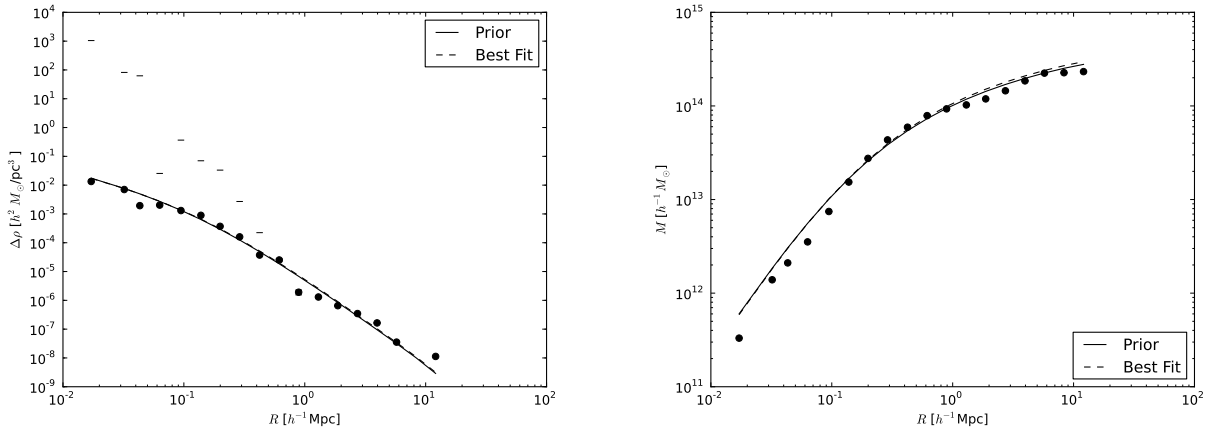

(c) $\Lambda : 27.5 - 29.1$

Figure 6.20: "Observed" and corrected (see Section 4.1) deprojected $\Delta\rho$ and M profiles for halos binned by richness.

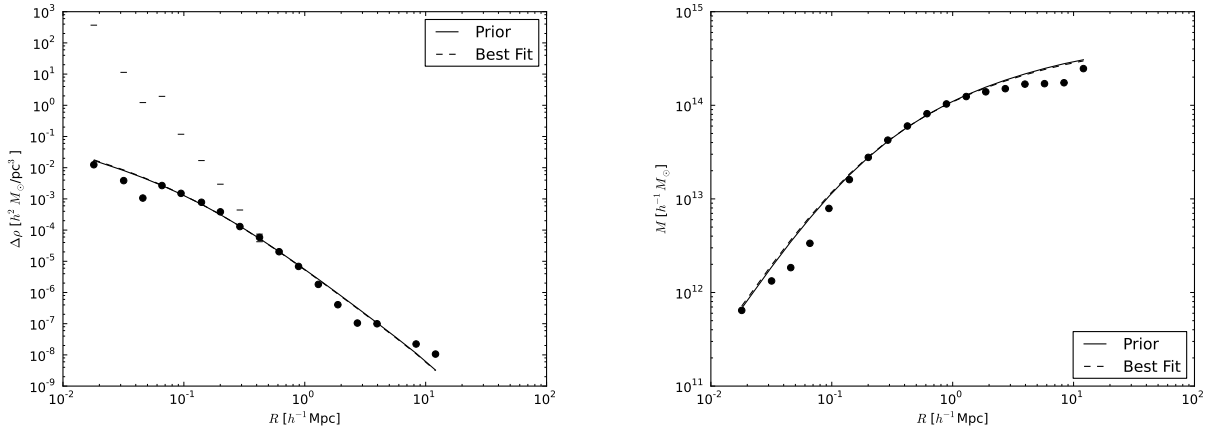

(a) $\Lambda : 29.1 - 33.8$

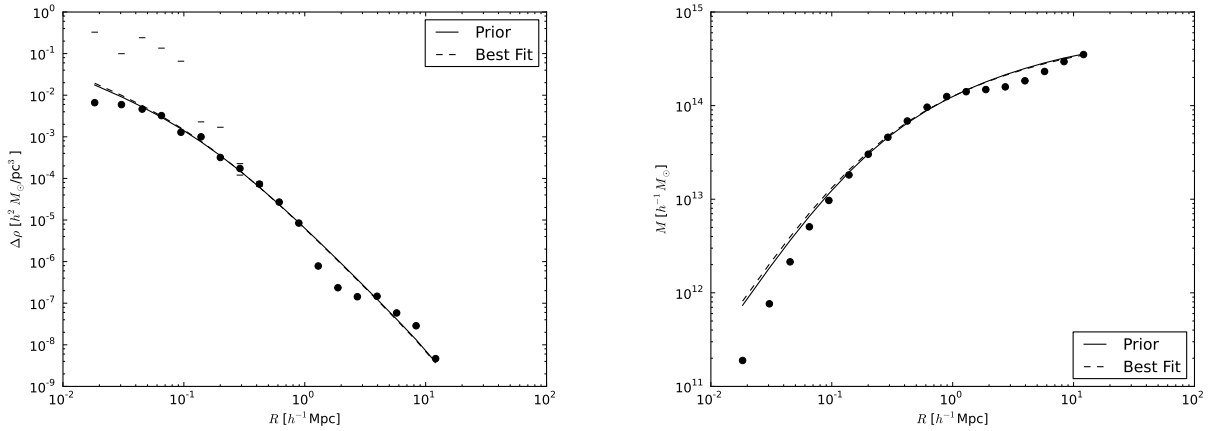

(b) $\Lambda : 33.8 - 43.2$

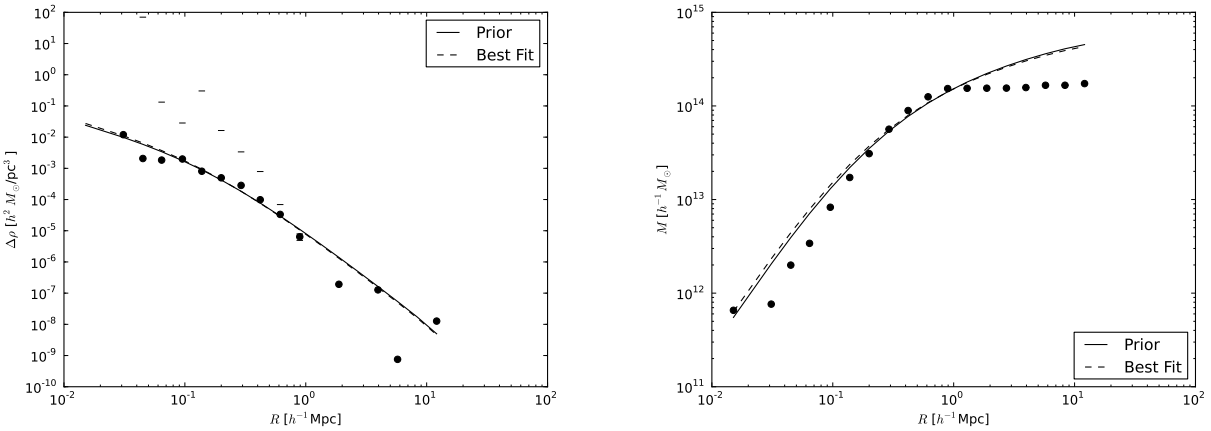

(c) $\Lambda : 43.2 - 55.8$

Figure 6.21: "Observed" and corrected (see Section 4.1) deprojected $\Delta\rho$ and M profiles for halos binned by richness.

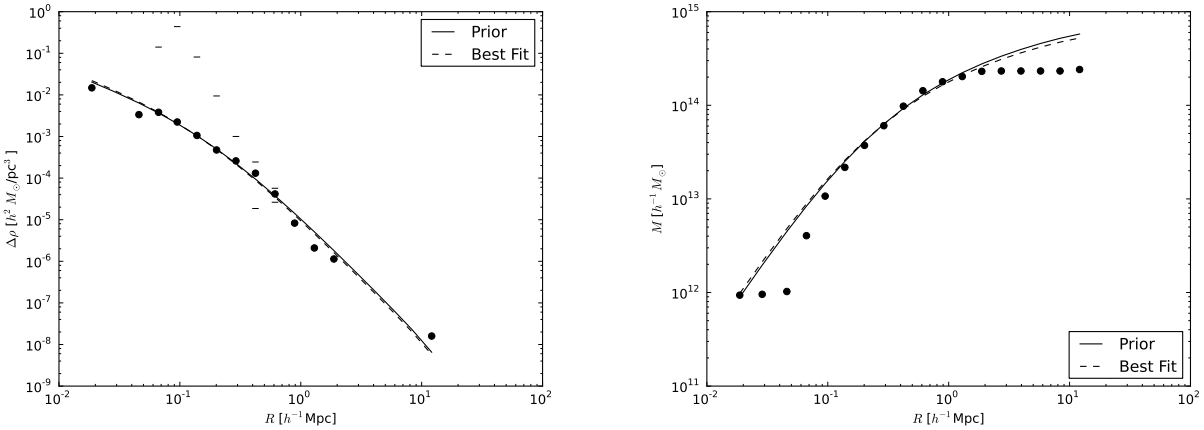

(a) $\Lambda : 55.8 - 79.3$

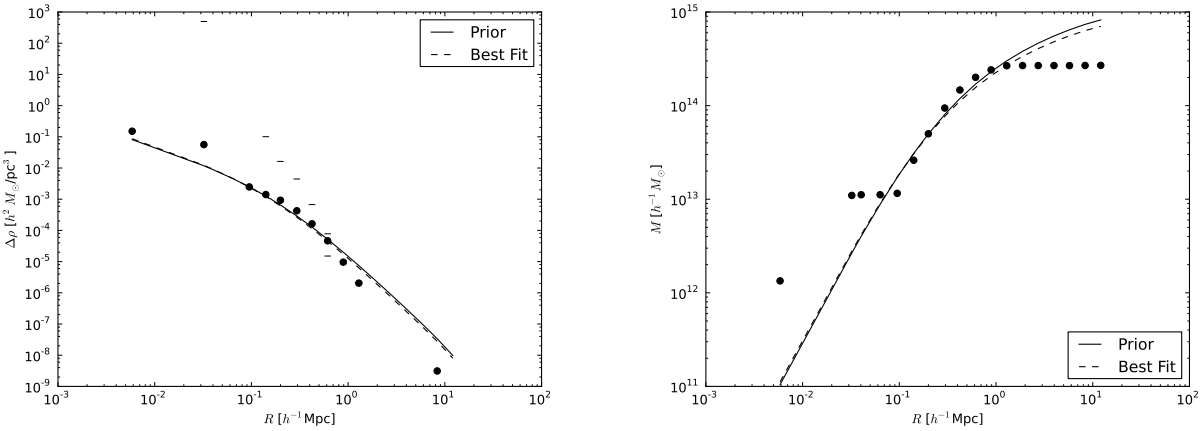

(b) $\Lambda : 79.3 - 126.3$

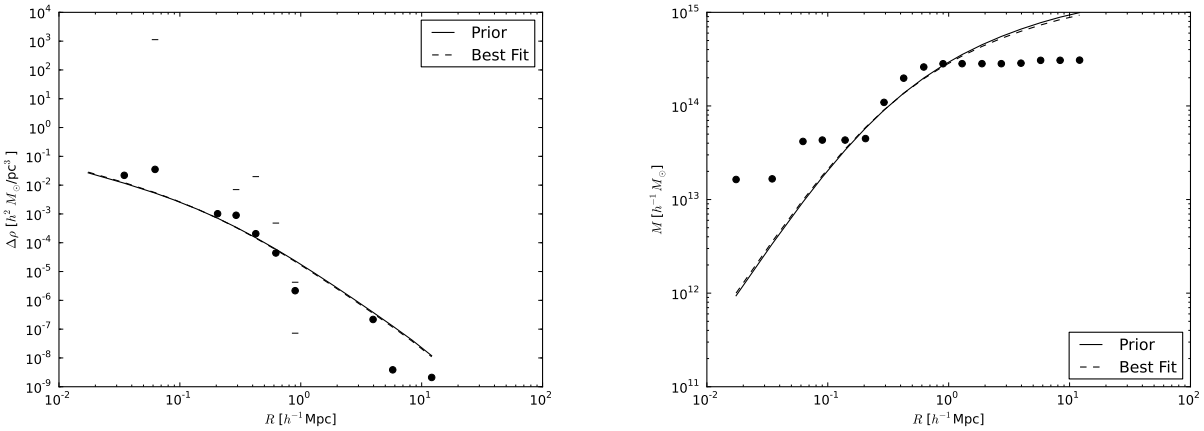

(c) $\Lambda : 126.3 - 361.6$

Figure 6.22: "Observed" and corrected (see Section 4.1) deprojected $\Delta\rho$ and M profiles for halos binned by richness.

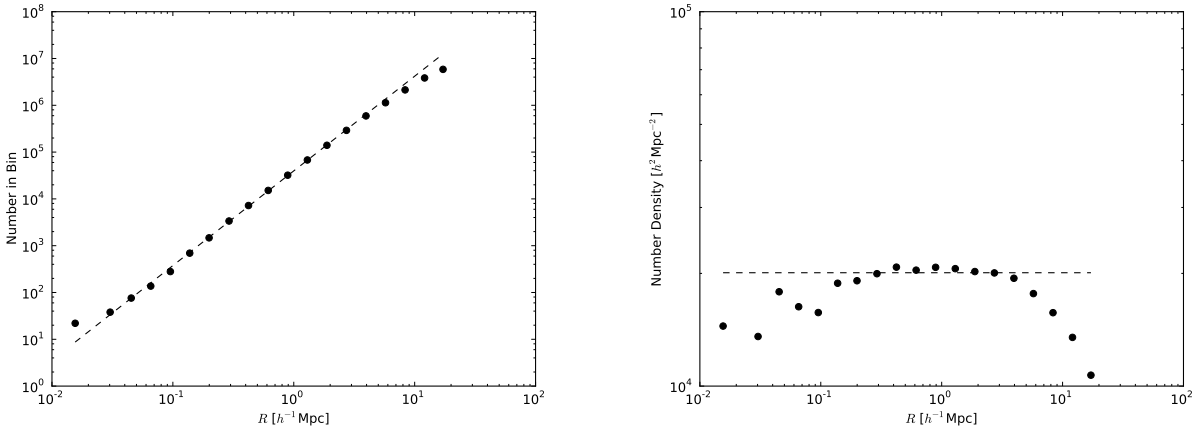

(a) $\Lambda : 19.7 - 21.3$

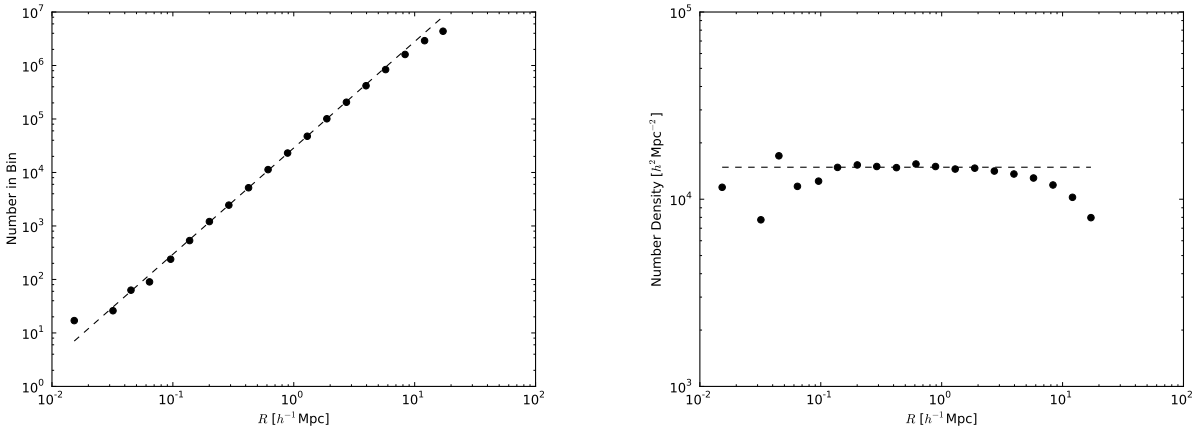

(b) $\Lambda : 21.3 - 22.8$

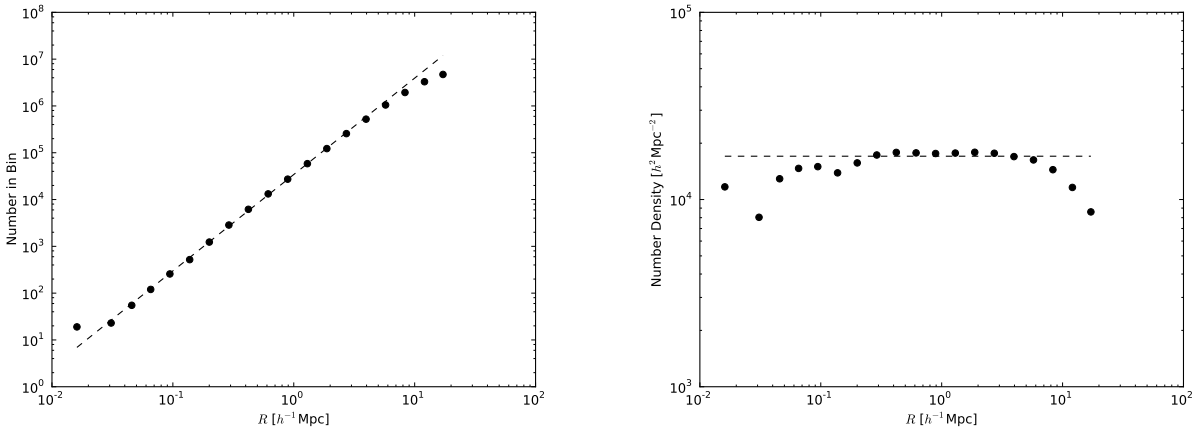

(c) $\Lambda : 22.8 - 24.4$

Figure 6.23: "Observed" and corrected (see Section 4.1) deprojected number and number density profiles for halos binned by richness.

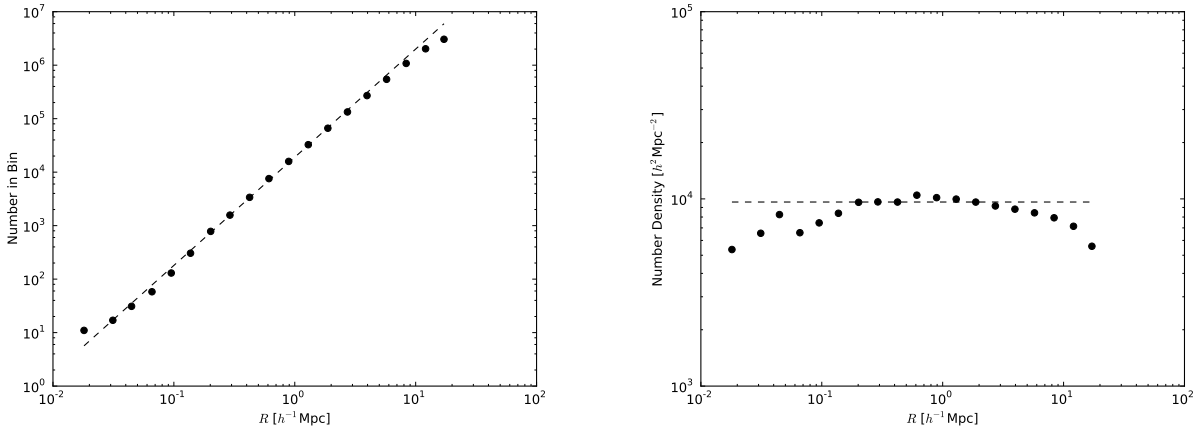

(a) $\Lambda : 24.4 - 26.0$

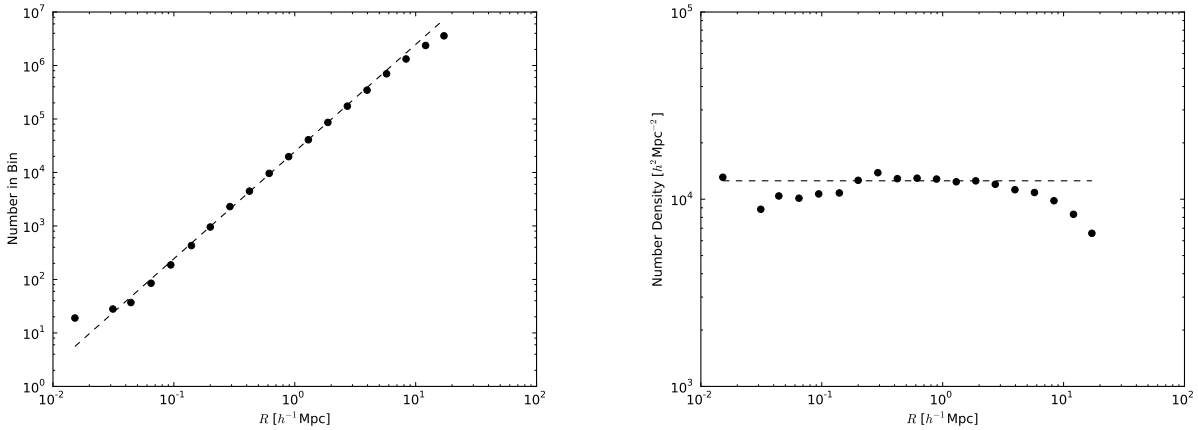

(b) $\Lambda : 26.0 - 27.5$

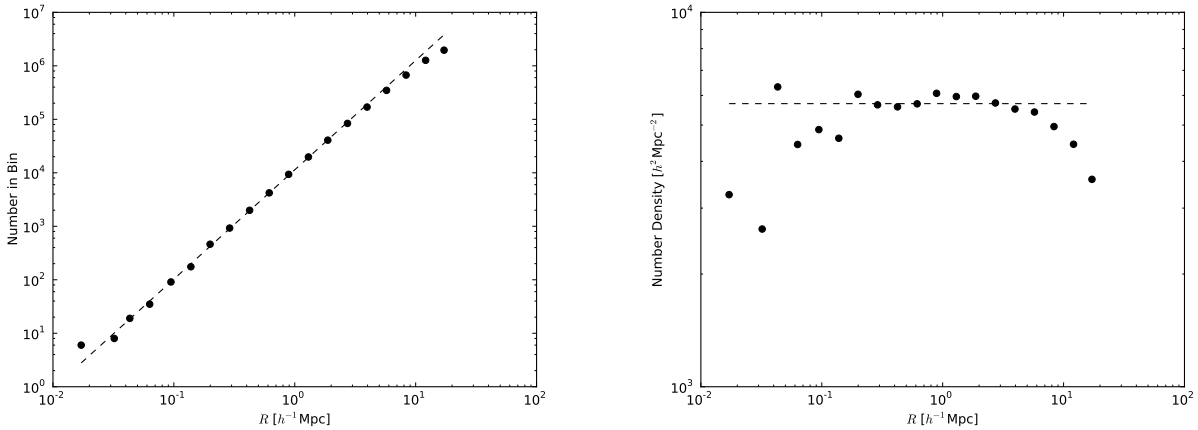

(c) $\Lambda : 27.5 - 29.1$

Figure 6.24: "Observed" and corrected (see Section 4.1) deprojected number and number density profiles for halos binned by richness.

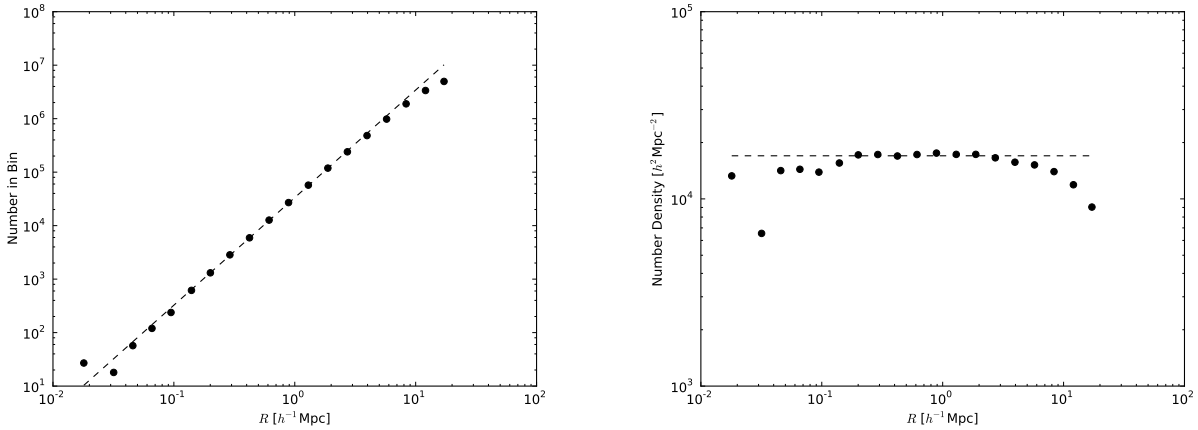

(a) $\Lambda : 29.1 - 33.8$

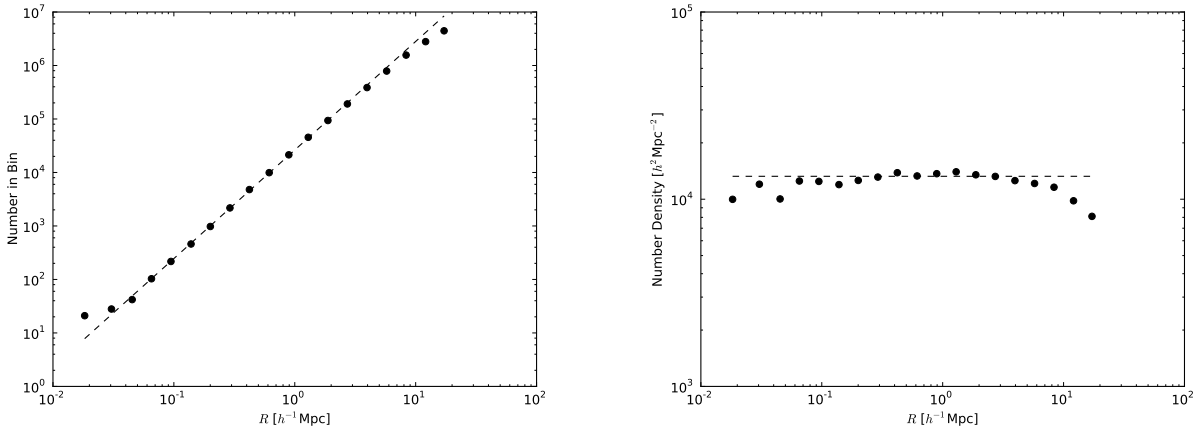

(b) $\Lambda : 33.8 - 43.2$

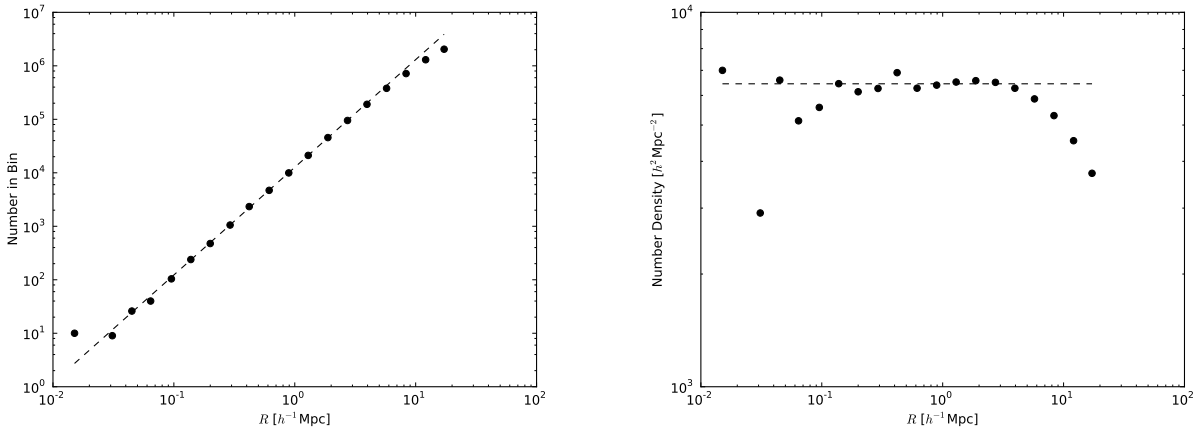

(c) $\Lambda : 43.2 - 55.8$

Figure 6.25: "Observed" and corrected (see Section 4.1) deprojected number and number density profiles for halos binned by richness.

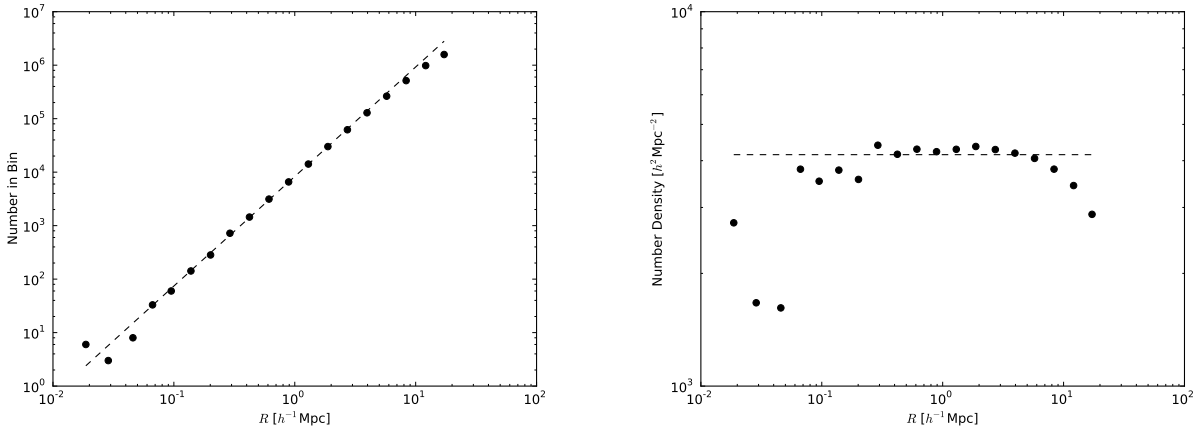

(a) $\Lambda : 55.8 - 79.3$

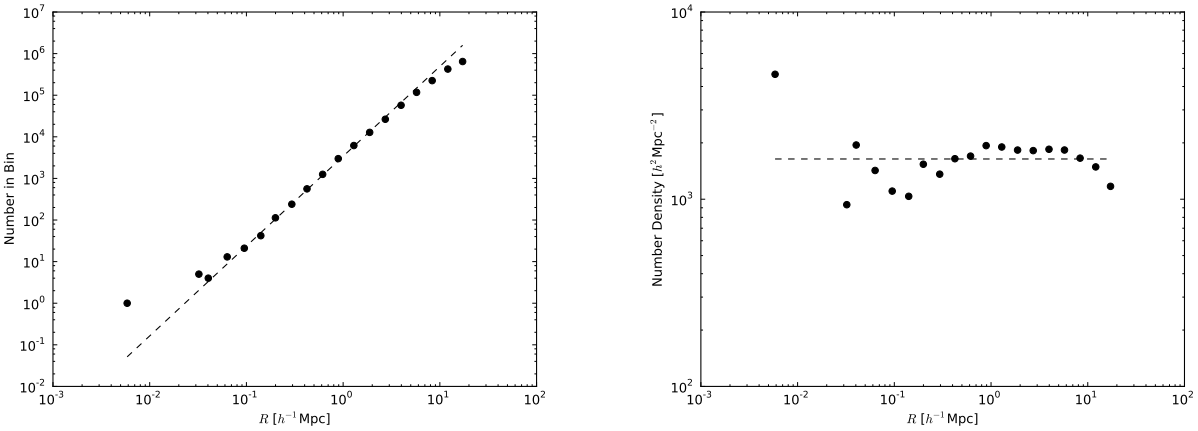

(b) $\Lambda : 79.3 - 126.3$

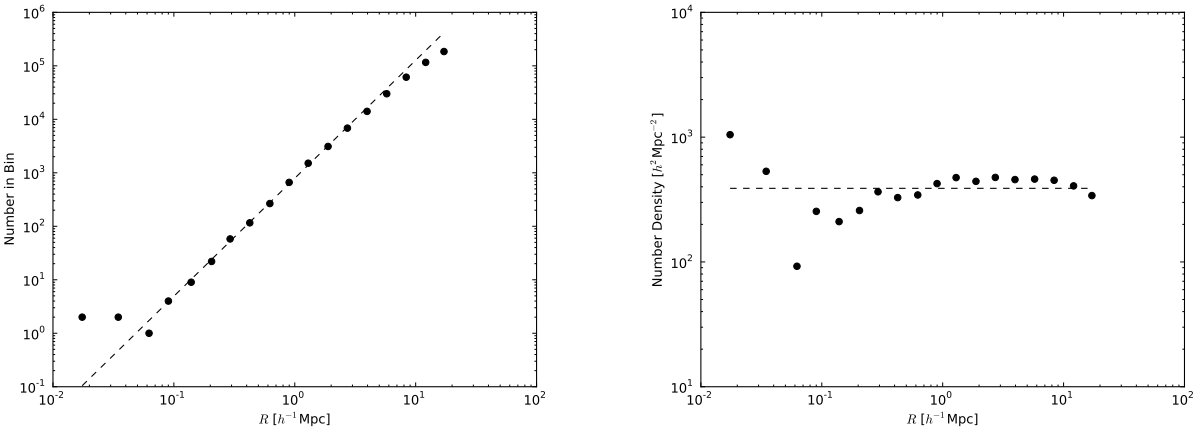

(c) $\Lambda : 126.3 - 361.6$

Figure 6.26: "Observed" and corrected (see Section 4.1) deprojected number and number density profiles for halos binned by richness.

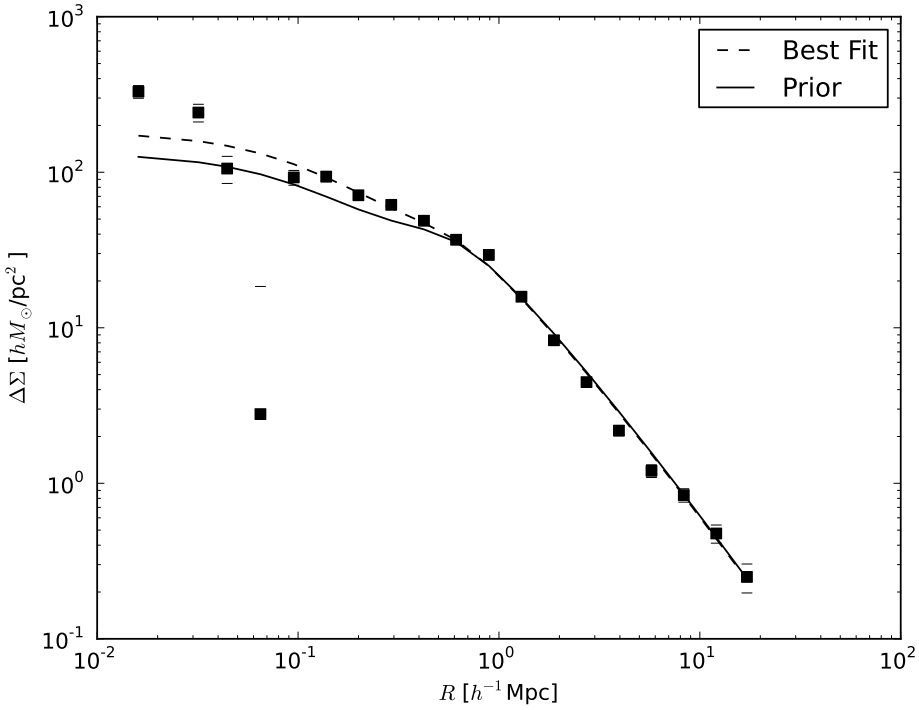

(a) $\Lambda : 19.7 - 21.3$

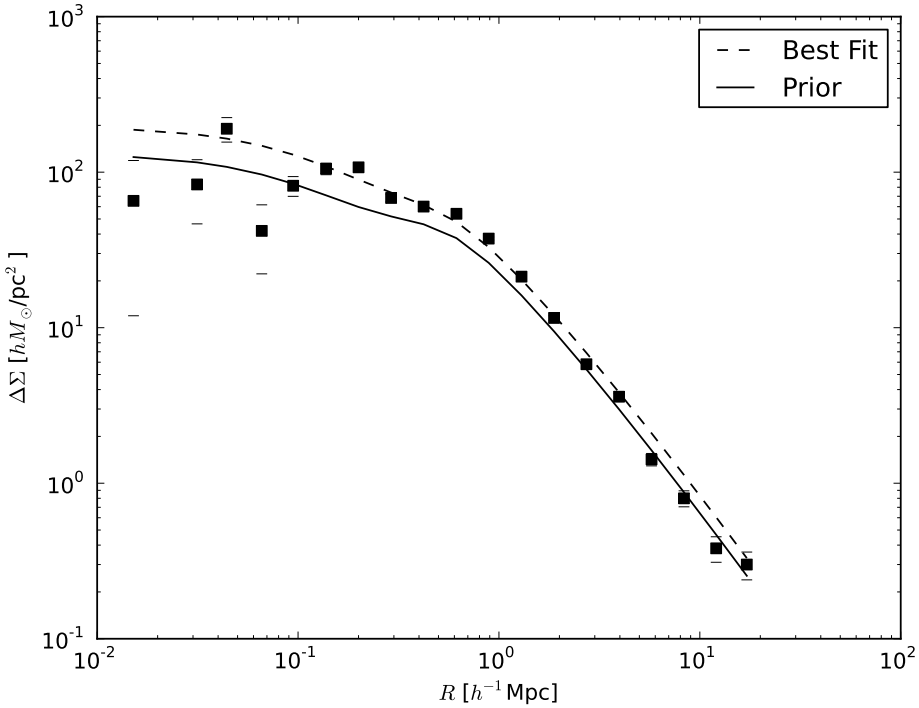

(b) $\Lambda : 21.3 - 22.8$

Figure 6.27: "Observed" $\Delta\Sigma$ profiles (see Section 4.1) for clusters binned by richness.

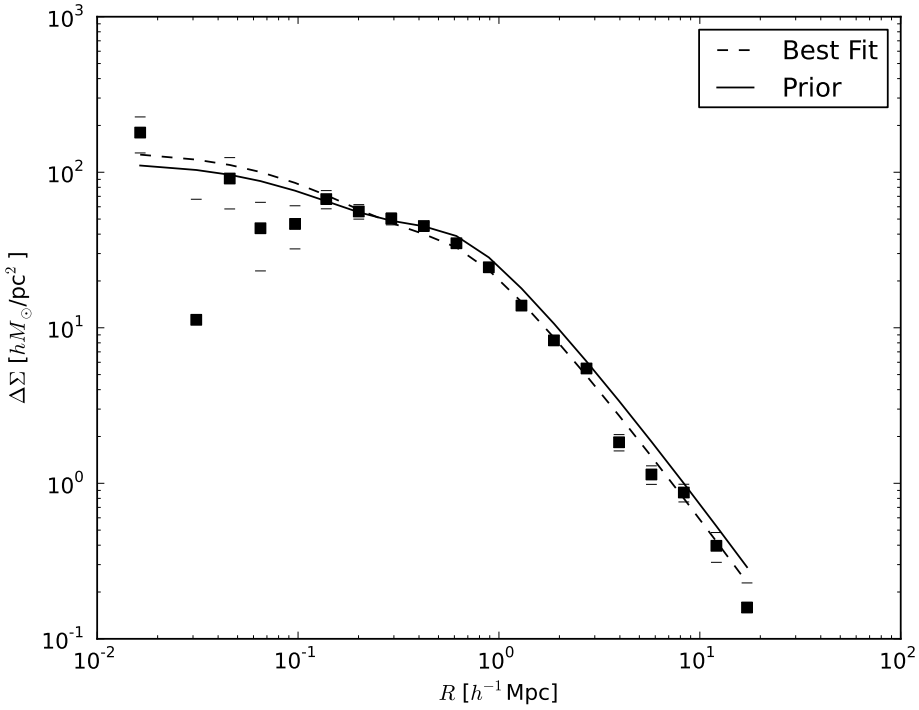

(a) $\Lambda : 22.8 - 24.4$

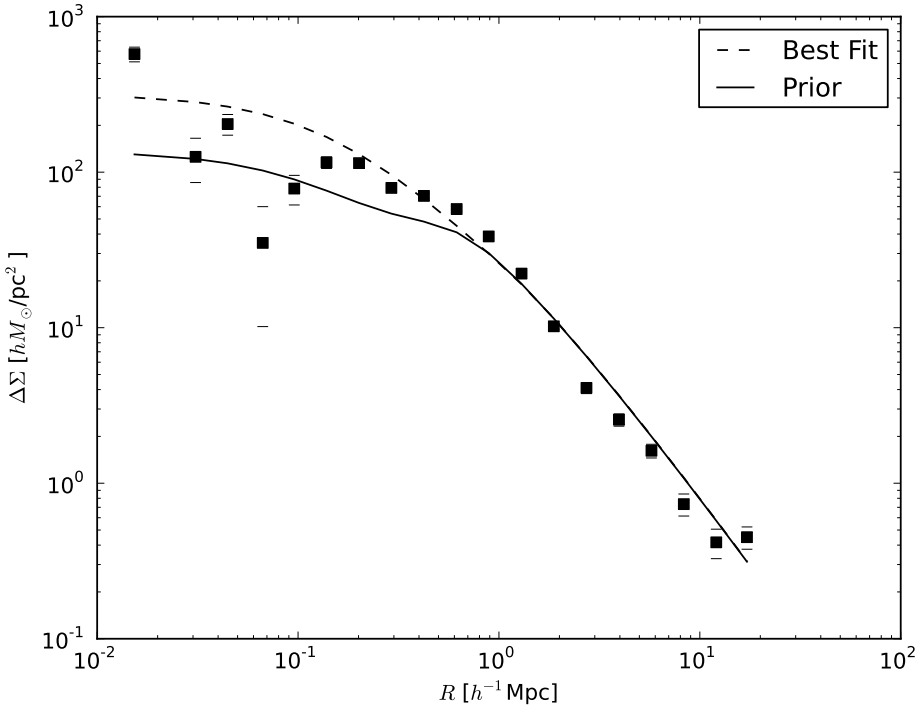

(b) $\Lambda : 24.4 - 26.0$

Figure 6.28: "Observed" $\Delta\Sigma$ profiles (see Section 4.1) for clusters binned by richness.

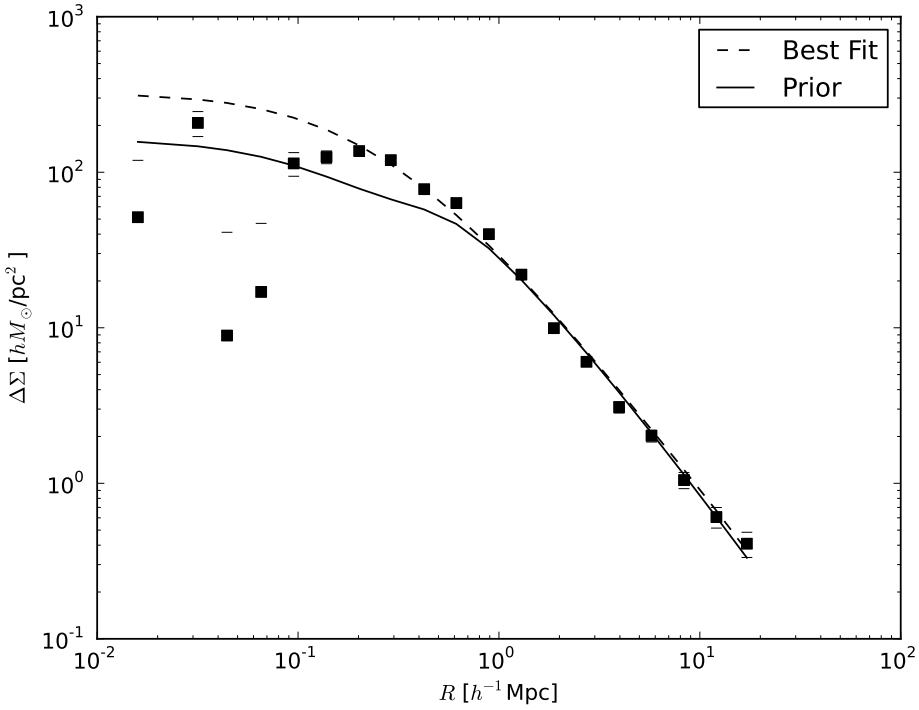

(a) $\Lambda : 26.0 - 27.5$

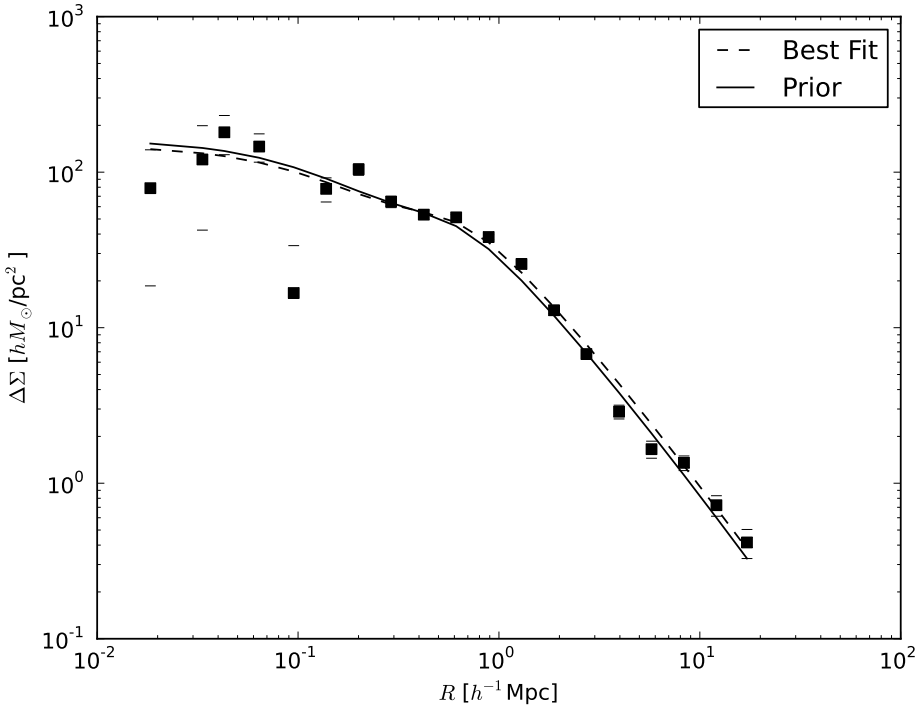

(b) $\Lambda : 27.5 - 29.1$

Figure 6.29: "Observed" $\Delta\Sigma$ profiles (see Section 4.1) for clusters binned by richness.

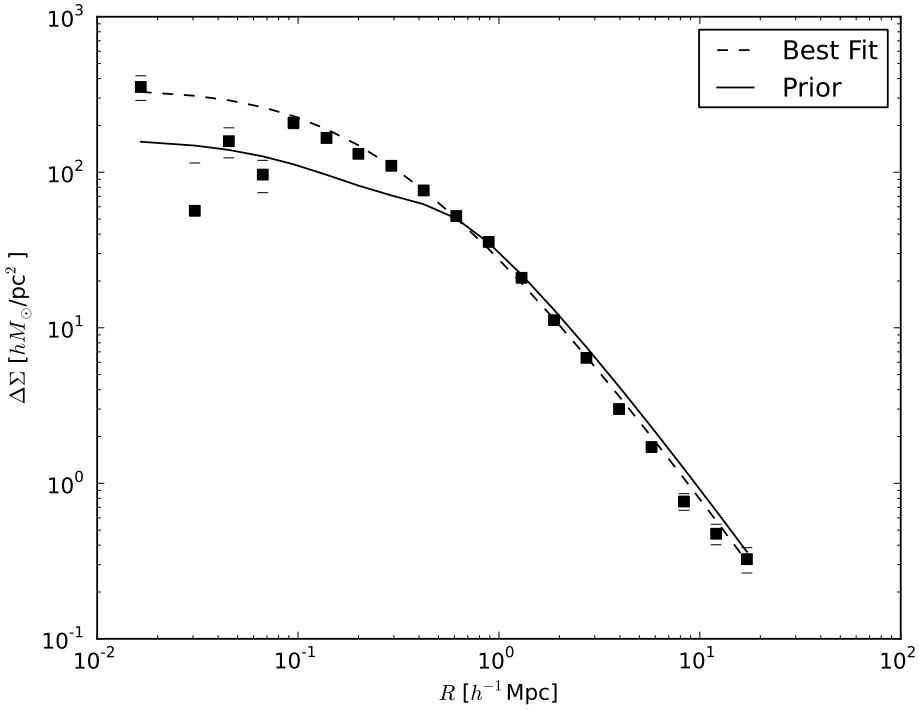

(a) $\Lambda : 29.1 - 33.8$

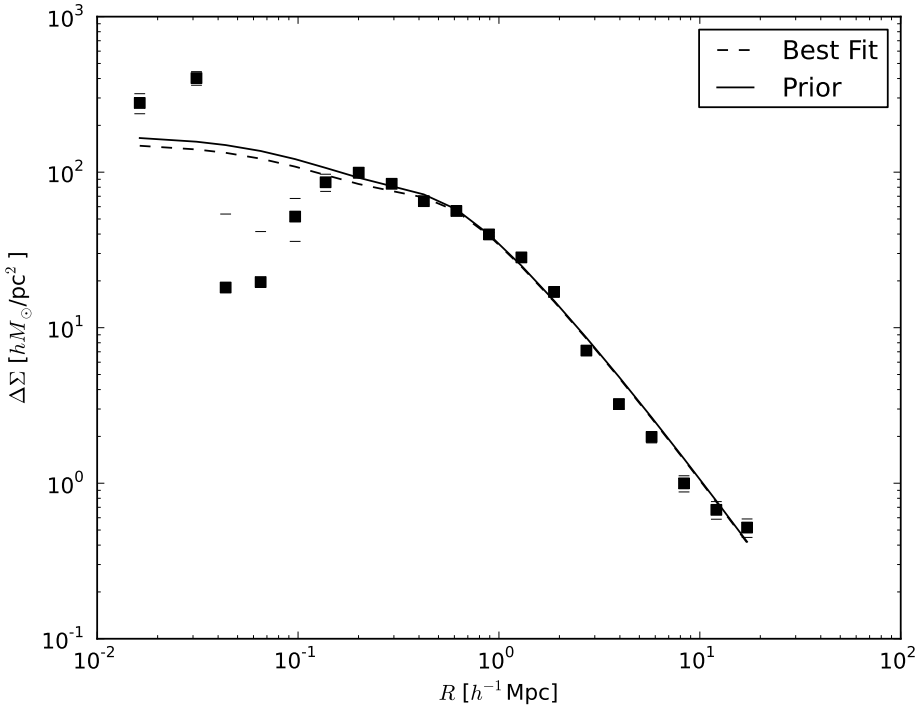

(b) $\Lambda : 33.8 - 43.2$

Figure 6.30: "Observed" $\Delta\Sigma$ profiles (see Section 4.1) for clusters binned by richness.

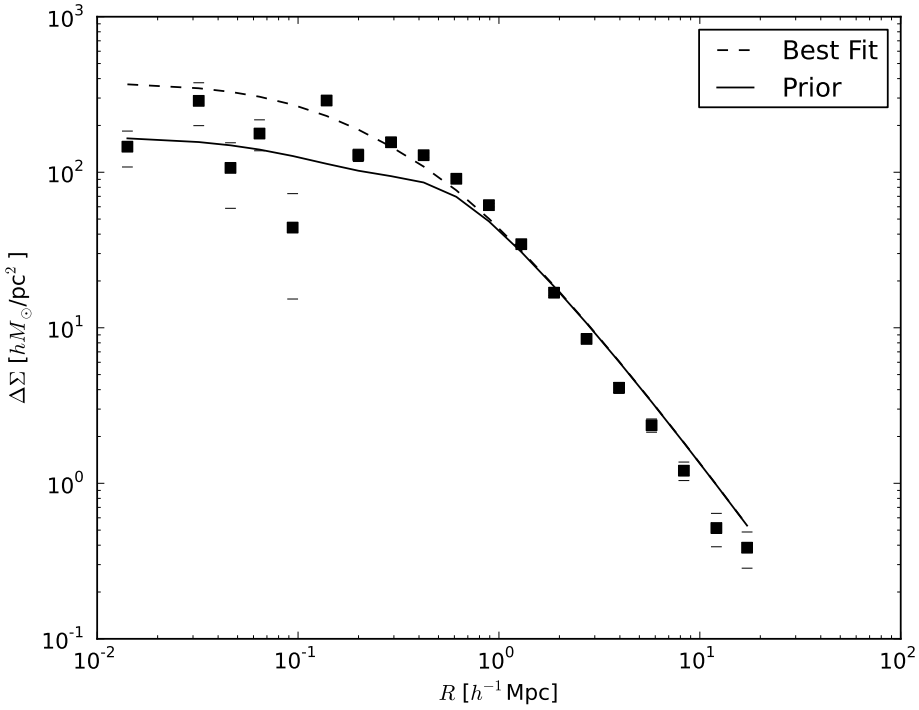

(a) $\Lambda : 43.2 - 55.8$

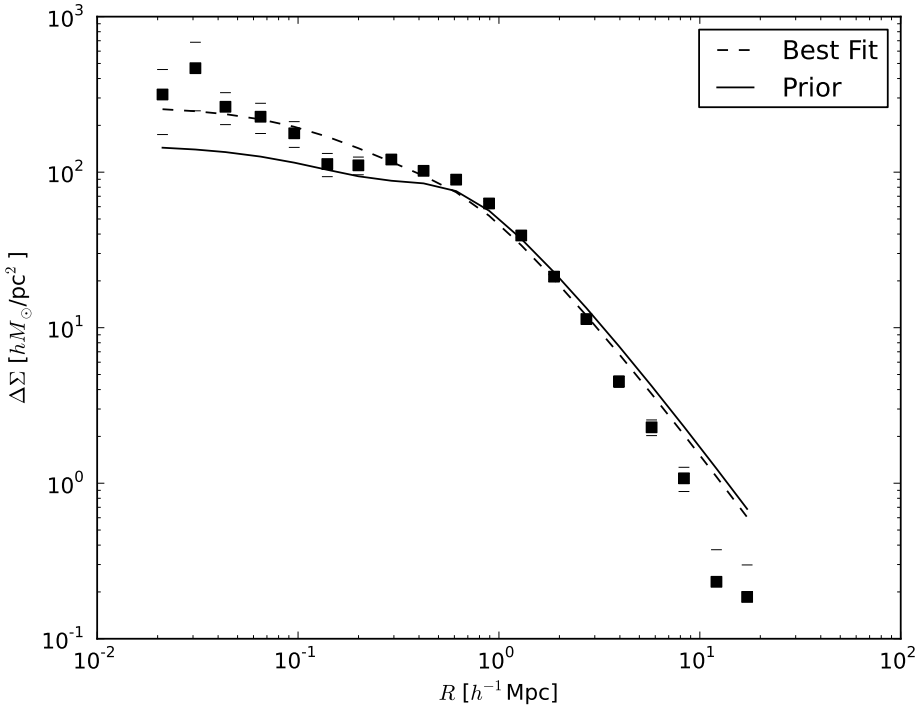

(b) $\Lambda : 55.8 - 79.3$

Figure 6.31: "Observed" $\Delta\Sigma$ profiles (see Section 4.1) for clusters binned by richness.

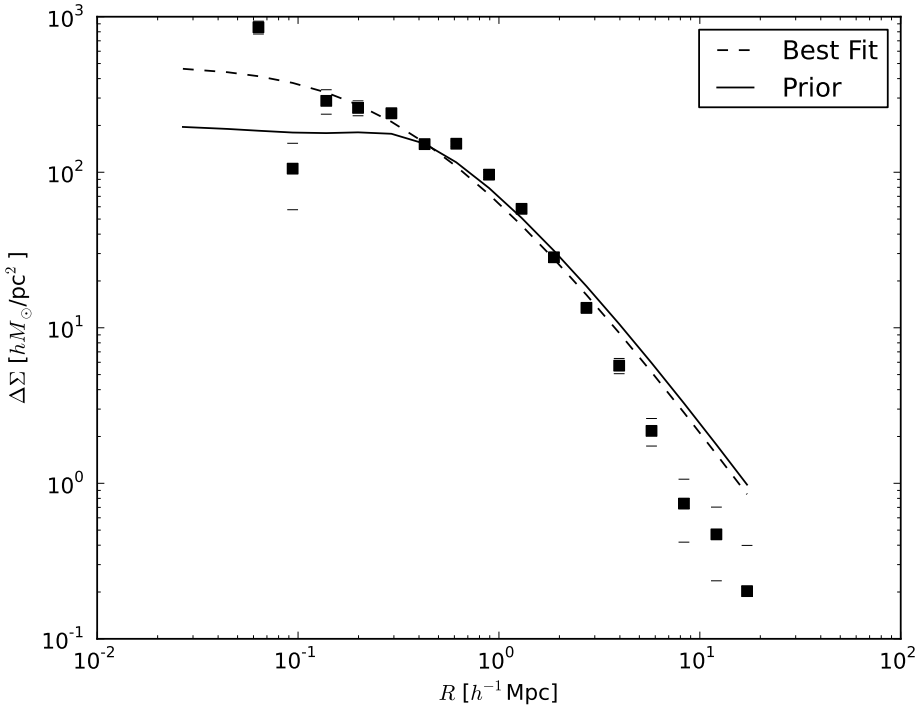

(a) $\Lambda : 79.3 - 126.3$

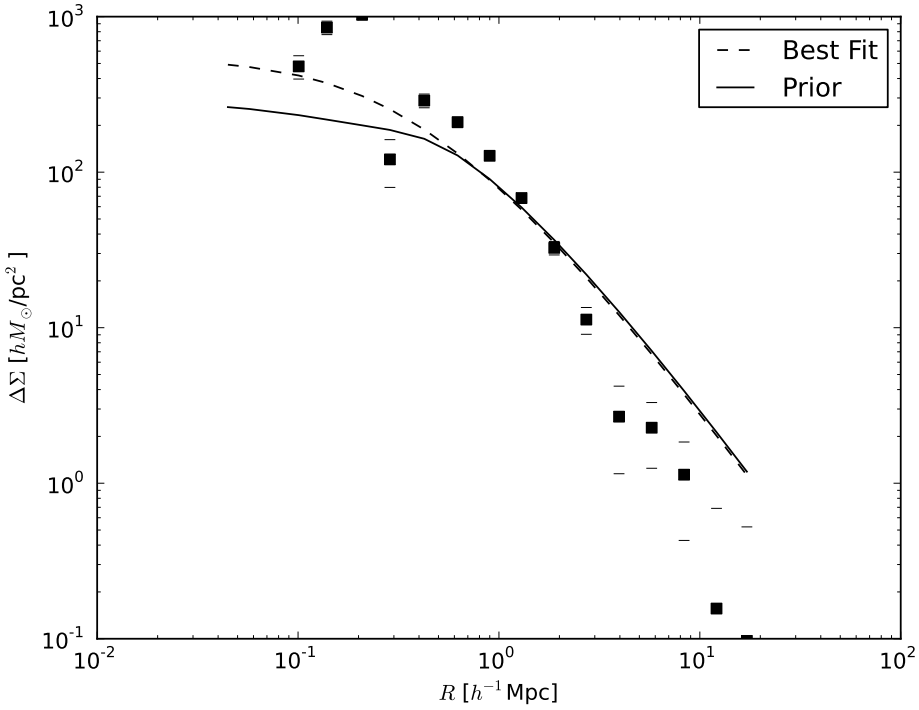

(b) $\Lambda : 126.3 - 361.6$

Figure 6.32: "Observed" $\Delta\Sigma$ profiles (see Section 4.1) for clusters binned by richness.

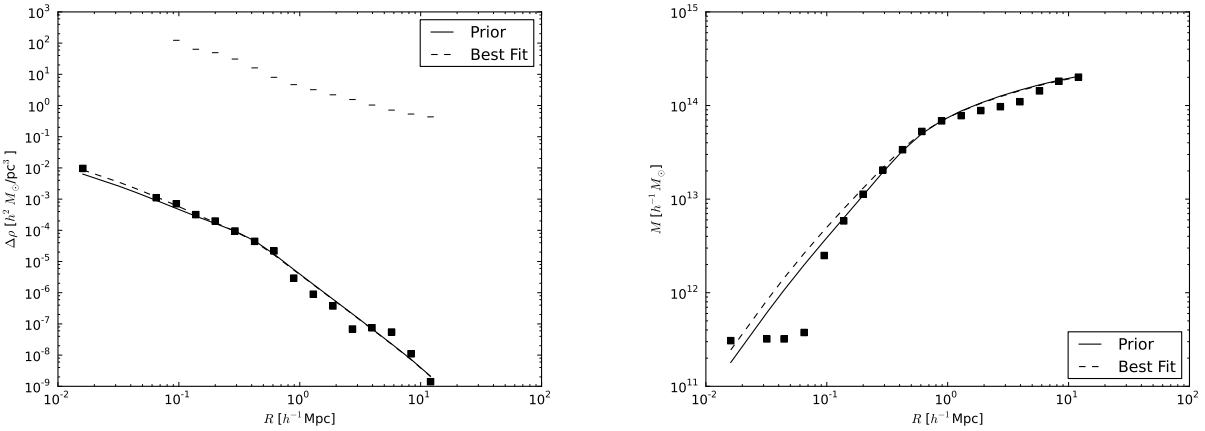

(a) $\Lambda : 19.7 - 21.3$

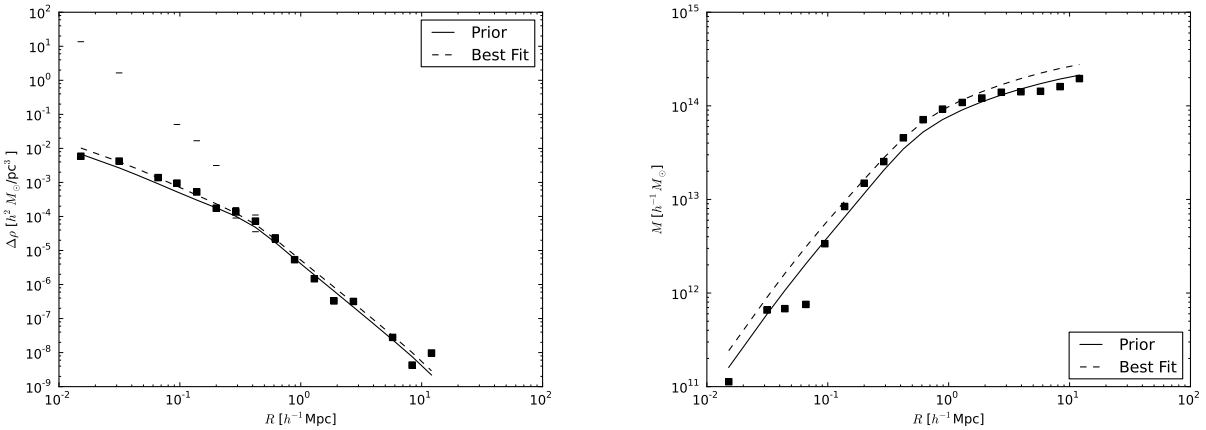

(b) $\Lambda : 21.3 - 22.8$

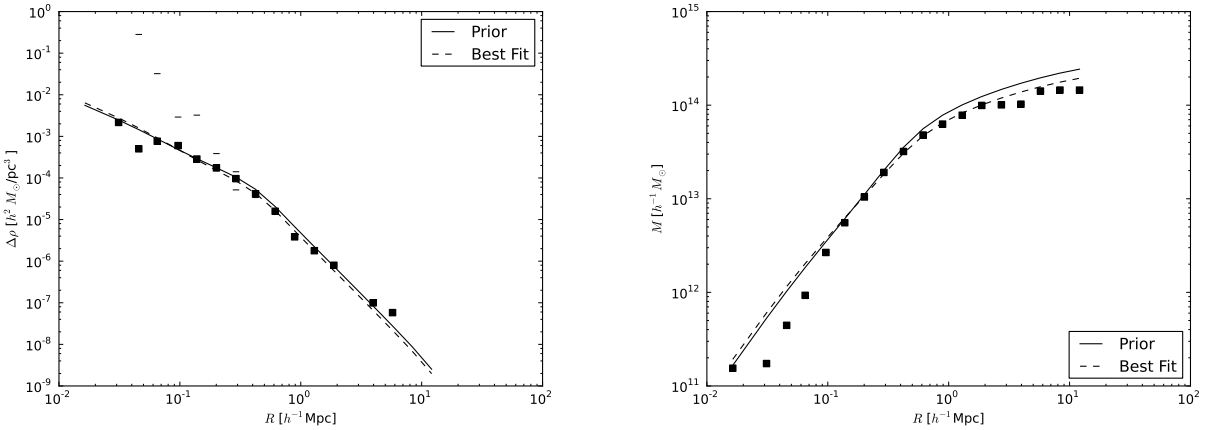

(c) $\Lambda : 22.8 - 24.4$

Figure 6.33: "Observed" deprojected $\Delta\rho$ and M profiles for clusters binned by richness.

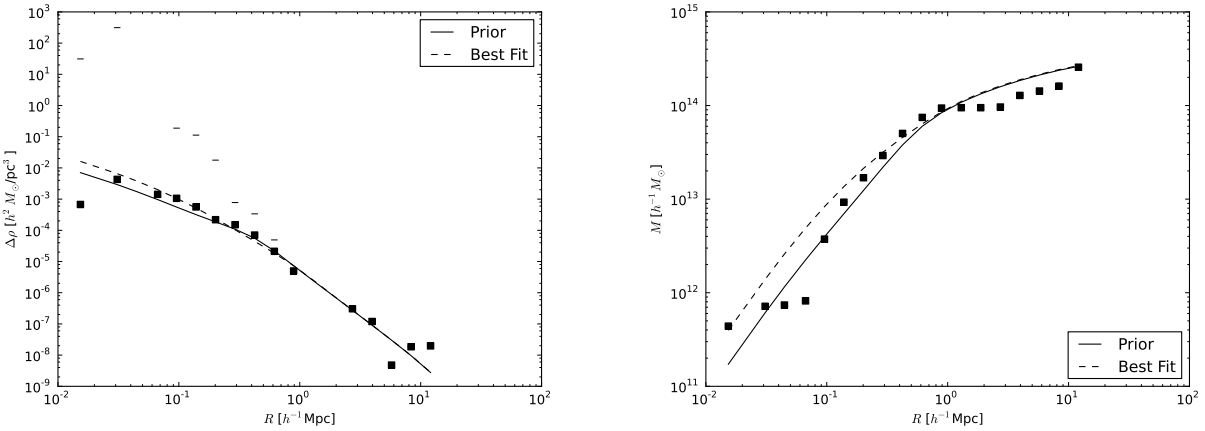

(a) $\Lambda : 24.4 - 26.0$

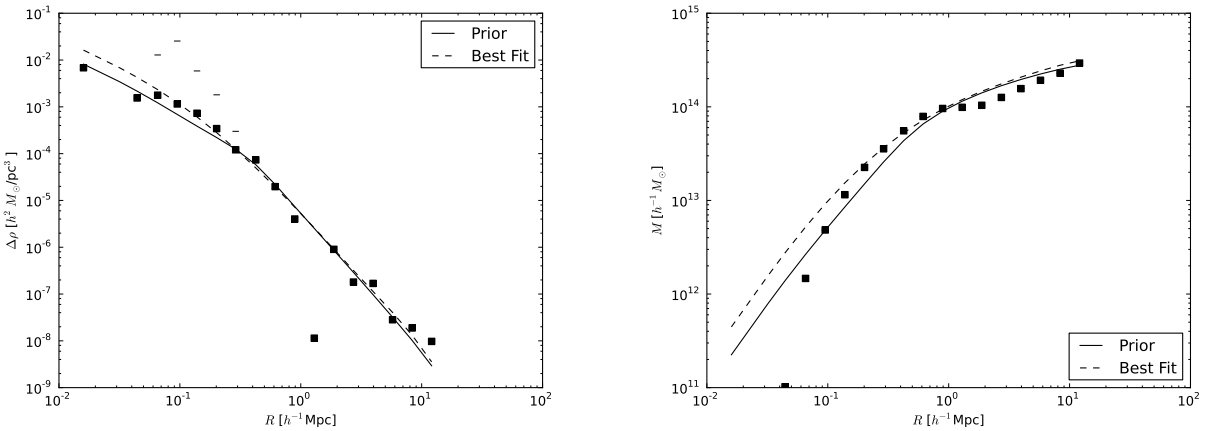

(b) $\Lambda : 26.0 - 27.5$

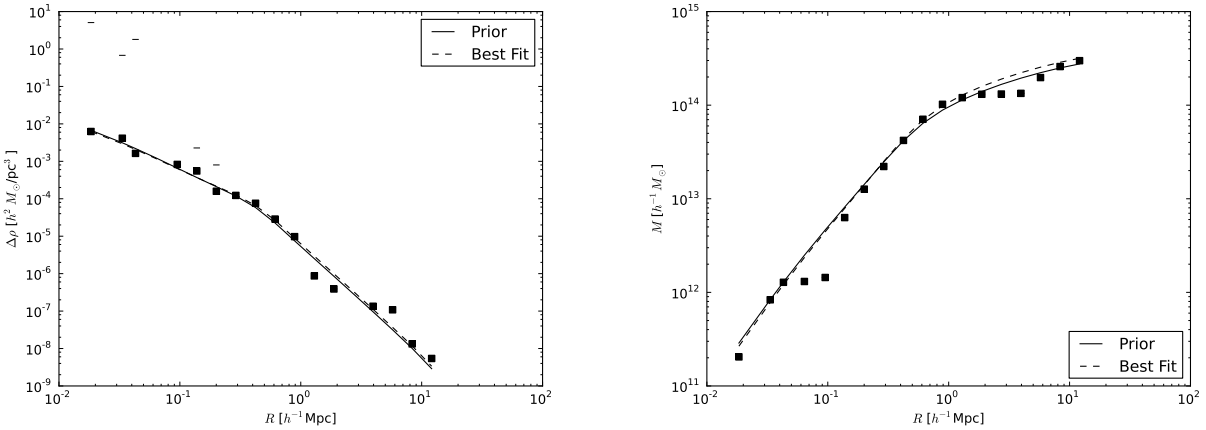

(c) $\Lambda : 27.5 - 29.1$

Figure 6.34: "Observed" deprojected $\Delta\rho$ and M profiles for clusters binned by richness.

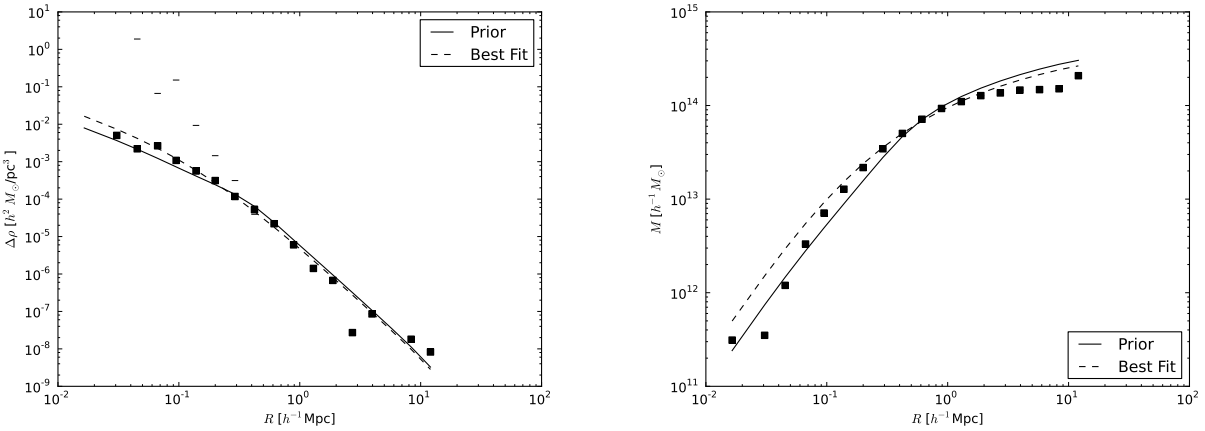

(a) $\Lambda : 29.1 - 33.8$

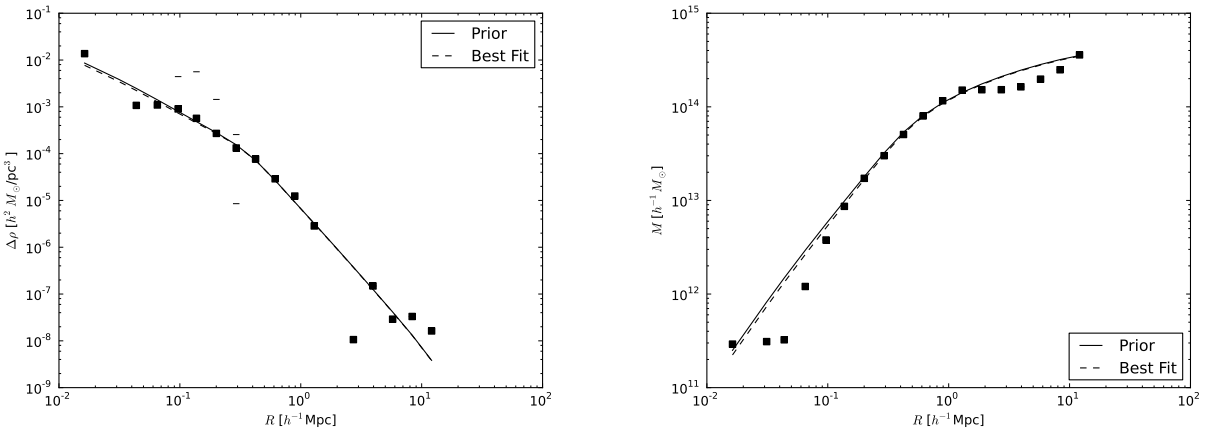

(b) $\Lambda : 33.8 - 43.2$

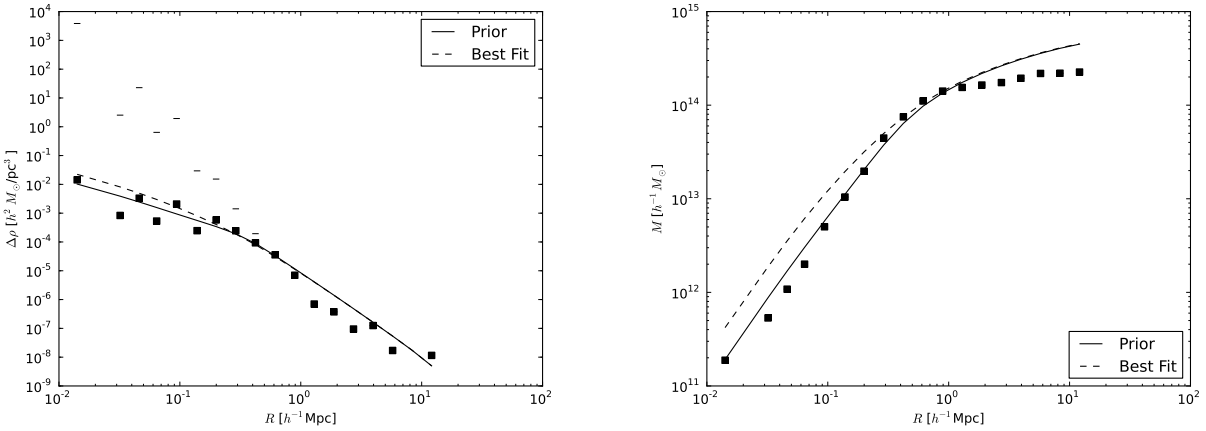

(c) $\Lambda : 43.2 - 55.8$

Figure 6.35: "Observed" deprojected $\Delta\rho$ and M profiles for clusters binned by richness.

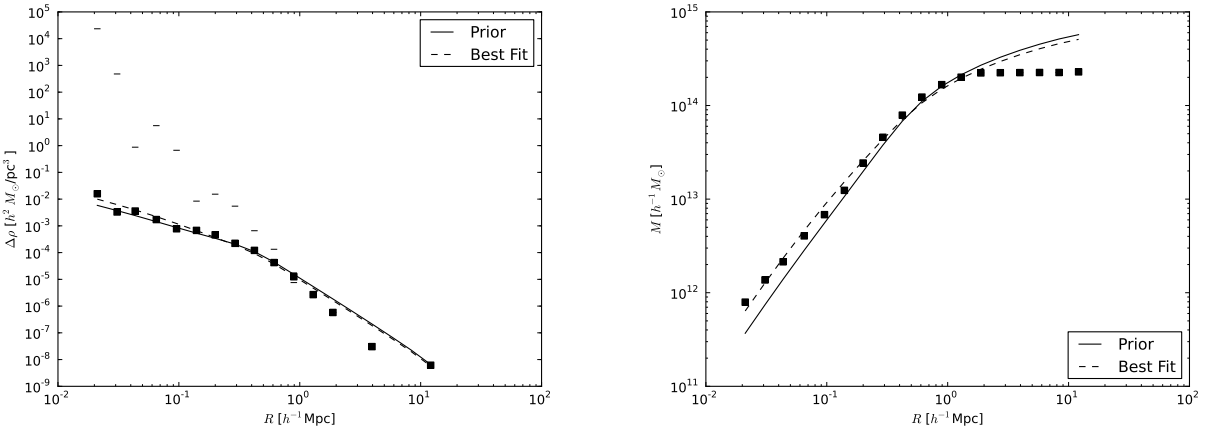

(a) $\Lambda : 55.8 - 79.3$

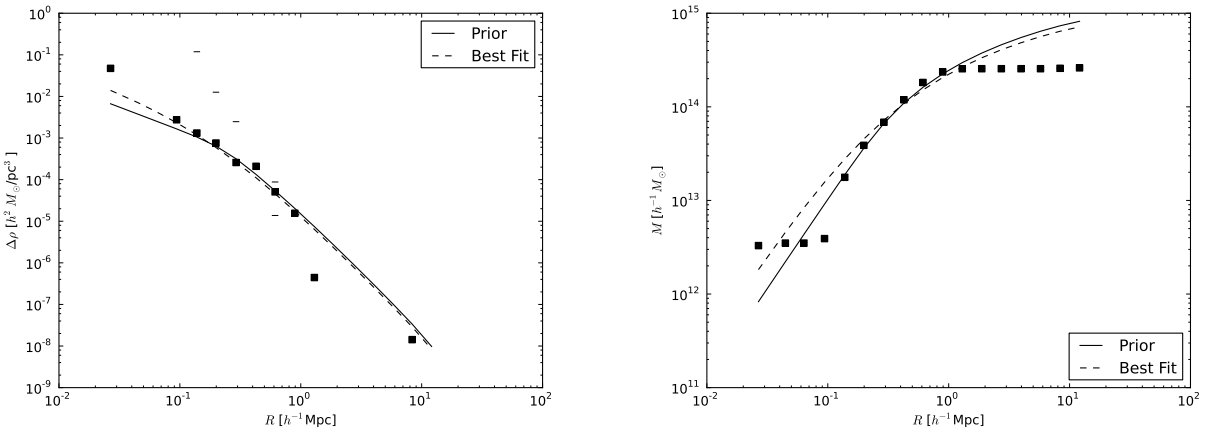

(b) $\Lambda : 79.3 - 126.3$

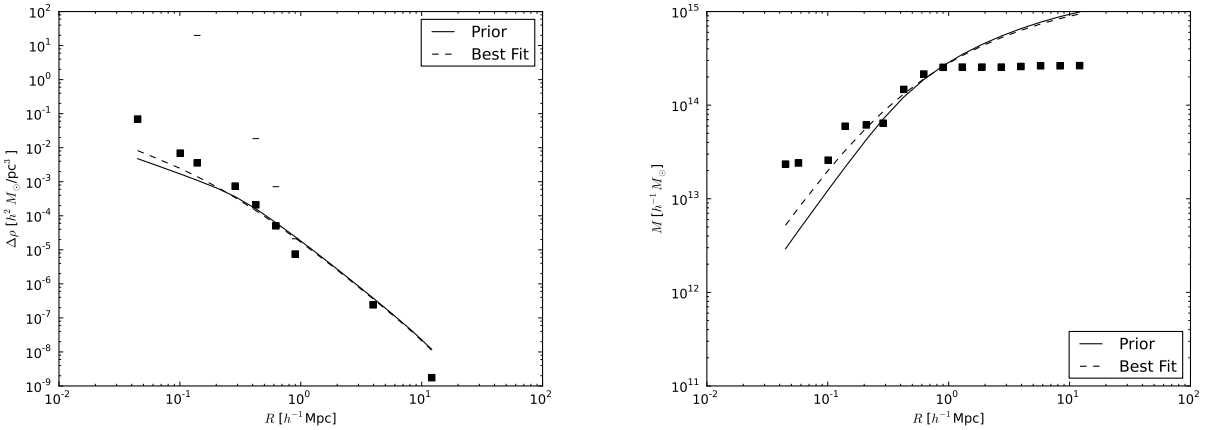

(c) $\Lambda : 126.3 - 361.6$

Figure 6.36: "Observed" deprojected $\Delta\rho$ and M profiles for clusters binned by richness.

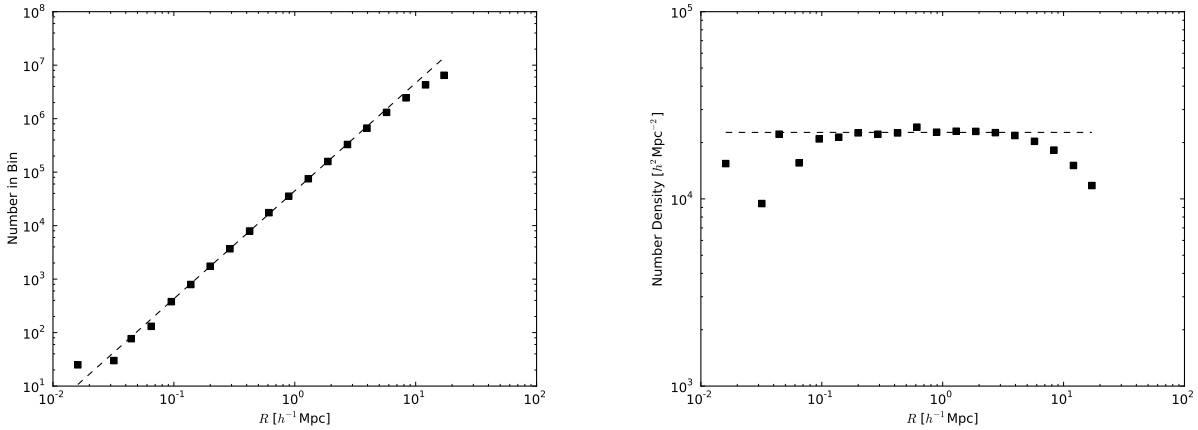

(a) $\Lambda : 19.7 - 21.3$

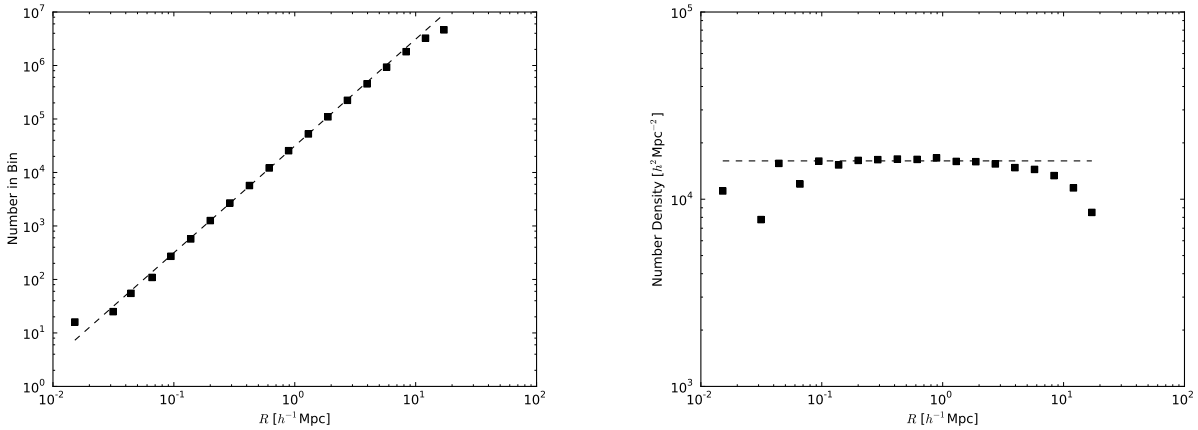

(b) $\Lambda : 21.3 - 22.8$

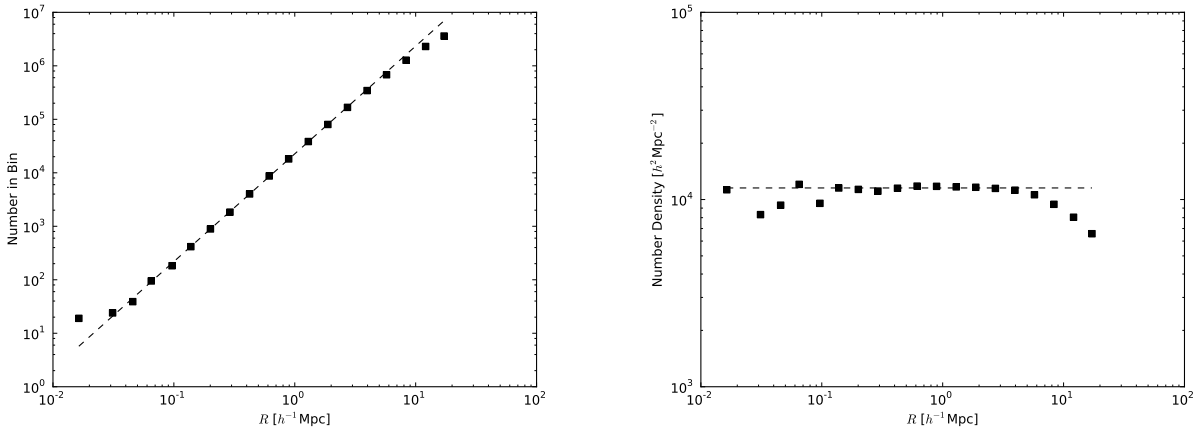

(c) $\Lambda : 22.8 - 24.4$

Figure 6.37: "Observed" deprojected number and number density profiles for clusters binned by richness.

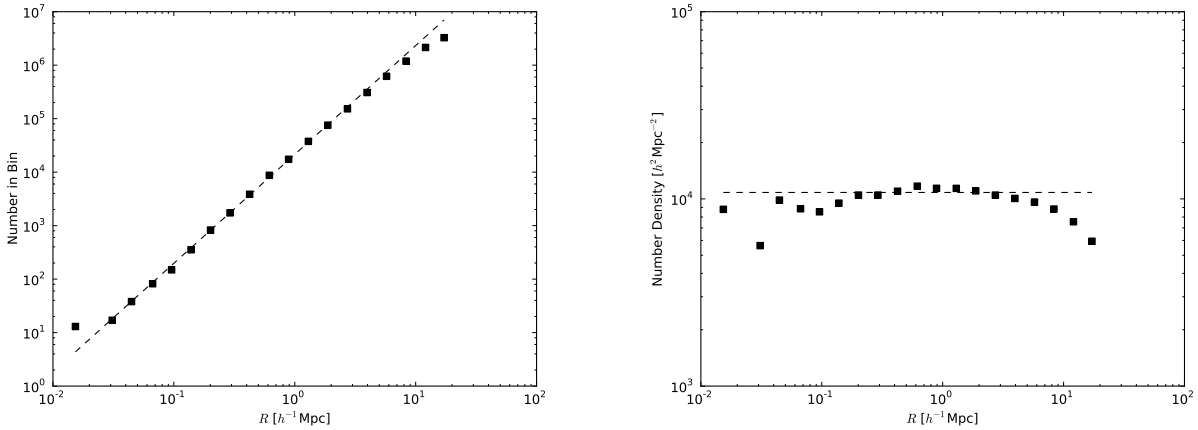

(a) $\Lambda : 24.4 - 26.0$

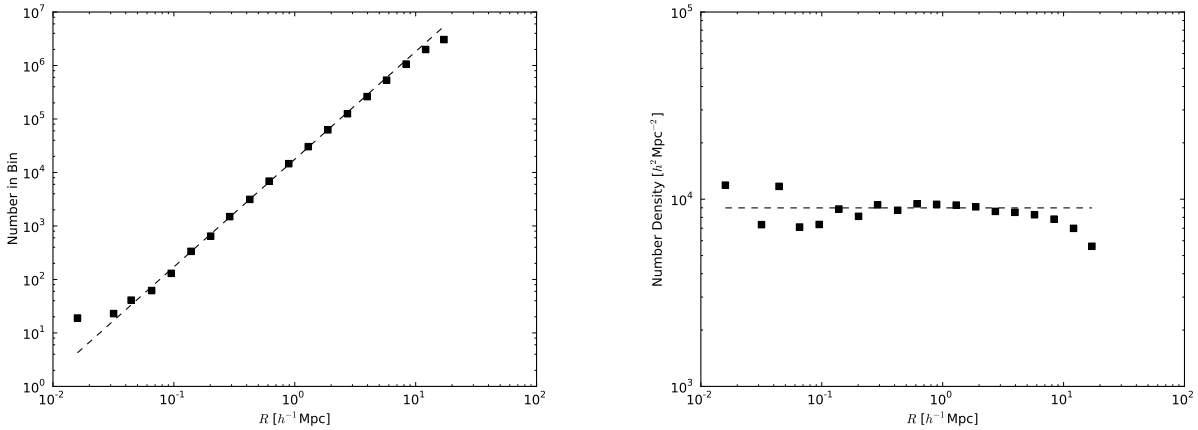

(b) $\Lambda : 26.0 - 27.5$

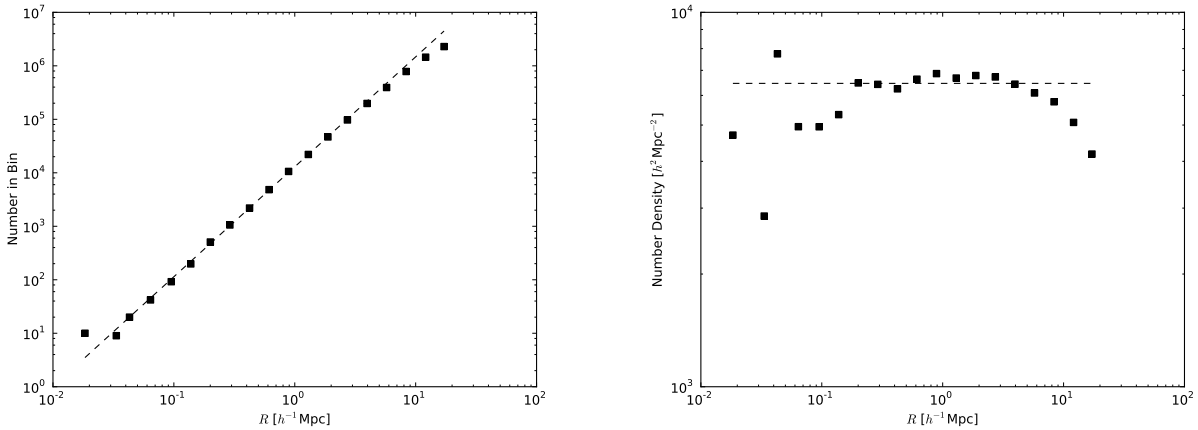

(c) $\Lambda : 27.5 - 29.1$

Figure 6.38: "Observed" deprojected number and number density profiles for clusters binned by richness.

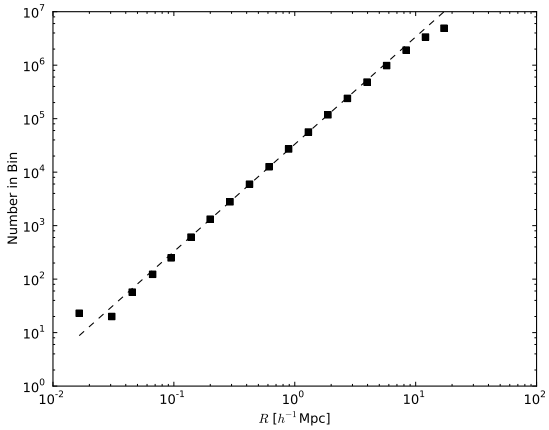

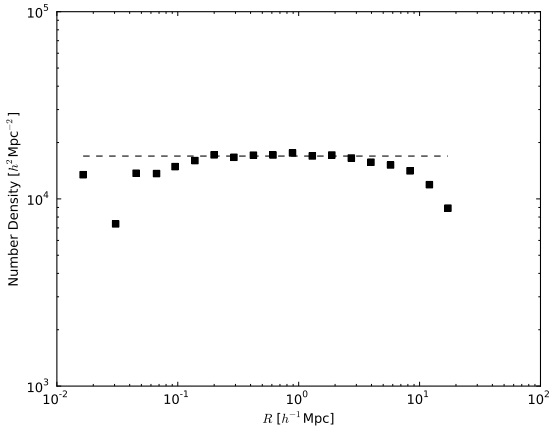

(a) $\Lambda : 29.1 - 33.8$

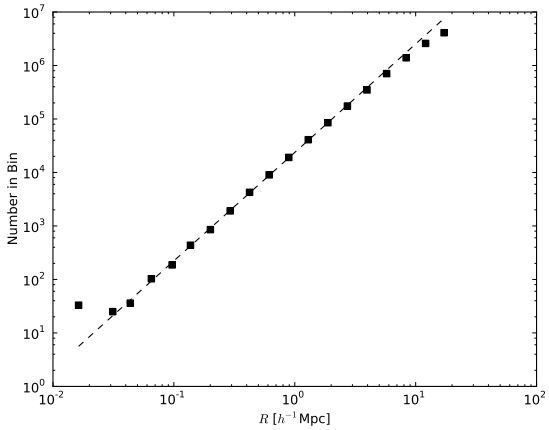

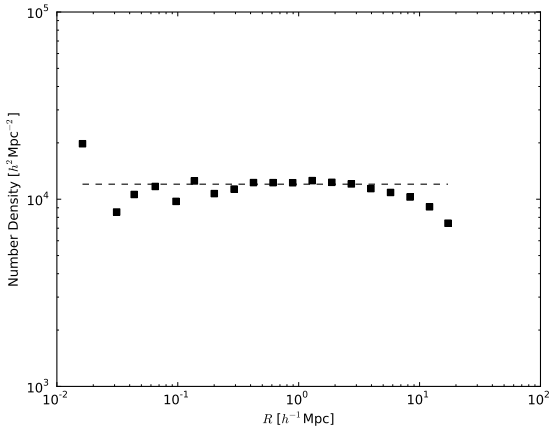

(b) $\Lambda : 33.8 - 43.2$

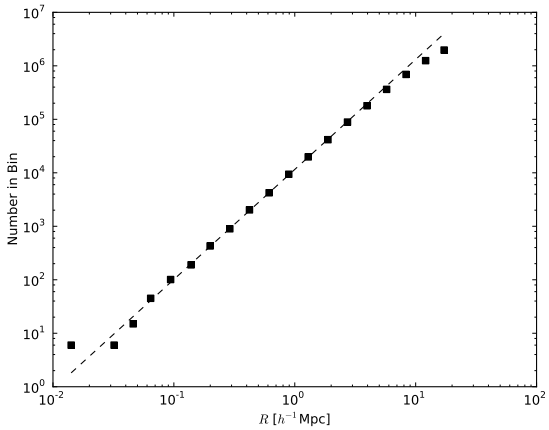

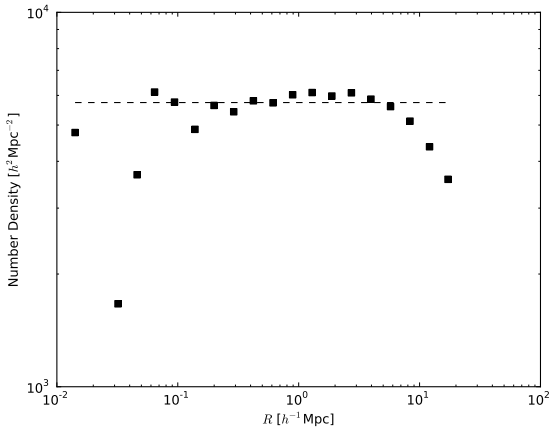

(c) $\Lambda : 43.2 - 55.8$

Figure 6.39: "Observed" deprojected number and number density profiles for clusters binned by richness.

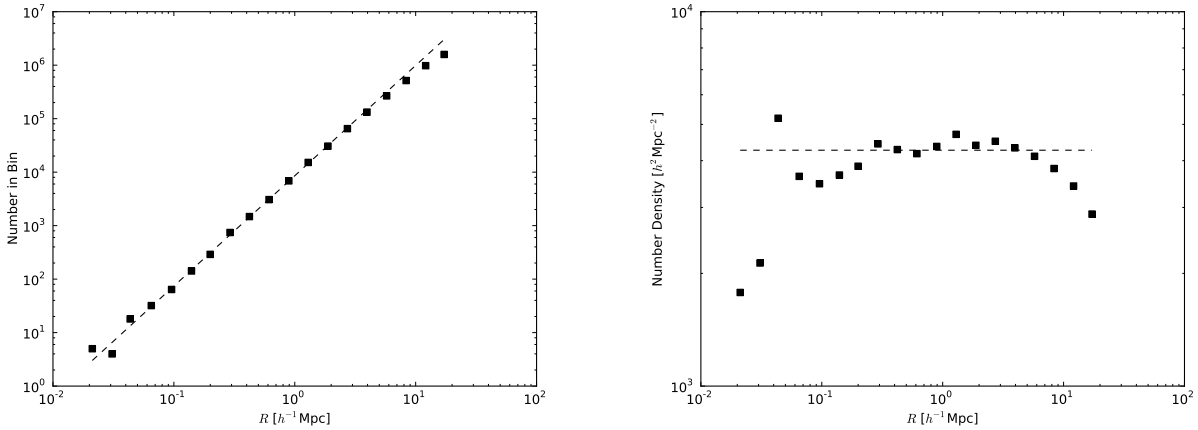

(a) $\Lambda : 55.8 - 79.3$

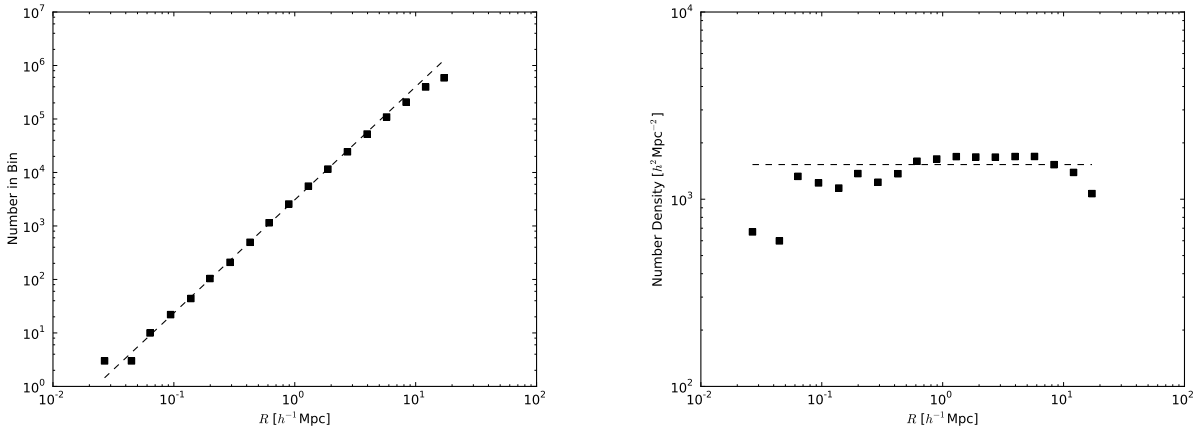

(b) $\Lambda : 79.3 - 126.3$

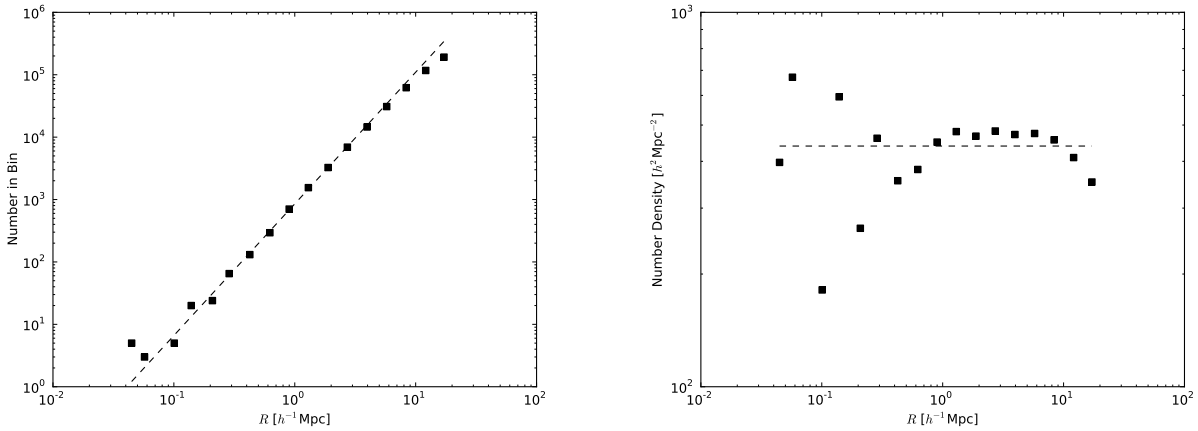

(c) $\Lambda : 126.3 - 361.6$

Figure 6.40: "Observed" deprojected number and number density profiles for clusters binned by richness.

Bibliography

Alcock, C., Akerlof, C. W., Allsman, R. A., Axelrod, T. S., Bennett, D. P., Chan, S., Cook, K. H., Freeman, K. C., Griest, K., Marshall, S. L., Park, H.-S., Perlmutter, S., Peterson, B. A., Pratt, M. R., Quinn, P. J., Rodgers, A. W., Stubbs, C. W., and Sutherland, W.: 1993, *Nature* **365**, 621

Alcock, C., Allsman, R. A., Alves, D. R., Axelrod, T. S., Becker, A. C., Bennett, D. P., Cook, K. H., Dalal, N., Drake, A. J., Freeman, K. C., Geha, M., Griest, K., Lehner, M. J., Marshall, S. L., Minniti, D., Nelson, C. A., Peterson, B. A., Popowski, P., Pratt, M. R., Quinn, P. J., Stubbs, C. W., Sutherland, W., Tomaney, A. B., Vandehei, T., and Welch, D.: 2000, *Astrophysical Journal* **542**, 281

Allen, S. W.: 1998, *Monthly Notices of the Royal Astronomical Society* **296**, 392

Aubourg, E., Bareyre, P., Bréhin, S., Gros, M., Lachièze-Rey, M., Laurent, B., Lesquoy, E., Magneville, C., Milsztajn, A., Moscoso, L., Queinnec, F., Rich, J., Spiro, M., Vigroux, L., Zylberajch, S., Ansari, R., Cavalier, F., Moniez, M., Beaulieu, J.-P., Ferlet, R., Grison, P., Vidal-Madjar, A., Guibert, J., Moreau, O., Tajahmady, F., Maurice, E., Prévôt, L., and Gry, C.: 1993, *Nature* **365**, 623

Baldauf, T., Smith, R. E., Seljak, U., and Mandelbaum, R.: 2010, *Physical Review D* **81(6)**, 063531

Bartelmann, M.: 1995, *Astronomy and Astrophysics* **303**, 643

Bartelmann, M., King, L. J., and Schneider, P.: 2001, *Astronomy and Astrophysics* **378**, 361

Berlind, A. A. and Weinberg, D. H.: 2002, *Astrophysical Journal* **575**, 587

Blandford, R. D., Saust, A. B., Brainerd, T. G., and Villumsen, J. V.: 1991, *Monthly Notices of the Royal Astronomical Society* **251**, 600

Brainerd, T. G., Blandford, R. D., and Smail, I.: 1996, *Astrophysical Journal* **466**, 623

Colley, W. N., Schild, R. E., Abajas, C., Alcalde, D., Aslan, Z., Bikmaev, I., Chavushyan, V., Chinarro, L., Cournoyer, J.-P., Crowe, R., Dudinov, V., Evans, A. K. D., Jeon, Y.-B., Goicoechea, L. J., Golbasi, O., Khamitov, I., Kjernsmo, K., Lee, H. J., Lee, J., Lee, K. W., Lee, M. G., Lopez-Cruz, O., Mediavilla, E., Moffat, A. F. J., Mujica, R., Ullan, A.,

Muñoz, J., Oscoz, A., Park, M.-G., Purves, N., Saanum, O., Sakhibullin, N., Serra-Ricart, M., Sinelnikov, I., Stabell, R., Stockton, A., Teuber, J., Thompson, R., Woo, H.-S., and Zheleznyak, A.: 2003, *Astrophysical Journal* **587**, 71

Corless, V. L. and King, L. J.: 2007, *Monthly Notices of the Royal Astronomical Society* **380**, 149

Curtis, H. D.: 1921, *Bulletin of the National Research Council* 2(171)

Deutsch, M. and Beniaminy, I.: 1982, *Applied Physics Letters* **41**, 27

Duffy, A. R., Schaye, J., Kay, S. T., and Dalla Vecchia, C.: 2008, *Monthly Notices of the Royal Astronomical Society* **390**, L64

Einstein, A.: 1920, *Relativity: The special and general theory*, Henry Holt and Company

Einstein, A.: 1936, *Science* **84**, 506

Fadely, R., Keeton, C. R., Nakajima, R., and Bernstein, G. M.: 2010, *Astrophysical Journal* **711**, 246

Fan, X., Strauss, M. A., Schneider, D. P., Becker, R. H., White, R. L., Haiman, Z., Gregg, M., Pentericci, L., Grebel, E. K., Narayanan, V. K., Loh, Y.-S., Richards, G. T., Gunn, J. E., Lupton, R. H., Knapp, G. R., Ivezić, Ž., Brandt, W. N., Collinge, M., Hao, L., Harbeck, D., Prada, F., Schaye, J., Strateva, I., Zakamska, N., Anderson, S., Brinkmann, J., Bahcall, N. A., Lamb, D. Q., Okamura, S., Szalay, A., and York, D. G.: 2003, *Astrophysics Journal* **125**, 1649

Fischer, P., McKay, T. A., Sheldon, E., Connolly, A., Stebbins, A., Frieman, J. A., Jain, B., Joffre, M., Johnston, D., Bernstein, G., Annis, J., Bahcall, N. A., Brinkmann, J., Carr, M. A., Csabai, I., Gunn, J. E., Hennessy, G. S., Hindsley, R. B., Hull, C., Ivezić, Ž., Knapp, G. R., Limmongkol, S., Lupton, R. H., Munn, J. A., Nash, T., Newberg, H. J., Owen, R., Pier, J. R., Rockosi, C. M., Schneider, D. P., Smith, J. A., Stoughton, C., Szalay, A. S., Szokoly, G. P., Thakar, A. R., Vogeley, M. S., Waddell, P., Weinberg, D. H., York, D. G., and The SDSS Collaboration: 2000, *Astrophysics Journal* **120**, 1198

Fort, B., Prieur, J. L., Mathez, G., Mellier, Y., and Soucail, G.: 1988, *Astronomy and Astrophysics* **200**, L17

Gao, L., Navarro, J. F., Cole, S., Frenk, C. S., White, S. D. M., Springel, V., Jenkins, A., and Neto, A. F.: 2008, *Monthly Notices of the Royal Astronomical Society* **387**, 536

Gorenstein, M. V., Shapiro, I. I., and Falco, E. E.: 1988, *Astrophysical Journal* **327**, 693

Guzik, J. and Seljak, U.: 2002, *Monthly Notices of the Royal Astronomical Society* **335**, 311

Hirata, C. M., Mandelbaum, R., Seljak, U., Guzik, J., Padmanabhan, N., Blake, C., Brinkmann, J., Budávari, T., Connolly, A., Csabai, I., Scranton, R., and Szalay, A. S.: 2004, *Monthly Notices of the Royal Astronomical Society* **353**, 529

Hoekstra, H., Yee, H. K. C., and Gladders, M. D.: 2004, *Astrophysical Journal* **606**, 67

Hogg, D. W.: 1999, *ArXiv Astrophysics e-prints* arXiv:astro-ph/9905116

Joachimi, B., Mandelbaum, R., Abdalla, F. B., and Bridle, S. L.: 2011, *Astronomy and Astrophysics* **527**, A26

Johnston, D. E., Sheldon, E. S., Tasitsiomi, A., Frieman, J. A., Wechsler, R. H., and McKay, T. A.: 2007a, *Astrophysical Journal* **656**, 27

Johnston, D. E., Sheldon, E. S., Wechsler, R. H., Rozo, E., Koester, B. P., Frieman, J. A., McKay, T. A., Evrard, A. E., Becker, M. R., and Annis, J.: 2007b, *ArXiv e-prints* arXiv:0709.1159v1

Kaiser, N.: 1992, *Astrophysical Journal* **388**, 272

Kaiser, N.: 1995, *Astrophysical Journal Letters* **439**, L1

Kaiser, N. and Squires, G.: 1993, *Astrophysical Journal* **404**, 441

Klimov, Y. G.: 1964, *Soviet Journal of Astronomy* **7**, 664

Kundic, T., Turner, E. L., Colley, W. N., Gott, III, J. R., Rhoads, J. E., Wang, Y., Bergeron, L. E., Gloria, K. A., Long, D. C., Malhotra, S., and Wambsganss, J.: 1997, *Astrophysical Journal* **482**, 75

Lehar, J., Hewitt, J. N., Burke, B. F., and Roberts, D. H.: 1992, *Astrophysical Journal* **384**, 453

Liebes, S.: 1964, *Physical Review* **133**, 835

Lodge, O. J.: 1919, *Nature* **104**, 354

Lynds, R. and Petrosian, V.: 1986, in *Bulletin of the American Astronomical Society*, Vol. 18 of *Bulletin of the American Astronomical Society*, p. 1014

Mahdavi, A., Hoekstra, H., Babul, A., and Henry, J. P.: 2008, *Monthly Notices of the Royal Astronomical Society* **384**, 1567

Mandelbaum, R., Seljak, U., Cool, R. J., Blanton, M., Hirata, C. M., and Brinkmann, J.: 2006, *Monthly Notices of the Royal Astronomical Society* **372**, 758

Mandelbaum, R., Seljak, U., and Hirata, C. M.: 2008a, *Journal of Cosmology and Astroparticle Physics* **8**, 6

Mandelbaum, R., Seljak, U., Hirata, C. M., Bardelli, S., Bolzonella, M., Bongiorno, A., Carollo, M., Contini, T., Cunha, C. E., Garilli, B., Iovino, A., Kampczyk, P., Kneib, J.-P., Knobel, C., Koo, D. C., Lamareille, F., Le Fèvre, O., Le Borgne, J.-F., Lilly, S. J., Maier, C., Mainieri, V., Mignoli, M., Newman, J. A., Oesch, P. A., Perez-Montero, E., Ricciardelli, E., Scodeggio, M., Silverman, J., and Tasca, L.: 2008b, *Monthly Notices of the Royal Astronomical Society* **386**, 781

Mandelbaum, R., Tasitsiomi, A., Seljak, U., Kravtsov, A. V., and Wechsler, R. H.: 2005, *Monthly Notices of the Royal Astronomical Society* **362**, 1451

McKay, T. A., Sheldon, E. S., Racusin, J., Fischer, P., Seljak, U., Stebbins, A., Johnston, D., Frieman, J. A., Bahcall, N., Brinkmann, J., Csabai, I., Fukugita, M., Hennessy, G. S., Ivezic, Z., Lamb, D. Q., Loveday, J., Lupton, R. H., Munn, J. A., Nichol, R. C., Pier, J. R., and York, D. G.: 2001, *ArXiv Astrophysics e-prints* arXiv:astro-ph/0108013

Mellier, Y., Fort, B., Soucail, G., Mathez, G., and Cailloux, M.: 1991, *Astrophysical Journal* **380**, 334

Merritt, D., Graham, A. W., Moore, B., Diemand, J., and Terzić, B.: 2006, *Astrophysics Journal* **132**, 2685

Miralda-Escude, J.: 1991, *Astrophysical Journal* **380**, 1

Miralda-Escude, J. and Babul, A.: 1995, *Astrophysical Journal* **449**, 18

Navarro, J. F., Frenk, C. S., and White, S. D. M.: 1997, *Astrophysical Journal* **490**, 493

Navarro, J. F., Hayashi, E., Power, C., Jenkins, A. R., Frenk, C. S., White, S. D. M., Springel, V., Stadel, J., and Quinn, T. R.: 2004, *Monthly Notices of the Royal Astronomical Society* **349**, 1039

Navarro, J. F., Ludlow, A., Springel, V., Wang, J., Vogelsberger, M., White, S. D. M., Jenkins, A., Frenk, C. S., and Helmi, A.: 2010, *Monthly Notices of the Royal Astronomical Society* **402**, 21

Ota, N., Mitsuda, K., and Fukazawa, Y.: 1998, *Astrophysical Journal* **495**, 170

Paczynski, B.: 1986, *Astrophysical Journal* **304**, 1

Paczynski, B.: 1987, *Nature* **325**, 572

Peebles, P. J. E.: 1993, *Principles of Physical Cosmology*, Princeton University Press

Pierre, M., Le Borgne, J. F., Soucail, G., and Kneib, J. P.: 1996, *Astronomy and Astrophysics* **311**, 413

Powell, M.: 1994, *A direct search optimization method that models the objective and constraint functions by linear interpolation*, pp 51–64, Kluwer Academic

Refsdal, S.: 1964a, *Monthly Notices of the Royal Astronomical Society* **128**, 307

Refsdal, S.: 1964b, *Monthly Notices of the Royal Astronomical Society* **128**, 295

Sahu, K. C., Shaw, R. A., Kaiser, M. E., Baum, S. A., Ferguson, H. C., Hayes, J. J. E., Gull, T. R., Hill, R. J., Hutchings, J. B., Kimble, R. A., Plait, P., and Woodgate, B. E.: 1998, *Astrophysical Journal Letters* **492**, L125

Schild, R. E.: 1990, *Astrophysics Journal* **100**, 1771

Schneider, P.: 2006a, *Part 1: Introduction to gravitational lensing and cosmology*, pp 1–89, Springer

Schneider, P.: 2006b, *Part 3: Weak Gravitational Lensing*, p. 269, Springer

Schneider, P., King, L., and Erben, T.: 2000, *Astronomy and Astrophysics* **353**, 41

Schneider, P. and Rix, H.-W.: 1997, *Astrophysical Journal* **474**, 25

Schneider, P. and Seitz, C.: 1995, *Astronomy and Astrophysics* **294**, 411

Seljak, U.: 2000, *Monthly Notices of the Royal Astronomical Society* **318**, 203

Seljak, U.: 2002, *Monthly Notices of the Royal Astronomical Society* **334**, 797

Seljak, U. and Warren, M. S.: 2004, *Monthly Notices of the Royal Astronomical Society* **355**, 129

Shapley, H.: 1921, *Bulletin of the National Research Council* 2(194)

Sheldon, E. S., Cunha, C., Mandelbaum, R., Brinkmann, J., and Weaver, B. A.: 2011, *ArXiv e-prints* arXiv:1109.5192v1

Sheldon, E. S., Johnston, D. E., Frieman, J. A., Scranton, R., McKay, T. A., Connolly, A. J., Budavári, T., Zehavi, I., Bahcall, N. A., Brinkmann, J., and Fukugita, M.: 2004, *Astrophysics Journal* **127**, 2544

Sheldon, E. S., Johnston, D. E., Scranton, R., Koester, B. P., McKay, T. A., Oyaizu, H., Cunha, C., Lima, M., Lin, H., Frieman, J. A., Wechsler, R. H., Annis, J., Mandelbaum, R., Bahcall, N. A., and Fukugita, M.: 2009, *Astrophysical Journal* **703**, 2217

Smail, I., Ellis, R. S., Dressler, A., Couch, W. J., Oemler, Jr., A., Sharples, R. M., and Butcher, H.: 1997, *Astrophysical Journal* **479**, 70

Soucail, G., Fort, B., Mellier, Y., and Picat, J. P.: 1987, *Astronomy and Astrophysics* **172**, L14

Soucail, G., Mellier, Y., Fort, B., Mathez, G., and Cailloux, M.: 1988, *Astronomy and Astrophysics* **191**, L19

Stockton, A.: 1980, *Astrophysical Journal Letters* **242**, L141

Tinker, J. L., Sheldon, E. S., Wechsler, R. H., Becker, M. R., Rozo, E., Zu, Y., Weinberg, D. H., Zehavi, I., Blanton, M. R., Busha, M. T., and Koester, B. P.: 2012, *Astrophysical Journal* **745**, 16

Tyson, J. A., Valdes, F., Jarvis, J. F., and Mills, Jr., A. P.: 1984, *Astrophysical Journal Letters* **281**, L59

Tyson, J. A., Wenk, R. A., and Valdes, F.: 1990, *Astrophysical Journal Letters* **349**, L1

Vanderriest, C., Schneider, J., Herpe, G., Chevreton, M., Moles, M., and Wlerick, G.: 1989, *Astronomy and Astrophysics* **215**, 1

Walsh, D., Carswell, R. F., and Weymann, R. J.: 1979, *Nature* **279**, 381

Wambsganss, J.: 1998, *Living Reviews in Relativity* **1**, 12

Webster, R. L.: 1985, *Monthly Notices of the Royal Astronomical Society* **213**, 871

Weinberg, D. H., Mortonson, M. J., Eisenstein, D. J., Hirata, C., Riess, A. G., and Rozo, E.: 2012, *ArXiv e-prints* arXiv:1201.2434v1

Wright, C. O. and Brainerd, T. G.: 2000, *Astrophysical Journal* **534**, 34

Wu, X.-P. and Fang, L.-Z.: 1997, *Astrophysical Journal* **483**, 62

Wyrzykowski, L., Skowron, J., Kozłowski, S., Udalski, A., Szymański, M. K., Kubiak, M., Pietrzyński, G., Soszyński, I., Szewczyk, O., Ulaczyk, K., Poleski, R., and Tisserand, P.: 2011, *Monthly Notices of the Royal Astronomical Society* **416**, 2949

Yang, X., Mo, H. J., van den Bosch, F. C., Jing, Y. P., Weinmann, S. M., and Meneghetti, M.: 2006, *Monthly Notices of the Royal Astronomical Society* **373**, 1159

Yoo, J., Tinker, J. L., Weinberg, D. H., Zheng, Z., Katz, N., and Davé, R.: 2006, *Astrophysical Journal* **652**, 26

Young, P., Gunn, J. E., Oke, J. B., Westphal, J. A., and Kristian, J.: 1980, *Astrophysical Journal* **241**, 507

Zehavi, I., Weinberg, D. H., Zheng, Z., Berlind, A. A., Frieman, J. A., Scoccimarro, R., Sheth, R. K., Blanton, M. R., Tegmark, M., Mo, H. J., Bahcall, N. A., Brinkmann, J., Burles, S., Csabai, I., Fukugita, M., Gunn, J. E., Lamb, D. Q., Loveday, J., Lupton, R. H., Meiksin, A., Munn, J. A., Nichol, R. C., Schlegel, D., Schneider, D. P., SubbaRao, M., Szalay, A. S., Uomoto, A., York, D. G., and SDSS Collaboration: 2004, *Astrophysical Journal* **608**, 16

Zhang, Y.-Y., Finoguenov, A., Böhringer, H., Kneib, J.-P., Smith, G. P., Kneissl, R., Okabe, N., and Dahle, H.: 2008, *Astronomy and Astrophysics* **482**, 451

Zhang, Y.-Y., Okabe, N., Finoguenov, A., Smith, G. P., Piffaretti, R., Valdarnini, R., Babul, A., Evrard, A. E., Mazzotta, P., Sanderson, A. J. R., and Marrone, D. P.: 2010, *Astrophysical Journal* **711**, 1033

Zwicky, F.: 1937a, *Physical Review* **51**, 290

Zwicky, F.: 1937b, *Physical Review* **51**, 679